1 of 2
AD
A115889

AD A115889

RADC-TR-82-95
Final Technical Report
April 1982

MAGNETIC FIELD SYNTHESIS FOR MICROWAVE MAGNETICS

Massachusetts Institute of Technology

Frederic R. Morgenthaler

APPROVED FOR PUBLIC RELEASE; DISTRIBUTION UNLIMITED

ROME AIR DEVELOPMENT CENTER
Air Force Systems Command
Griffiss Air Force Base, NY 13441

DTIC
ELECTE
JUN.2 2 1982

S   D

B

82 06 21 098

This report has been reviewed by the RADC Public Affairs Office (PA) and is releasable to the National Technical Information Service (NTIS). At NTIS it will be releasable to the general public, including foreign nations.

RADC-TR-82-95 has been reviewed and is approved for publication.

APPROVED: *James C. Sethares*

JAMES C. SETHARES
Project Engineer

APPROVED: *Allan C. Schell*

ALLAN C. SCHELL
Chief, Electromagnetic Sciences Division

FOR THE COMMANDER: *John P. Huss*

JOHN P. HUSS
Acting Chief, Plans Office

UNCLASSIFIED

REPORT DOCUMENTATION PAGE		READ INSTRUCTIONS BEFORE COMPLETING FORM
1. REPORT NUMBER RADC-TR-82-95	**2 GOVT ACCESSION NO.** AD-A115 889	**3. RECIPIENT'S CATALOG NUMBER**
4. TITLE (and Subtitle) MAGNETIC FIELD SYNTHESIS FOR MICROWAVE MAGNETICS		**5. TYPE OF REPORT & PERIOD COVERED** Final Technical Report 1 Jan 79 - 30 Nov 80
		6. PERFORMING ORG. REPORT NUMBER N/A
7. AUTHOR(s) Frederic R. Morgenthaler		**8. CONTRACT OR GRANT NUMBER(s)** F19628-79-C-0047
9. PERFORMING ORGANIZATION NAME AND ADDRESS Massachusetts Institute of Technology Dept of E.E. & Computer Sciences Cambridge MA 02139		**10. PROGRAM ELEMENT, PROJECT, TASK AREA & WORK UNIT NUMBERS** 61101F LD9501C1
11. CONTROLLING OFFICE NAME AND ADDRESS Deputy for Electronic Technology (RADC/EEAC) Hanscom AFB MA 01731		**12. REPORT DATE** APRIL 1982
		13. NUMBER OF PAGES 178
14. MONITORING AGENCY NAME & ADDRESS(if different from Controlling Office) Same		**15. SECURITY CLASS. (of this report)** UNCLASSIFIED
		15a. DECLASSIFICATION/DOWNGRADING SCHEDULE N/A

16. DISTRIBUTION STATEMENT (of this Report)

Approved for public release; distribution unlimited

17. DISTRIBUTION STATEMENT (of the abstract entered in Block 20, if different from Report)

Same

18. SUPPLEMENTARY NOTES

RADC Project Engineer: James C. Sethares (EEAC)

This effort was funded totally by the Laboratory Directors' Fund

19. KEY WORDS (Continue on reverse side if necessary and identify by block number)

Magnetostatic Waves	Microwave Magnetics
Field Synthesis	Non Uniform Fields
Ferrimagnetic Films	Yettrium Iron Garnet
Magnetic Fields	

20. ABSTRACT (Continue on reverse side if necessary and identify by block number)

The Microwave and Quantum Magnetics Group of the M.I.T. Department of Electrical Engineering and Computer Science undertook a two-year research program directed at developing synthesis procedures that allow magnetostatic and/or magnetoelastic modes to be specially tailored for microwave signal processing applications that include magnetically tunable filters and limiters as well as delay lines that are either linearly dispersive or nondispersive over prescribed bandwidths. (over)
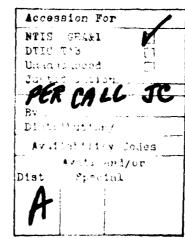
DD FORM 1473 EDITION OF 1 NOV 65 IS OBSOLETE

UNCLASSIFIED

Special emphasis was given to devices employing thin films of yttrium iron garnet (YIG) that are blessed with spatially nonuniform dc magnetic fields.

TABLE OF CONTENTS

Accession For
NTIS GRA&I
DTIC TAB
Unannounced
Justification
PER CALL JC
By
Distribution/
Availability Codes
Avail and/or
Dist Special
A

Introduction

Magnetic resonance is normally very much broadened if a ferrimagnetic sample is immersed in a spatially non-uniform field. Experimentalists measuring fundamental resonance parameters take great pains therefore to employ ellipsoidal sample shapes (usually small spheres) that are positioned in fields of very high uniformity. Because surface roughness is known to cause scattering from the uniform mode to degenerate spinwaves of short wavelengths, thereby increasing the resonance linewidth, additional effort is expended in polishing the surfaces to optical tolerances.

Commercial manufacturers of tunable microwave, yttrium iron garnets (YIG) filters avail themselves of this knowledge and employ uniformly magnetized, highly polished spherical single crystals in their designs.

From this perspective it is therefore remarkable that we at MIT observed extremely sharp resonances of a very localized character in single crystal YIG slabs and films that encounter highly uniform bias fields. On the other hand, it has been known for some time that magnetoelastic waves can be highly focussed by, and propagate with low loss in, steep magnetic field gradients. One view of the high Q resonance is that magnetostatic mode patterns are formed for which the resonant energies are highly confined to certain regions or "tracks" within the crystal that allow wave propagation around them. If the mode amplitudes are very small at the edges and corners of the sample, the surface scattering (which one would expect to be enormous) is largely prevented; consequently the Q of the resonance is governed primarily by the intrinsic linewidth of the bulk crystal together with normal circuit loading considerations. In effect, appropriately designed magnetic field profiles create surfaces of discontinuity where there are no actual surfaces; surface wave propagation at such "surfaces" should be free of many of the drawbacks and loss mechanisms encountered at true surfaces. It has been our intent to learn how to characterize, control and efficiently couple to such modes so that one can create a new class of microwave magnetically-tunable resonance filters.

Our research goals concerned Magnetoelastic Delay Line and Magnetostatic Mode/Wave Synthesis; we separately enumerate our results for each of these two major topics.

Personnel Supported in Part by the Contract

Professor F. R. Morgenthaler	Principal Investigator
Professor R. L. Kyhl	Senior Research Staff
Dale Zeskind	Senior Research Staff
Dr. Tushar Bhattacharjee	Postdoctoral Research
Daniel Fishman	Research Assistant
Leslie Itano	Research Assistant
Johnny Low	Research Assistant
Daniel Stancil	Research Assistant
Nickolas Vlannes	Research Assistant

Publications

F. R. Morgenthaler, "Synthesized Magnetostatic Resonances in a Nonuniformly Biased Thin Disk Without Conducting Boundaries," IEEE Transactions on Magnetics, Vol. MAG-16, NO. 5, September 1980. p. 1150.

D. D. Stancil and F. R. Morgenthaler, "Magnetostatic Surface Modes in a Thin Film with Nonuniform In-plane Fields," IEEE Transactions on Magnetics, Vol. MAG-16, No. 5, September 1980, p. 1156.

D. D. Stancil, "Magnetostatic Waves in Nonuniform Bias Fields Including Exchange Effects," IEEE Transactions on Magnetics, Vol. MAG-16, No. 5, September 1980, p. 1153.

F. R. Morgenthaler, "Novel Devices Based Upon Field Gradient Control of Magnetostatic Modes and Waves," The 3rd International Conference on Ferrites, September 29 - October 2, 1980, Kyoto, Japan. To be Published.

F. R. Morgenthaler, "Synthesis of Magnetostatic Waves and Modes Using Nonuniform Bias Fields," 1980 IEEE Ultrasonics Symposium Proceedings, November 1980, p. 532.

D. D. Stancil and F. R. Morgenthaler, "The Effects of Nonuniform In-plane Fields on the Propagation Characteristics of Magnetostatic Surface Waves," 1980 Ultrasonics Symposium Proceedings, November 1980, p. 547.

F. R. Morgenthaler, "Magnetostatic Surface Modes in Nonuniform Thin Films with In-plane Bias Fields," J. of Applied Physics, Vol. 52, No. 3, Part II, March 1980. p. 2267.

Publications (cont.)

D. D. Stancil, "Localized Magnetostatic Resonances in Inhomogeneous Fields Including Exchange Effects," Technical Memorandum, April 1979.

D. D. Stancil, "Virtual Surfaces, Harmonic Oscillator Wavefunctions, and the Spin Wave Continuum," Technical Memorandum, June 29, 1979.

Theses (in progress)

Daniel Stancil, "Effects of Nonuniform Fields on Magnetostatic Waves in Ferrite Thin Films", Ph.D. Thesis to be submitted to the Dept. of Electrical Engineering and Computer Science.

Daniel Fishman, "Investigation of the Velocity of Energy Circulation of Magnetostatic modes in YIG," S.M. Thesis, to be submitted to the Dept of Electrical Engineering and Computer Science.

Leslie Itano, "Microwave Delay Line with Thin Antennae," S.M. Thesis, to be submitted to the Dept. of Electrical Engineering and Computer Science.

Synthesized Magnetoelastic Delay Lines

Time Prism Filters

The basis for the research program in magnetoelastic delay line synthesis that was undertaken for the Air Force by the MIT Microwave and Quantum Magnetics Group under Contract F19628-79-C-0047 is contained, in the following paper that is included for completeness.

The dc field synthesis techniques were developed at M.I.T. by the principal investigator and culminated in U.S. Patent # 4,093,929 dated June 6, 1978.

The linearly dispersive delay lines (Time Prism Filters) cited were fabricated and measured by Dr. A. Platzker at Chu Associates, Littleton, Massachusetts who was then a concurrent member of the Microwave and Quantum Magnetics Group.

Field Gradient control of spatially localized magnetostatic resonances is covered by U.S. Patent 4,152,676, May 1, 1979 (Morgenthaler and Zeskind).

MAGNETIC FIELD SYNTHESIS PROCEDURES
FOR MAGNETOSTATIC AND MANETOELASTIC DEVICES*

F.R. Morgenthaler and A. Platzker

Department of Electrical Engineering and Computer Science,
Massachusetts Institute of Technology, Cambridge, Mass. 02139 and
Chu Associates, Littleton, Mass. 01460

ABSTRACT

Certain types of magnetostatic and/or magneto-elastic devices require nonuniform dc bias fields of sufficient strength to locally saturate the active ferrite element.

We here review a synthesis procedure for cylindrically symmetric geometries that allows pre-specification of the field either on the symmetry axis or on a plane perpendicular to it.

The method is then applied to the cases of both a thin film disk magnetized normally to its plane and microwave magnetoelastic delay line designed for linear frequency dispersion over wide bandwidths.

Finally, we report construction details and test data on an actual packaged device having greatly improved characteristics. Measured parameters for two-port operation at S-band over a 1 GHz. bandwidth include a linear dispersion factor $D=.3$ nsec/MHz. and an insertion loss (untuned) of 27-30 Db.

INTRODUCTION

Although many magnetic resonance devices ideally operate with a dc magnetic field bias that is spatially uniform, there are a number of magnetostatic and magnetoelastic wave devices that either require or benefit from nonuniform dc fields. Although the equations governing the dc magnetic field within a locally saturated ferrimagnet are well known and can be solved numerically for any set of boundary conditions that force uniqueness, the solution when found may not be the field required for proper device operation. Fortunately, a synthesis procedure has been formulated[1] that allows one to specify the desired field along axes or planes of symmetry and then work outward to find, first, the entire field within the magnetic material, second, appropriate high permeability pole pieces or current windings capable of sustaining that field.

We first describe the synthesis procedure and show how to produce prescribed nonuniform radially symmetric dc fields in a normally magnetized thin film. We then apply the method to high performance magnetoelastic linearly dispersive delay lines that employ cylindrical crystals of yttrium iron garnet (YIG).

BASIC EQUATIONS

Within a current free magnetic material, and neglecting crystalline anisotropy, the dc $\bar{H}$-field is both curl free and parallel to the magnetization vector, $\bar{M}$. If the latter is assumed locally saturated to a uniform value M, it follows in terms of the scalar magnetic potential ψ

that
$$\bar{H} = \nabla\psi \tag{1}$$
and
$$\bar{M} = M\nabla\psi/|\nabla\psi| \tag{2}$$

The final constraint is $\nabla\cdot\mu_o(\bar{H}+\bar{M}) = 0$, therefore

$$\nabla\cdot[(1+M/|\nabla\psi|)\nabla\psi] = 0 \tag{3}$$

Although this equation can be solved numerically subject to any set of boundary conditions that force a unique solution, the analysis of such a boundary value problem is often tedious. Moreover, and of greater importance, the H-field, when found, may not be that which is desired. Then, the boundaries must be modified, the field recomputed and so on in an iterative "cut and try" manner. It would appear to be much more difficult to carry out field synthesis rather than analysis. However, the synthesis of a desired field is actually a much simpler problem.

In essence, the procedure starts by assuming the specified field to exist along an axis or plane of symmetry for which the direction of $\bar{M}$ can be deduced. The potential ψ is then expanded in an appropriate series within the magnetic region. This portion of the synthesis is termed the "inner"-field determination and is carried out without regard to the boundaries of the magnetic material. The next stage of the procedure involves expanding, in a convenient series, the Laplacian potential in the nonmagnetic region outside of some assumed boundary surface. The coefficients of the "outer"-field potential are next matched to those of the "inner"-field so as to satisfy, in a least-squares sense, the proper boundary-conditions.

Finally, we design high-permeability pole-pieces or current sheets that when suitably energized will create the outer and hence also the inner field.

AN OVERVIEW OF THE SYNTHESIS PROCEDURE

Although more general situations also can be treated by similar methods, we here restrict our discussion to cylindrically symmetric fields when the material shape is a cylinder or disk. There are then two cases of particular interest. They result from specification of the $\bar{H}$-field along either the axis of symmetry $H_z(o,z)$ or an appropriate plane perpendicular to that axis ($H_z(r,z_o)$).

The synthesis procedure can be divided into the following steps:

1. Find the H-field that meets the on-axis or on-plane field requirement inside of the cylinder of length L and radius R for specified magnetization M.

2. Choose a convenient series expansion for the Laplacian scalar potential outside of the cylinder and match boundary conditions over the entire surface. Solve for the coefficients of the outer potential. It may prove useful to subdivide the outer region and carry out a separate a match for each subregion.

3. Plot the equipotentials of the outer field and choose two (or more) that are appropriate to serve as surface contours of high permeability magnetic pole pieces. If subdivision of the outer region has been utilized, pole pieces must in general touch the material at the division points so as to isolate the various outer subregions.

4. Alternatively, if a solenoid is to be used to generate the field without benefit of magnetic pole pieces, the field outside of the winding surface must be chosen with continuous normal flux and vanish as $r \to \infty$. The discontinuity in the tangential field then determines the surface electric current density and hence winding design.

5. If a satisfactory design does not result from the synthesis procedure, one can alter the assumed material boundary surface and/or the "outer"-field expansion and try again.

It is important to realize that although an infinite number of combinations of material size, shape and pole piece designs exist, all of which would create the desired field, once one has been chosen the field it creates is unique.[1]

INNER FIELD

Because symmetry dictates that both $H_r(o,z)$ and $M_r(o,z)$ must vanish, and the axis ($r=0$) is assumed nonsingular, an appropriate expansion of the potential within the magnetic material is

$$\psi = \sum_{n=0} a_{2n}(z) \, r^{2n} \tag{4}$$

One could substitute Eq. (4) into Eq. (3) and expand the result so as to find a_2 in terms of a_o and its derivatives and so on. However, it is more convenient to separately expand $\bar{M}$ as

$$\bar{M}=M[\bar{1}_z \sum_{n=0} b_{2}(z) r^{2n} + \bar{1}_r \sum_{n=0} b_{2n+1}(z) r^{2n+1}] \tag{5}$$

and require $|\bar{M}| = M$, $\bar{M} \times \bar{H} = 0$, and $\nabla \cdot \bar{B} = 0$. The result is three sets of constraints, respectively

$$\sum_{n=0}^{s}[a'_{2n} \, b_{[2(s-n)+1]} - 2(s+1-n)a_{2(s+1-n)} b_{2n}] = 0 \tag{6a}$$

$$\sum_{n=0}^{s}[b_{2n+1}b_{2(s-n)+1} + b_{2n}b_{2(s+1-n)}] + b_o b_{2(s+1)} = 0 \tag{6b}$$

$$4(s+1)^2 a_{2(s+1)} + 2(s+1)Mb_{2s+1} + a''_{2s} + Mb'_{2s} = 0 \tag{6c}$$

where the primes denote differentiation with respect to z and $s=0, 1, 2, 3, \ldots$ In addition, $b_o = 1$ and $o_o a'_o > C$. In order to ensure local saturation, a'_o is either positive or negative definite over the interval; we take $a'_o > 0$ and $b_o = +1$ without loss of generality. Eqs. (6) yield, for each value of $s: b_{s+1}, a_{s+2}$ and b_{s+2} in terms of the lower order a and b coefficients and their derivatives. Therefore one starts with $s=0$ and proceeds upwards to generate as many terms as are needed. For $s=0$

$$b_1 = - a''_o/2(a'_o+M) \tag{7a}$$

$$a_2 = a'_o b_1/2 \tag{7b}$$

$$b_2 = - b_1^2/2 \tag{7c}$$

Provided $a'_o(z)$ is either specified or can be deduced, the various functions a_{2n} constitute the desired solution of Eq. (3). The number of terms required to satisfactorily approximate the field depends upon the extent of r, the value of M and the particular function a'_o.

If the material has uniaxial magnetic anisotropy oriented along the z-axis, the procedure can be generalized by replacing in Eq. (6a)

$$a'_{2n} \to a'_{2n} - \frac{2K_o}{\mu_o M} b_{2n}$$

where K_o is the uniaxial anisotropy constant. ($K_o < 0$ easy axis; $K_o > 0$ easy plane). If the anisotropy is not uniaxial with respect to the z-axis, (as for example a cubic material with [100] or [111] orientation) the formulation may still be used by replacing K_o with an appropriate effective value provided the radial component of $\bar{M}$ is not too large. If M_r/M_z is large, the field is, of course, not strictly cylindrically symmetric.

The expansion of Eq. (4) is very helpful when the on-axis field is what is specified because then $a'_o(z)$ is known. On the other hand, if $H_z(r,z_o)$ is specified, an alternate approach is preferable. In this case we expand ψ as

$$\psi = a_o(r) + a_1(r)(z-z_o) + a_2(r)(z-z_o)^2 + \ldots \tag{8}$$

with $a_z(r) = H_z(r,z_o)$ and assurance that $a'_n(0) = 0$ for all n.

THE OUTER FREE SPACE POTENTIAL

If the z-axis passes through an outer field subregion, the Laplacian outer-potential ψ for that subregion may be taken nonsingular over all z and expanded in the form

$$\hat{\psi} = \hat{a}_o(z) - \frac{\hat{a}''_o(z)}{(1!)^2} \left(\frac{r}{2}\right)^2 + \frac{\hat{a}''''_o(z)}{(2!)^2} \left(\frac{r}{2}\right)^4 - \ldots \tag{9}$$

Naturally, if $\hat{a}_o$ is taken to be $\binom{\sin}{\cos}(kz)$ or $\binom{\sinh}{\cosh}(kz)$ $\hat{\psi}$ factors into the product of $\hat{a}_o$

and either $I_0(kr)$ or $J_0(kr)$. However, the usual cylinder functions are not especially convenient because our boundary specification does not lead readily to identification of eigenvalues of k.

For $\hat{a}_0 = z^n$, Eq. (9) generates the set of polynomials $P_n^*(r,z)$ that satisfy the recurrence formula

$$P_n^* = \frac{2n-1}{n} z P_{n-1}^* - \frac{n-1}{n}(z^2+r^2)P_{n-2}^*$$

With $P_0^* = 1$, it follows that $P_n^* = (r^2+z^2)^{n/2}P_n^0(\cos\theta)$ where $\tan\theta = r/z$ and P_n^0 is the associated Legendre function of degree n and order zero.

For subregions of the outer field that do not contain the z-axis, solutions with a logarithmic singularity at $r=0$ are often helpful. In such cases, we employ the set of polynomials $Q_n^*(r,z)$ that satisfy the recurrence formula

$$Q_n^* = \frac{2n-1}{n} z Q_{n-1}^* - \frac{n-1}{n}(z^2+r^2)Q_{n-2}^* - \frac{2}{n}(P_n^* - zP_{n-1}^*)$$

with $\quad Q_0^* = (1 + \ln r)$

It is also permissable and often advantageous to utilize in the expansion axial multipoles of the form

$$\frac{d^n}{dz^n}\left((z-z_0)/[(z-z_0)^2+r^2]^{3/2}\right) \quad n=0,1,2,\ldots.$$

as long as their locations $r=0$, $z=z_0$ are anywhere within the material boundary.

We plan to use iron pole pieces to energize all of the synthesized fields described in this paper, therfore the behaviour of the polynomials at large distances from the origin is no deterrent to expanding ψ in any outer region as

$$\psi = C_0 + \sum_{n=1}^{N} C_n P_n^* + \sum_{n=0}^{N-1} C_n' Q_n^* \qquad (10a)$$

or what is exactly equivalent, if $C_N' = 0$

$$\psi = \sum_{n=0}^{N} \sum_{k=0}^{n*/2} [C_n + C_n'(\ln r + \phi_k)]A_{n,k}z^{n-2k}r^{2k} \qquad (10b)$$

where

$$A_{n,k} = \frac{(-1)^k n!}{(n-2k)!(k!)^2 4^k}$$

and

$$\phi_k = \begin{cases} 1 & k=0 \\ 1-(1 + 1/2 + 1/3 + \ldots 1/k) & k \geq 1 \end{cases}$$

and $n*$ is the even integer n or $n-1$.

BOUNDARY CONDITIONS

Because the sample shape is here restricted to be a right circular cylinder (or disk) of radius R and length L, it is beneficial to subdivide the outer region at the corners and carry out three separate expansions for ψ. Those for $z<0$ and $z>L$ cannot contain Q^* functions.

From the "inner" field synthesis we know $\bar{H}$ and $\bar{M}$ everywhere within the cylinder. We consider the radial match at $r=R$ and the end match at $z=0$ or $z=L$ separately.

Radial Match

We wish to expand $H_z(z,R)$ and $(H_r+M_r)(z,R)$ in power series form

$$H_z(z,R) = \sum_{n=0}^{N-1} \alpha_n(z/L)^n \qquad (11a)$$

and

$$(H_r+M_r)(z,R) = \sum_{n=0}^{N-1} \beta_n(z/L)^n \qquad (11b)$$

where N is the number of terms that will produce a tolerable error. Although α_n and β_n could be found from matching terms of a Taylor series, we often find it preferable to calculate them from a least squares fit, using the inverse Hilbert Matrix of order N.

In terms of α_n and β_n, the coefficients C_n and C_n' are then found to satisfy

$$C_p = \alpha_{p-1}/(pL^{p-1}) - (\ln R+1)C_p'$$

$$- \sum_{k=1}^{N-p} R^{2k} A_{p+k,k}[C_{p+k}+(\ln R+\phi_k)C_{p+k}'] \qquad (12a)$$

$$C_p' = R\beta_p/L^p - \sum_{k=1}^{N-p} R^{2k} A_{p+k,k}\{2k[C_{p+k} + (\ln R+\phi_k)C_{p+k}'] + C_{p+k}'\} \qquad (12b)$$

Notice that for a given value of n, C_n and C_n' depend only on the values of C_p and C_p' with $p>n$. Therefore, since by design $C_N' = 0$, Eq. (12a) immediately yields C_N. Thereafter, alternating between Eqs. (12b) and (12a) for successively decreasing values of p, produces an unravelling that calculates in order C_N; C_{N-1}', C_{N-2}, C_{N-2}'; $\ldots$; C_0'. The value of C_0 is immaterial and can be set to any convenient value including zero.

End Match

In a like manner, the outer potentials for $z<0$ or $z>L$ can be expanded as

$$\hat{\psi}_{end} = \sum_{n}^{N} \sum_{k=0}^{n*/2} C_n A_{n,k}z^{n-2k}r^{2k} \qquad z \leq 0 \qquad (13a)$$

and

$$\hat{\psi}_{end} = \sum_{n}^{N} \sum_{k=0}^{n*/2} C_n A_{n,k}(z-L)^{n-2k}r^{2k} \qquad z \geq L \qquad (13b)$$

For the $z=0$ end face, matching ψ and H_z+M_z gives

$$C_n = \begin{cases} \dfrac{a_n(0)}{A_{n,n}} & n \text{ even} \\[2ex] \dfrac{a_{n-1}(0)+Mb_{n-1}(0)}{A_{n,n-1}} & n \text{ odd} \end{cases} \qquad (14)$$

where a_n and b_n satisfy Eqs. (6). Similar equations result for the $z=L$ end face.

As an example, assume that the on-axis field in a cylinder of radius $R=1.5mm$ and length $L=5mm$ is required to be

$$H_z(o,z) = 300 + 300z \quad Oe.$$

when the saturation magnetization expressed in gauss is $4\pi M = 1780G$.

A plot of both equipotentials that pass through the corner ($r=R$, $z=0$) of the cylinder determines a region that can be made the same potential by forming it of high permeability iron. The manner in which the outer-field is subdivided by the pole-piece that touches the $r=R$, $z=0$ edge is shown in Fig. 1. Of course, this technique is not feasible should the end match equipotential lie below that of the radial-match potential.
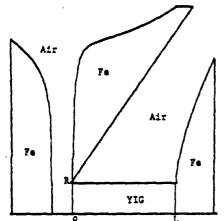

Fig. 1   Pole pieces that synthesize a linear field profile on the axis of a YIG cylinder.

SYNTHESIS OF Hz(r) IN A VERY THIN DISK

In order to normally magnetize a very thin disk of magnetization M so as to produce, within it, a prescribed field $H_z(r)$, it is necessary to first expand it in the form

$$H_z(r<R) = \sum_{n=0} \alpha_{2n} r^{2n} \quad (15)$$

If the film is located at the plane $z=0$ and the outer-potential is expanded as

$$\hat{\psi} = \sum_{n=0} C_{2n+1} P_{2n+1}^o(r,z) \quad , \quad (16)$$

the boundary conditions can be matched (neglecting fringing at the rim) provided $C_1 = \psi_0 + M$ and

$$C_{2n+1} = \frac{(-1)^n n! \ 4^n}{(2n+1)!} \alpha_{2n} \quad n \geq 1 \quad (17)$$

SYNTHESIZED LINEARLY DISPERSIVE MAGNETOELASTIC DELAY LINES

We have used the synthesis procedure outlined above to design and build a special class of magnetoelastic delay lines, namely, linearly dispersive delay lines with wide instantaneous bandwidth. Several attempts [2-4] have been made in the past

to realize such devices but their success was very limited. The difficulty lies in the fact that the required field profile is not achievable in simple YIG geometries immersed in a uniform bias magnetic field. In contrast, we have previously reported[5] success in synthesizing laboratory delay lines and wish here to report our further progress.

First, we review the underlying physical principles of magnetoelastic delay lines and emphasize the areas of importance for improved device operation which require further understanding. Next, we give design parameters. Third, and last, we supply details of device construction and report measured characteristics.

DEVICE PHYSICS

In cases where the internal magnetic field varies slowly enough, spatially, an expansion of the rf fields and magnetization in terms of plane waves is still possible. However, the propagation constant k associated with the wave packet then varies with position. At each internal point z of the single crystal YIG rod, the frequency of the z-directed magnetic spin waves is given by

$$\omega/\gamma\mu_o = H(z) + A/k^2 + Dk^2 \quad (18)$$

where $H(z)$ is the internal magnetic field, γ is the gyromagnetic ratio, and A,D are constants appropriate to the material. The above relation is a simplification only. In reality there is a multitide of modes inversely proportional to k, as shown in Fig. 2a. Also shown in the figure is the ω/k relation of the shear elastic wave which is coupled to the spin waves. This coupling gives rise to the splitting at the crossover point; i.e. the point where the unperturbed frequency values are equal. The longitudinal elastic wave is not important to the delay line operation and is therefore omitted from the figure. In the region of small k, the dominant term is A/k^2 and the group velocity $v_g = \partial\omega/\partial k$ is negative. The wave in this region is called a backward magnetostatic wave (BMW). In the high k region the group velocity is positive and the wave there is termed exchange spin wave (SW).

To understand the operation of the single ended delay line, we follow the path of a particular wave packet of frequency ω_p inside the magnetic medium as shown in Fig. 2b. The path of the wave starts very near the face of the rod (point A in Fig. 2b) in the form of a very low k, backward magnetic wave. This wave is generated by an electromagnetic signal applied to an antenna placed in close proximity to the face of the rod. As the wave packet rapidly penetrates into the rod it encounters a monotonically increasing magnetic field. The initial group (or energy) velocity is very high but decreases rapidly until k reaches the value $k_T = (A/D)^{1/4}$ where the velocity is zero. This point termed the turning point is the point of furthest penetration of the wave into the rod (point B in Fig. 2b). A schematic representation of the group velocity vs. time is shown in Fig. 2c. The time spent in the BMW region is very short, on the order of a few nanoseconds and will henceforth be neglected in the calculation of

the total delay time.

This omission should not be construed as an indication that the BMW region is of little importance in the operation of the delay line. On the contrary, this region where the wave packet initially forms is of crucial importance to efficient delay line operation. Unfortunately, the complicated processes associated with the formation and propagation of the wave in this region are understood only qualitatively and in scant detail. If the magnetic field gradient is comparatively small[6] at the turning point, k will suffer no discontinuity and its magnitude will continue to increase. Except for a small reflection, the bulk of the energy continues along a path of increasing (k) into the exchange spin wave region.

The wave trajectory is now toward the front face of the rod in the direction of decreasing magnetic field. In this SW region, it is necessary to consider both the radial and axial components of the magnetic field. Certain radial distributions tend to bend the wave away from the axis, that is defocus the coherent energy beam while other profiles tend to focus it toward the axis. It is very important to ensure the existance of focussing conditions since very high propagation losses occur otherwise. Too much focussing, on the other hand, is counterproductive since it saturates the propagation channel by creating local regions of extremely small cross-section and thus of high energy density. This tendency to premature saturation limits the power handling capabilities of the delay line and hence its useful dynamic range.

The determination of whether a focussing or a defocussing condition exists may be made by evaluating a dimentionless quantity Q that is a function of the H-field and its first and second spatial derivatives, evaluated at the axial point z under consideration[6]. A concave field profile (H''<0) automatically ensures focussing but a slightly convex profile is also allowed.

Provided a focussing condition exists, the beam propagates to the left until k reaches the value $k_x = \omega/v$, where v is the velocity of the elastic

shear wave. This is defined as the cross-over point where the unperturbed frequencies of the elastic and spin waves are equal (point C in Fig.2b). The distance between the turning point and the cross over point traversed in this region is very small, but the wave on the other hand is a slow one with its maximum velocity reached at the cross over point. As a result, the time spent in the SW region accounts for a major portion of the total delay time (more than half in the case of a linearly varying field profile). Representative values of the distance and velocity for YIG at 4 GHz and a magnetic field gradient of 10^4 Oe/cm are 20mm for the distance and 1.15×10^4 cm/sec for the maximum velocity. This velocity is only 3% of the shear elastic wave velocity.

The coupling between the spin wave and the elastic wave causes a substantial conversion of the spin wave packet into an elastic shear wave at the cross-over point. Under the same stipulations as before, namely that the field gradient is not too steep, very high conversion efficiencies are possible. The elastic wave continues to propagate

unaffected by the magnetic field towards the face of the rod where it undergoes a reflection in the highly polished surface (point D in Fig. 2b). From this point the wave packet retraces its former steps through the SW and BMW regions and is picked up at the surface in the form of an electromagnetic wave. This may be done by the same antenna used to launch the input signal, or by another antenna placed in close proximity to it when two port operation is desired. The delayed signal whose rather complex trajectory we have just finished describing, is the main output of the delay line, the so called 1st echo. Not all the wave energy, however, is extracted by the receiving antenna and the unextracted portion is launched back into the crystal to arrive back at the rod face as a 2nd echo. This spurious signal is delayed by twice the delay of the 1st echo and is of reduced amplitude. Higher-order echoes exist as well at further reduced amplitudes.

When two port operation of the single ended delay line is required, the direct electromagnetic feed the rough between the input and output antennae which are at close proximity causes another spurious output signal. This sometimes bothersome spurious whose high amplitude had been reported,[5] could be reduced substantially by improving the wave coupling antennae.

The total transit time of the 1st echo is the sum of the times spent as an exchange spin wave and as an elastic shear wave. This is given by

$$T = \frac{2z_x}{v} + 2 \int_{z_x}^{z_x} \frac{dz}{v_g} \qquad (19)$$

where z_T, z_x are the positions of the turning point and the cross-over points respectively, v is the velocity of the elastic shear wave, and $v_g = \partial\omega/\partial k$ is the group velocity. In the above expression for evaluating T we neglect the transit times through the BMW and the cross over regions.

We therefore assume $\omega/\gamma = H(z) + D_{ex}k^2$, and by expanding H(z) in a Taylor series around z_x, obtain the approximate expression for T

$$T = \frac{2z_x}{v} + \frac{2\omega}{\mu_0 \gamma H' v \beta} \tan^{-1}\beta \qquad (20)$$

where $\beta = \omega\sqrt{2D_{ex}H''}/vH'$ is a dimensionless parameter, H', H'' are the first and second spatial derivatives of the axial magnetic field evaluated at the cross over point z_x, and D_{ex} is the exchange constant. For YIG, when converted to CGS units, $D_{ex} = 5 \times 10^{-9}$ Oe cm^2, v = 3.84×10^5 cm/mc and $\gamma = 2.8$ MHz/Oe. In evaluating T in the above equation, we assumed $k_T = 0$ and $k_x = \omega/v$.

Equation (20) for T, can be used to compute the delay time for a given field profile or alternatively to synthesize the necessary profile for achieving a desired delay characteristic. In the latter case, $T(\omega)$ is a given function of frequency. When a field synthesis is attempted, a word of caution is appropriate. For a specified

$T(\omega)$, the synthesized field profile may turn out to be physically unrealizable or if physically possible, might turn out to be a defocusing profile, rendering it impractical. For example, the profile proposed for a constant delay[8] is a highly defocusing one.

In the limits of $D_{ex}=\beta=0$ we obtain from Eq. (20) the position z_x as

$$z_x = \frac{1}{\mu_o YH} \int_0^{\mu_o YH} T(\omega)d\omega + C \qquad (21)$$

where C is an integration constant whose value may be chosen at will.

The field profile as a function of position z along the axis of the rod can be found by inverting the above expression for z_x. When higher accuracy of the prescribed delay characteristics over wide instantaneous bandwidth is required, a better determination of the field profile may be warranted.

An important delay characteristics is a linear dispersion where the dealy time increases linearly with frequency. In this case $T=T_o+D\omega$. By solving Eq. (21), and when $C=0$ is chosen, the required axial field profile is a linear one, given by

$$H = -\frac{2T_o}{YD} + \frac{4z}{YvD} \qquad (22)$$

The linear dispersion coefficient D, is therefore given by $D=4/\mu_o YvH'$ whre H' is the field gradient. When $C\neq0$ is chosen, the resulting profile is non-linear.

DESIGN PARAMETERS

The most important operational parameters in this class of devices together with our design goals are listed below:
Insertion loss and flatness
For the device to be of practical use, it should have no more than a moderate amount of insertion loss and reasonable variation of such losses across the frequency band. Obviously any matching arrangement to minimize the loss has to be broad band since no external tuning at each frequency is allowed.
Linear dispersion value and accuracy
Potential uses of and interest in devices posssing a wide range of dispersion factors exist. Based on our laboratory experience, we feel that values from $D=.1NS/MHz$ to 2 NS/MHz are currently achievable, not necessarily over the same bandwidth. For certain applications a useful criterion is the time bandwidth product defined as $D^2\Delta\omega$ and a practically achievable number of >500. The deviation from linearity is also dependent on the bandwidth and values in the 1-3% range over bandwidth of up to 1500 MHz are achievable. There is a wide room for tradeoffs among the three parameters dispersion value, allowable percentage deviation from linearity and frequency bandwidth.
Frequency range and instantaneous bandwidth
Aside from bandwidth limitations which can be traded off as discussed above, there is an upper limit imposed by the appearance of the spurious 2nd echo. As was earlier explained, the 1st echo generates its own echo and the 2nd echo free bandwidth is therefore defined as the $\Delta\omega$ over which the only delayed output present is the 1st echo. This bandwidth increases upon increasing the frequency (an octave being the theoretical maximum) and a 1GHz or more at s band was set as a goal. Device operation in the frequency range of .5-5GHz has been verified with 5GHz being a laboratory instrumentation limitation. We belive that useful operation at C and possibly x bands in feasible with instantaneous bandwidth exceeding 2GHz.
Input/Output isolation
Since the nondispersive electromagnetic leakage appears instantly at the output, a high amplitude may be tolerable for certain applications. For some important applications, however, this is not so. Although it may seem that due to the close proximity of the input and output antennae, high isolation could not be achieved, our design goal was to limit the leakage to a level at which its amplitude is no higher than the amplitude of the 1st echo signal.
Dynamic range
Our delay line is a magnetic device and like all such devices, its behavior changes drastically when high power rf signals are present. These high power effects limit the dynamic range for useful operation. Since high energy densities are the culprits an obvious way to increase the dynamic range is to increase the effective cross sectional area of the signal. This may be accomplished by optimizing the coupling to the BMW and/or by decreasing the amount of focussing of the signal while it traverses the exchange spin wave region. As large a dynamic range as possible is obviously desirable for many applications. For our ealier work we achieved ranges of 25-30db, and any improvement was deemed welcome.

DEVICE CONSTRUCTION AND MEASURED CHARACTERISTICS

An exploded view of a packaged device is shown in Fig. 3. Notice the position of the YIG rod between the synthesized soft iron pole pieces. The pole pieces were designed to implement the radial match only. Other surfaces were omitted to allow access for the wave coupling structure. The resultant internal field is therefore only an approximation to the exact requirement. Its axial position is adjustable, and it is held securely by the tension supplied by the adjustment screw in the front, and the locking cylinder, which presses on the back pole pike, at the back. The input and output antennae which are loops of 5 mil enameled wire soldered to semirigid cables, are pressed to the front face of the crystal by a small cylindrical teflon piece. The diameter of the loops is 30 mils and they are placed side by side off the center of the face of the YIG rod. The parallel feed lines joining each loop to the semirized cable intersect at approximately 90° on the face of the rod. The magnetic flux is supplied by Alnico 8 permanent magnet rings. The dimensions of the package are 2" dia. by 2 1/2" long and it accomodates a 120 mils dia. by 200 mil long (100) YIG rod. Smaller size packaged devices have been built and successfully tested.

With the improved coupling structure described above we observed simultaneous improvement in several device characteristics. Specifically, overall

insertion loss was reduced by up to 10db; loss ripple was limited to 1-3 db; dynamic range measured between the noise floor and the onset of nonlinear high power effects increased by at least 10db; electromagnetic leakage feedthrough could be reduced to a level at which it was equal to or lower than the level of the frequency dispersive time-delayed primary signal. Input/output isolation increased as a result by up to 20db. The spurious 2nd echo signal could also be suppressed to levels lower than the signals' by up to 20db.

In Figure 4 we see oscilloscope traces which highlight the characteristics of a representative packaged device operating at S band. The device contained synthesized pole pieces designed for a field on axis of 300+300z (z in mm). In all four parts of the figure short input pulses, 40 NSec wide, were applied.

Part (a) shows the output obtained at discrete input frequencies as marked. The 1st and 2nd echoes are seen to be delayed in proportion to the frequency, the latter at twice the rate of the formers. The leakage feedthrough is not time-delayed and its position does not vary with frequency. We see that the amplitudes of the spurious leakage and 2nd echo signals are lower than that of the primary 1st echo signals, the latter by as much as 20 db. By sweeping the short input pulses across the frequency band and applying the sweeping voltage ramp to the vertical axis of the oscilloscope, the frequency vs. delay time dependence is obtained. This is shown in part (b). The dispersion is .3 NSec/MHz and the frequency band 1000MHz. The linearity of the dispersion is quite good with a 2% deviation from a straight line observed. By removing the sweeping ramp from the vertical axis of the oscilloscope while continuing to sweep the input signal, we obtain part (c) which shows the amplitude of the output signal as a function of its frequency. The insertion loss of the primary 1st echo is 27-30 dB across the 1000 MHz frequency band and a negligible amount of signal distortion is observed. The spurious signals are at reduced amplitudes with input/output isolation of 33-40 db, and 2nd echo levels of 15-29 db below the levels of the primary 1st echoes.

Part (d) shows operation at the fixed frequency of 2.8 GHz where the input power increases from the upper trace downwards. The relative input power levels are marked in the figure. The lowest trace clearly shows the nonlinear high power effect on the signal; the output pulse shows signs of a breakdown and is no longer a delayed replica of the input. A complete breakdown occurs upon a further increase in the input power (not shown in the figure). The threshold level at which nonlinear response sets in is app. -10bm and the dynamic range for linear operation is 44db. This was measured in a setup which included a 47 db S band amplifier with a 5 db noise figure. It can be seen in part (d) that the 2nd echo saturates at lower power levels than the 1st echo. This suggests that the energy density of the signal tends to increase in proportion to its delay time and hence that smaller dynamic ranges are to be expected in delay lines exhibiting long delays. This tendency may be offset in low focussing internal magnetic field profiles where the signal energy densities are lower.

The magnetic field on the axis of the YIG rod, calculated by fitting the data represented in Fig. 4 to Eq. (20) for the delay time T, is $H_z(r=0) = 690+1240z - 454z^2$ Oe (z in mm). This field is quite different from the assumed field at the outset of the synthesis. Two points should be borne in mind in connection with this discrepency. The first one is that, as mentioned above, only the radial match of the synthesis was implemented. This will distort the field in the active region of the delay line which extends to a depth of only 1-2mm into the YIG rod. The field on the axis of a naked YIG rod; when placed in a uniform DC bias field, has a very small linear and a large quadratic spatial coefficients. The required axial field on the other hand, is drastically different, having no quadratic and a large linear coefficients; this difference has to be overcome by the synthesized pole pieces.

The second point is, that a set of pole pieces designed for a specific field profile is capable of sypporting a whole family of profiles by adjusting the flux passing through them. This is analogous to the case of a capacitor where the electric field may be varied by adjusting the charge accumulated on its plates. The most advantageous field profile for efficient device operation as determined by rf considerations, may not be the original profile from which the pole pieces were originally synthesized.

References

1. F.R. Morgenthaler, "The Synthesis of Cylindrically Symmetric Static Magnetic Fields in a Locally Saturated Ferromagnet," AIP Conference Proceedings No. 24, Magnetism and Magnetic Materials, 503, (1974).

2. For a general review and references to pre-1970 work see B.A. Auld in Appl. Solid State Science, Vol. 2, Academic Press (1971).

3. R.A. Moore, G.J. Moussally, IEEE, M.I.T.-19, 334 (1971).

4. R. Dötsch, JAP, 43, 1923 (1972).

5. A. Platzker, F.R. Morgenthaler, AIP Conference Proc. No. 29, Magnetism and Magnetic Materials, 645, (1975).

6. J.L. Doane, Technical report 22, Microwave and Quantum Magnetics Group, M.I.T. Center for Materials Science and Engineering, June 1970.

7. F.R. Morgenthaler, IEEE, MAG-8, 550, (1972)
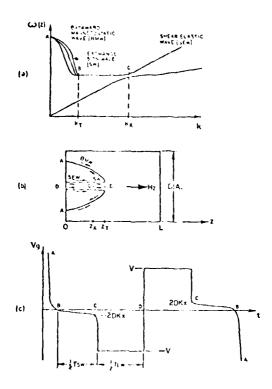
8. B.A. Auld, W. Strauss, JAP 37, 983 (1966).

Fig. 2   Diagrams explaining magnetoelastic delay
line operation: (a) ω-k relation,
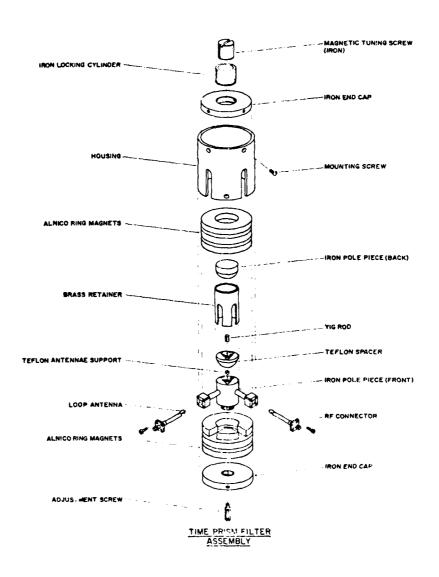(b) axial cross-section of the YIG rod
(c) group velocity vs. time.

MAGNETIC TUNING SCREW (IRON)

IRON LOCKING CYLINDER

IRON END CAP

HOUSING

MOUNTING SCREW

ALNICO RING MAGNETS

IRON POLE PIECE (BACK)

BRASS RETAINER

YIG ROD

TEFLON SPACER

TEFLON ANTENNAE SUPPORT

IRON POLE PIECE (FRONT)

LOOP ANTENNA

RF CONNECTOR

ALNICO RING MAGNETS

IRON END CAP

ADJUSTMENT SCREW

TIME PRISM FILTER
ASSEMBLY

Figure 3 Exploded view of packaged delay line
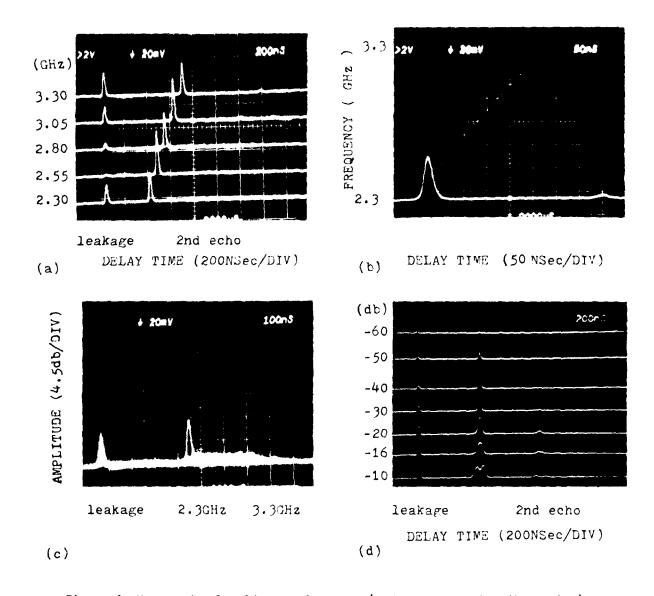
Figure 4 Measured delay line performance (refer to text for discussion).

The following sets of figures provide further information concerning the characteristics of the Time Prism Filters that were developed by employing the field synthesis techniques.
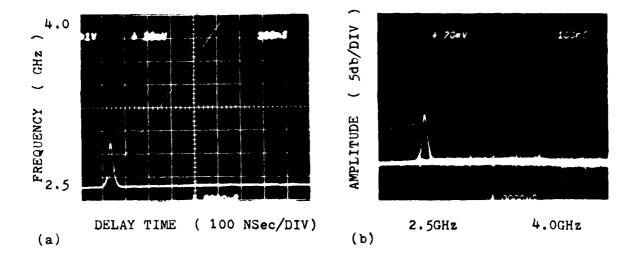
Figure 1. Characteristics of packaged device after its removal from the magnetizing field. (a) Frequency as a function of delay time with a straight line superimposed for comparison.The dispersion is .35NSec/MHz. (b) Signal amplitude as a function of frequency.Insertion loss 39-45 db.
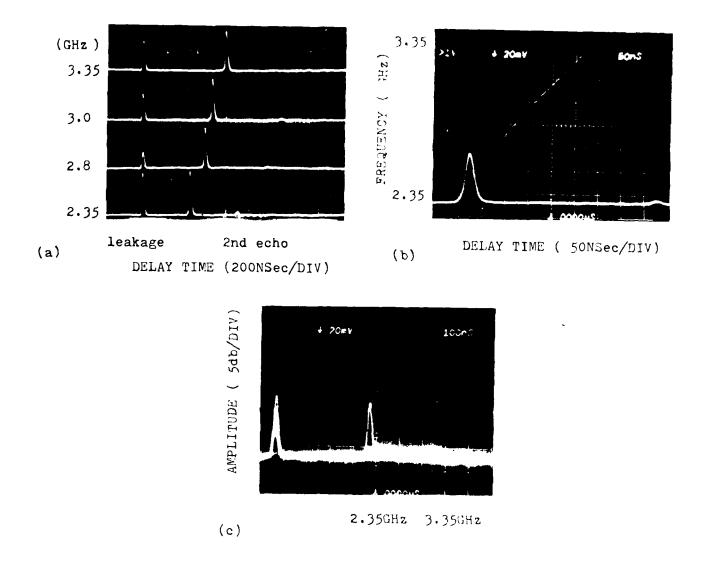
Figure 2. Time Prism characteristics after coupling optimization.
(a) Device output at four distinct frequencies as marked.Leakage amplitude
equal to or lower than first echo. (b) Frequency as a function of delay
time.Dispersion is .3NSec/MHz. (c) Signal amplitude as a function of
frequency.Insertion loss 32-35db,leakage amplitude lower than or equal to
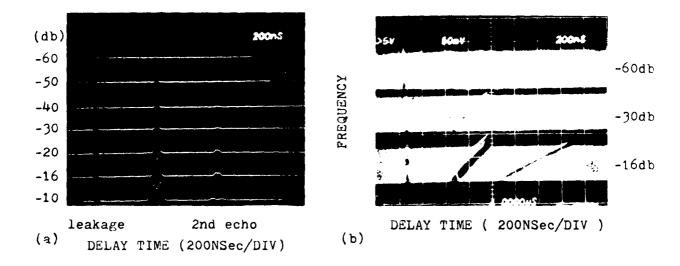first echo,second echo amplitude lower by at least 15db.

Figure 3. Dynamic range.Relative input power is as marked. (a) Fixed frequency 2.8 GHz.Lowest trace shows nonlinear high power effects,linear dynamic range 44db. (b) Full band **sweep of 1000MHZ in each trace,**linear dynamic range 44db
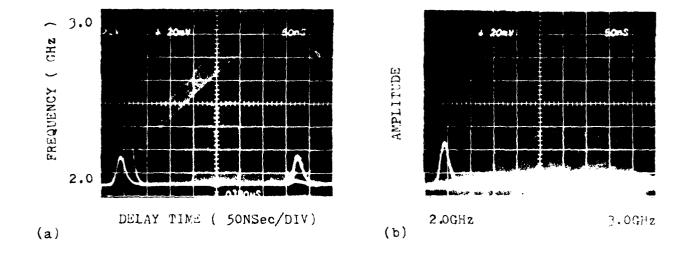
Figure 4. Characteristics of a filter in a laboratory setup. (a) Frequency
as a function of delay time. Dispersion is .38 NSec/MHz. (b) Signal ampli-
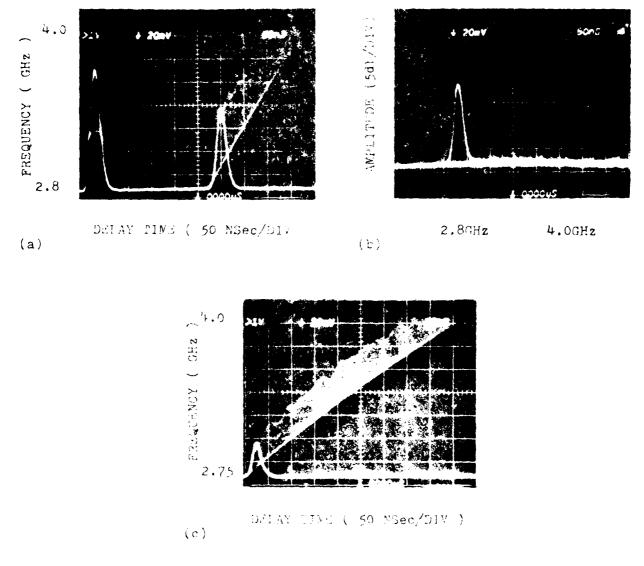tude as a function of frequency.Very flat insertion loss of 35±.5db

Figure 5. Filter characteristics in a laboratory setup. (a) Frequency as a
function of delay time, low dispersion .17 NSec/MHz. (b) Signal amplitude as
a function of frequency under same conditions as in (a), low insertion loss
25-28 db across 1200 GHz. (c) Different settings from those in (a)&(b), same
pole pieces and YIG rod. Dispersion of .38NSec/Hz, deviation from linearity
of less than 1.5% across a 1200MHz bandwidth, very flat insertion loss 33±.5db
T(2.75GHz) = 680 NSec.

(a) DELAY TIME (50 NSEC/DIV)

(b) DELAY TIME (100 NSEC/DIV)
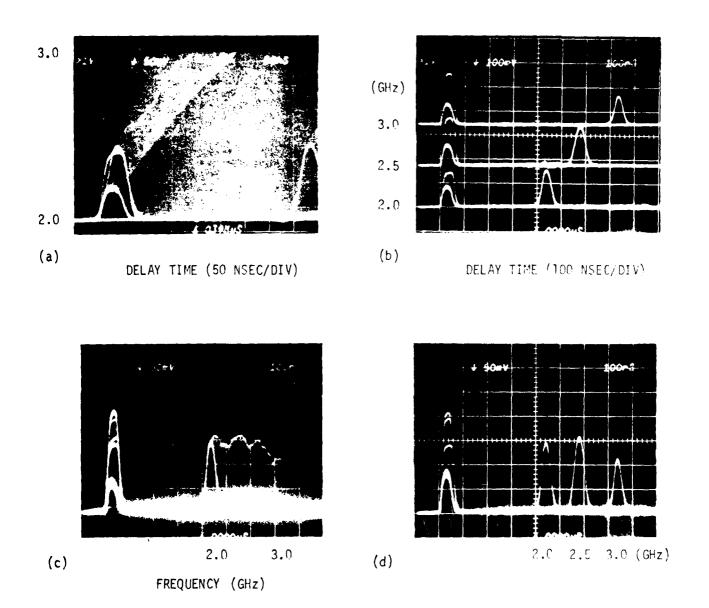
(c) FREQUENCY (GHz)

(d) 2.0 2.5 3.0 (GHz)

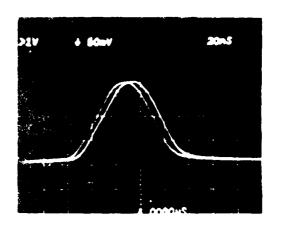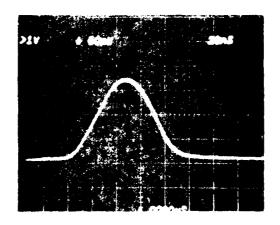FIGURE 2

OUTPUT OF TIME PRISM MICROWAVE PULSE ANALYZER. (a) FREQUENCY/DELAY
TIME CHARACTERISTICS, SWEPT INPUT. (b) RESPONSE TO THREE DISTINCT IN-
PUT FREQUENCIES, VERTICAL POSITION PROPORTIONAL TO FREQUENCY. (c)
AMPLITUDE AS A FUNCTION OF FREQUENCY, SWEPT INPUT. (d) SUPERPOSITION
OF SYSTEM RESPONSE TO THREE DISTINCT INPUT FREQUENCIES. ALL INPUTS
ARE CW AND APPLIED TO INPUT 1, GATING IS INTERNAL.

(a)

(b)

(c)

RESPONSE OF TIME DOMAIN MICROWAVE PULSE ANALYZER TO TWO
SIMULTANEOUSLY APPLIED CW SIGNALS. (a) f_1 = 2.9 GHz,
$\Delta f = f_2 - f_1$ = 50 MHz (b) Δf = 25 MHz (c) Δf = 2.5 MHz

Thin Film Input/Output Coupling Structures

The antennae are the major components in determining both isolation from input to output and the coupling efficiency. Previously optimization of these two specifications was difficult at best due to a number of problems inherent in using hand formed loops, including: (1) inability to make reproducible loops, (2) questionable reliability of wire loops due to embrittlement from work hardening, (3) limited isolation due to overlapping of input and output loops. The proposed design attempts to overcome these difficulties. The thin film antennae will: (1) be reproducible, given a design mask, (2) not be subject to embrittlement through work hardening, because the antennae will be sputtered and etched on a rigid substrate of alumina, (3) improve isolation with nonoverlapping loops and perhaps ground separators. In addition to accommodating for proposed antennae, the proposed delay line fixture should allow for interchanging of the iron pole pieces, which shape the magnetic field applied to the YIG rod. Ultimately this ability to interchange pole pieces and antennae will open the way for a future series of experiments to maximize power handling capabilities, minimize attenuation and maximize antennae isolation and coupling.

The SM thesis of Leslie Itano, now nearing completion, has as its main goal the design of a magnetoelastic delay line utilizing thin film input and output antennae. Previous delay lines utilized resonant cavities or hand formed wire loops to provide the electromagnetic input pulse and recieve the output pulse. Although the delay line performance with the hand formed wire loops was excellent, the results were extremely difficult to reproduce, requiring many hours of pain-staking initial assembly work and many more hours of tuning at the test bench for each antennae pair. Then, with all this loop adjustment, the wires sometimes became work hardened and embrittled, resulting in highly tuned out unreliable antennae. In contrast, the thin film antennae are made photolithographically

using a mask with a specific design. This method produces consistent, easily reproducible and reliable results. The fabrication time for thin film circuits is also significantly less due to several factors. First of all, a pair of antennae is produced on a single substrate so that several substrates can be processed simultaneously. Secondly, once a substrate has been processed and the antennae pair is etched onto the substrate, the circuit is fixed. The thin film antennae are not malleable like the wire loop antennae, eliminating the tuning step and further reducing fabrication time. Thus, the thin film antennae is not only more reproducible and reliable, but it requires less fabrication time than the hand formed loop antennae.

A secondary achievement of this thesis is the design of a flexible delay line fixture. By "flexible", we mean that the fixture is designed to allow for a range of antennae of substrate thickness, pole pieces which shape the internal rod profile, and thin film antennae designs. This ability to interchange components, and to interchange them quickly makes this design well suited to research.

This new fixture design also retains the advantages of previous designs. The new fixture is compact; it can be self-contained since allowance is made for the use of ring magnets. The pole pieces have been synthesized to provide linear dispersion.

Description of Fabrication Sequence (Summary)

This section, which will form a portion of Itano's thesis, describes the **fabrication of the YIG** delay line. First, an overview of the fabrication, and associated problems will be presented. The three major categories which will be included are: (1) producing the thin film antennae, (2) manufacturing the fixture, and (3) assemblying the delay line. Second, a summary of the fabrication sequence will be provided as an aid for subsequent work.

4.A. Producing Thin Film Antennae

The first step in producing a thin film antennae is mask fabrication. This step involves designing the antennae, reducing the pattern and transferring it to a glass photographic plate. This glass plate, complete with antennae pattern, is the mask. In the meanwhile, an alumina substrate has been sputtered by an outside recorder with thin film chrome-gold. The thin layer $(100-200 \overset{\circ}{A})$ of chromium acts as an adhesion layer between the substrate and the thicker gold-layer (200 micro inches). The mask is now used as a photolithographic negative to selectively etch both chromium and gold layers; the pattern remaining on the substrate is the thin film antennae.

Developing Etching Process

The complete "etching process" for thin film chromium gold circuits has been well established. In this overview,

we will first review the general process, explaining the necessity of each step. Next, we describe the special "challenges" presented by the antennae designed for this thesis, and the attempts to overcome these challenges. Lastly, we summarize the final approach used in this thesis.

The "etching process" begins by spinning on a thin layer of photosensitive, etch resistant liquid to the substrate. The spin rate and viscosity of this "photoresist" liquid determine the thickness of this layer. The substrate is then "prebaked" to harden the photoresist, making it more resistant to breakdown, i.e., local voids or weak points in the photoresist caused by handling in the exposure step to follow. "Breakdown" in the photoresist will allow the etchant to seep in, etching the gold and/or chromium.

The glass mask already prepared is a negative; that is, the design area is blackened, blocking out light, while the remaining area is totally transparent. This mask is aligned to the substrate edges, contact is made with the substrate, and the photoresist is exposed to ultra violet light in those areas where the mask is transparent. The photoresist is chemically developed, toughening all of the unexpected areas. The exposed areas are washed away, leaving behind the design's protective photoresist pattern. The substrate is "postbaked" to toughen the remaining photoresist.

Since the design area is completely protected by photoresist, the remaining unprotected area can be etched away.
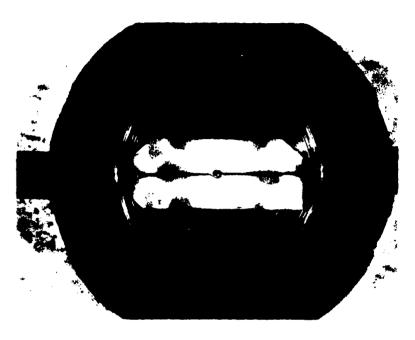
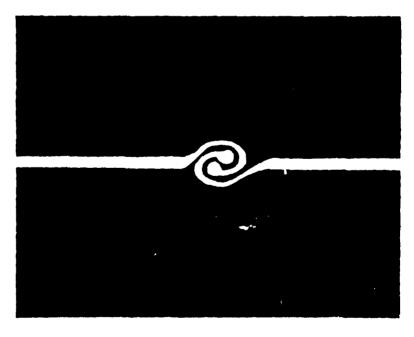Figure 4.1a - Thin film antennae designed, set in delay line
housing

Figure 4.1b - Enlargement of coupling region

The top gold layer is etched first with a potassium iodide solution, while the lower chromium layer is etched with a $KMnO_4$ and sodium hydroxide solution. Finally, the protective photoresist layer is stripped away with an industrial stripper, leaving behind the intact design pattern.

The antennae designed for this thesis (see Figure 4.1) requires several sputtered through via holes to ground in close proximity to narrow (3-4 mils wide) lines. The challenge was to protect the via holes without bridging over to the narrow lines. Using the established processes and taking no special precautions to protect the via holes, gold etch seeped into the holes, partially etching the insides of the holes. Also large voids were present in those regions where the photoresist layer was particularly thin, such as the edge of the via holes. The first attempt to solve this problem was a fourfold increases in the photoresist thickness (to 4 micron). As hoped, this change resulted in improvement coverage for the via holes; however, voids still appeared at the edges. In addition, the etch factor has increased significantly, causing a dramatic change in line width or effective line impedence. The etch factor, as shown in Figure 4.2, is the difference between the top surface or apparent edge of the photoresist and the edge of the etched line. In general, the etch factor can be due to breakdown or softening of the photoresist edge which allows the etchant to seep underneath. In the case of the thicker photoresist, the increase in etch factor is likely due to diffraction of the
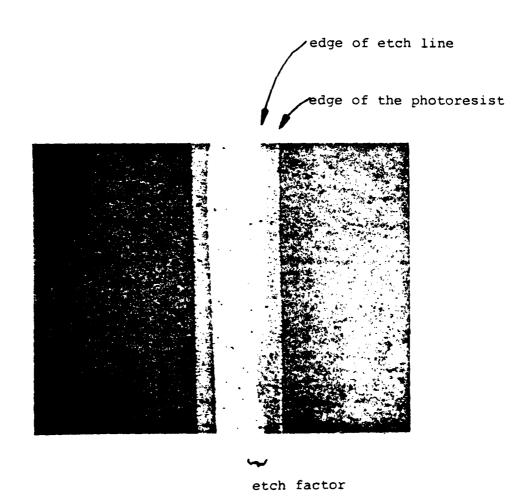
Figure 4.2 - Etch factor

exposure light. Figure 4.3 illustrates how this diffraction causes extra exposure of the thicker photoresist near the conductor surface, exactly where its protection is needed. Figure 4.4 shows how a vertical visual inspection completed before etching would not detect the diffraction caused difference between conductor surface or effective photoresist edge and top surface or apparent photoresist edge. So this modification brought some improvement, but proved to be more problematic than helpful.

Returning to the original 1 micron thick photoresist layer the etch factor was further improved by increasing the postbake temperature from $90^{\circ}C$ to $150^{\circ}C$. This seemed to further harden the photoresist edges, resulting in less etchant seeping underneath and etching the metallic layer.

The remaining problem of protecting the sputtered through holes was solved by manually applying a thick, acetone based resist to the holes with a few strands from a camel hair brush. Since the holes were only 3 mils in diameter with adjacent conductor lines only 2-3 mils away, this task requried steady hands, but resulted in totally protected sputtered through holes.

4.B.   Manufacturing the Fixture

Manufacturing the delay line fixture involves designing the components of the housing and then machining them. Since rusting of the pole pieces had altered the field profile of previous efforts,   these parts were flashed with Ni for protection.
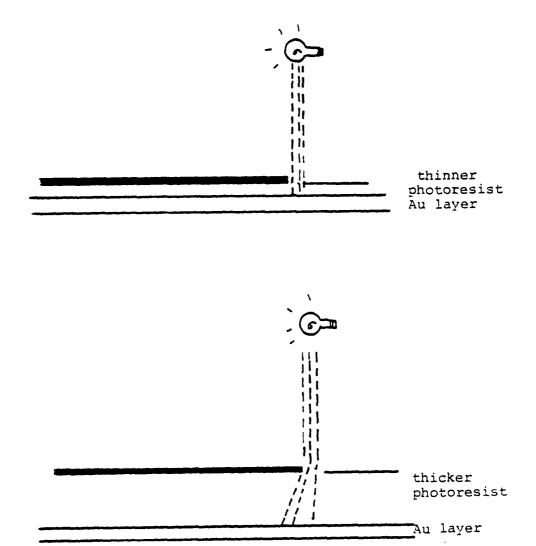
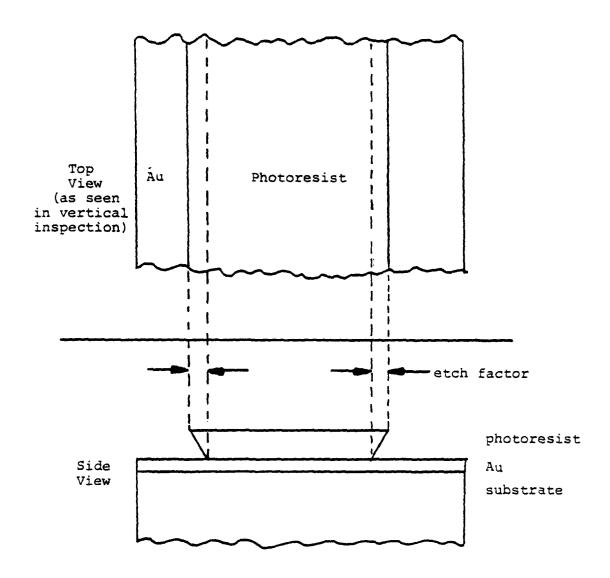Figure 4.3 - Diffraction effect on photoresist

Figure 4.4 - Shows how vertical inspection does not detect
diffraction caused etch factor

4.C. Assemblying the Delay Line

The final delay line assembly starts by putting together the connectors and main housing (see Figure 4.1). The next step is to fix all of the flexible parameters, including raising the front pole piece to compensate for the substrate thickness, installing the specially designed pole pieces, and epoxying the thin film antennae to the front pole piece. The electrical connections between the substrate and coaxial connectors are made with a 1 mil x 25 mil x 100 mil gold ribbon which has been gap welded to the substrate, then epoxied to the connector. Gap welding is a general technique for thermal compression bonding gold ribbon to gold metallization (including thin film gold metallization). After finally installing the remaining components, including YIG rod, front pole piece and retainers, the delay line is complete and ready to test.

The following detailed summary is provided as aid for subsequent work:

Description of Antennae Fabrication

  A. Mask Fabrication

    1. Design antennae

    2. Transfer design (at 20x) to rubylith

    3. Photoreduce patterns

    4. Transfer (xl) patterns to glass photographic plates

  B. Sputtered Substrate Procurement

1. Order alumnina to size--15 mil thickness ordered
    to minimize gap between rod and pole piece.
    Width and length determined by fixture.

2. Order holes drilled for sputtered through holes

3. Sputter substrates with chrome (for adhesion) and
    200 µ inches of Au.

C. Substrate Etching Summary

1. Spin AZ 1350J photoresist on to metallized
    substrates.

2. Bake substrates at 90° for 25 min. to dry photo-
    resist.

3. Align glass photographic mask to both substrate
    edges and sputtered through hole sites.

4. Expose photoresist with ultraviolet light,
    using glass photographic mask as a negative.

5. Apply protection paint to sputtered through
    holes.

6. Develop photoresist with Shipley AZ Developer,
    removing exposed portions of photoresist.

7. Postbake substrates at $150^{\circ}C$ for 25 min. to
    toughen photoresist.

8. Make batches of both chromium and gold etch
    solutions as follows:

Gold Etch Solution

    0.324 grams I (solid)

  + 1.134 grams KI

    50 milliliters water

Chromium Etch Solution

    3.25 grams $KMnO_4$

    3.25 grams NaOH

    50 milliliters water

9. Etch away exposed gold and chrome metallizations.

10. Strip remaining photoresist with Allied Chemical A-20, a phenol based industrial stripper.

D. Housing Construction

1. Design housing

2. Machine housing

3. Apply Ni flash

E. Final Delay Line Assembly

1. Assemble coaxial connectors

2. Gapweld Au ribbon to antennae input and output

3. Screw front pole piece into main housing, adjusting height so that substrate surface is 5-10 mils below connector height.

4. Attach substrate, antennae side up, to front pole piece with Ag point. Antennae input and output must line up with connectors.

5. Attach Au ribbon to connectors with Ag epoxy

6. Assemble balance of delay line, including back-pole piece, YIG rod, teflon rod retainer, fixture retainer.

Appendix A - Pole Piece Design

I. Overview

This appendix outlines the synthesis procedure developed by Morgenthaler and Platzker [19]. Although more general cases can be treated using similar methods, this discussion will be restricted to the synthesis of cylindrically symmetric fields where the material shape is a cylinder or disk. The logic behind the pole piece design is as follows. The magnetic potential inside the cylindrical material is determined by an appropriate series expansion once the axial magnetic field, $H_z(0,z)$, is specified. The space outside the cylinder is then divided into separate regions. Within each outer region, an appropriate selection of functions is made with which to expand the Laplacian magnetic potential in that region. The coefficients for each outer region expansion are then determined by matching boundary conditions with the inner potential so that the error is minimized in a least squares sense.

Once the outer potential has been determined, the edges of pole pieces which surround the cylinder can be designed to coincide with lines of equipotential. With the application of an appropriate dc magnetic field, the pole pieces become energized so as to produce the correct outer field and consequently the correct axial magnetic field in the cylinder. It is important to realize that although an infinite number of combinations of material size, shape, and pole piece design exist, all of which would create the desired field, once one has been chosen the field it creates is unique [18].

II. Inner Field Determination

The equations governing the dc H field in a ferro-magnet that is everywhere locally saturated are

$$\overline{M} \times (\overline{H} + \overline{H}^a) = 0 \qquad \text{(A.1.a)}$$

$$\overline{M} \cdot \overline{H} > 0 \qquad \text{(A.1.b)}$$

$$|\overline{M}| = M \qquad \text{(A.2)}$$

$$\nabla \times \overline{H} = 0 \qquad \text{(A.3)}$$

$$\nabla \cdot (\overline{H} + \overline{M}) = 0 \qquad \text{(A.4)}$$

where $\overline{H}^a$ is an effective magnetic anisotropy field which may be ignored initially. In terms of the inner scalar magnetic potential ψ, the relations

$$\overline{H} = - \nabla\psi \qquad \text{(A.5)}$$

and

$$\overline{M} = - \frac{\nabla\psi}{|\nabla\psi|} \cdot M \qquad \text{(A.6)}$$

satisfy equations (A.1), (A.2), and (A.3). These equations may be substituted into equation (A.4) to arrive at

$$\nabla \cdot \left[(1 + \frac{M}{|\nabla\psi|}) \nabla\psi \right] = 0 \qquad \text{(A.7)}$$

In the limit as $|\nabla\psi| \to \infty$, the non-linear portion of equation (A.7) goes to zero and the equation becomes Laplace's equation. Thus if the magnitude of $\overline{H}$ grows as distance from the cylindrical axis increases, then at the radial boundary the inner field potential should be approximately Laplacian. This aids the matching of boundary conditions with the outer field, which is Laplacian.

The axis of the cylindrically symmetric ferromagnet is assumed nonsingular, so an appropriate expansion of ψ is

$$- \psi = \sum_{n=0}^{\infty} a_{2n}(z) \ r^{2n} \tag{A.8}$$

so that $\quad \bar{H}(r,z) = \hat{1}_z \sum_{n=0}^{\infty} a'_{2n}(z) \ r^{2n}$

$$+ \hat{1}_r \sum_{n=0}^{\infty} 2(n+1) \ a_{2(n+1)}(z) \ r^{2n+1} \tag{A.9}$$

where $\hat{1}_n$ is the unit vector in the nth direction and the primes denote differentiation with respect to z. Expanding $\bar{M}$ separately as

$$\bar{M}(r,z) = M[\hat{1}_z \sum_{n=0}^{\infty} b_{2n}(z) \ r^{2n}$$

$$+ \hat{1}_r \sum_{n=0}^{\infty} b_{2n+1}(z) \ r^{2n+1}] \tag{A.10}$$

allows the use of equations (A.1), (A.2), and (A.4) to determine constraints on the a_i and b_i coefficients.

Use of equation (A.1.a) results in

$$M(\sum_{n=0}^{\infty} a'_{2n}(z) \ r^{2n})(\sum_{n=0}^{\infty} b_{2n+1}(z) \ r^{2n+1})$$

$$- M(\sum_{n=0}^{\infty} b_{2n}(z) \ r^{2n})(\sum_{n=0}^{\infty} 2(n+1) \ a_{2(n+1)}(z) \ r^{2n+1} = 0$$

where M may be factored out as assumed non-zero. Multiplying out and collecting terms yields a polynomial in r,

$$\sum_{s=0}^{\infty} \{[\sum_{n=0}^{\infty} (a'_{2n} \ b_{2(s-n)+1} - 2(s+1-n) \ a_{2(s+1-n)} \ b_{2n})] \ r^{s+1}\} = 0 \tag{A.11}$$

Since this equation must be satisfied for all r, we must have that

$$\sum_{n=0}^{s} (a'_{2n} \ b_{2(s-n)+1} - 2(s+1-n) \ a_{2(s+1-n)} \ b_{2n}) = 0 \tag{A.12}$$

for s = 0, 1, 2, 3, ... This gives the first constraint on the coefficients. However, equation (A.1.b) also re-

stricts the sign of $a_0' b_0$ to be $a_0' b_0 > 0$.

Use of equation (A.2) results in

$$\left(\sum_{n=0}^{\infty} b_{2n}(z) r^{2n}\right)^2 + \left(\sum_{n=0}^{\infty} b_{2n+1}(z) r^{2n+1}\right)^2 = 1$$

Multiplying out and collecting terms yields a polynomial in r,

$$b_0^2 + \sum_{s=0}^{\infty} \left[\sum_{n=0}^{s} (b_{2n+1} b_{2(s-n)+1} + b_{2n} b_{2(s+1-n)}) + b_0 b_{2(s+1)} \right] r^{2(s+1)} = 1 \qquad (A.13)$$

Setting $r = 0$ reveals that $b_0^2 = 1$. Furthermore, from repeatedly differentiating the equation with respect to r and then evaluating at $r = 0$ we find that

$$\sum_{n=0}^{s} (b_{2n+1} b_{2(s-n)+1} + b_{2n} b_{2(s+1-n)}) + b_0 b_{2s+1} = 0 \qquad (A.14)$$

for $s = 0, 1, 2, 3, \ldots$. This gives the second constraint on the coefficients.

Use of equation (A.4) results in

$$\nabla \cdot \left[\hat{1}_z \sum_{n=0}^{\infty} (a_{2n}' + M b_{2n}) r^{2n} + \hat{1}_r \sum_{n=0}^{\infty} (M b_{2n+1} + 2(n+1) a_{2(n+1)}) r^{2n+1} \right]$$

or $$\sum_{s=0}^{\infty} [4(s+1)^2 a_{2(s+1)} + 2(s+1) M b_{2s+1} + a_{2s}'' + M b_{2s}'] r^{2s} = 0 \quad (A.15)$$

This can hold true for all r if and only if

$$4(s+1)^2 a_{2(s+1)} + 2(s+1) M b_{2s+1} + a_{2s}'' + M b_{2s}' = 0 \qquad (A.16)$$

for s = 0, 1, 2, 3, ... This gives the final constraint on the coefficients.

In addition to equations (A.12), (A.14), and (a.16) we have the constraints that $b_0^2 = 1$ and $b_0\, a_0' > 0$. Since a_0' must be either positive or negative definite over the interval to insure saturation, without loss of generality we may take $a_0' > 0$ and $b_0 = +1$. The solution of equations (A.12), (A.14), and (A.16) is then:

$$s = 0, \qquad b_1 = -\frac{1}{2}\,\frac{a_0''}{a_0' + M} \tag{A.17.a}$$

$$a_2 = \frac{1}{2}\,b_1\,a_0' \tag{A.18.a}$$

$$b_2 = -\frac{1}{2}\,b_1^2 \tag{A.19.a}$$

$$s \geq 1,$$

$$b_{2s+1} = \{-\frac{1}{2(s+1)}\,(a_{2s}'' + M\,b_{2s}') \tag{A.17.b}$$

$$+ \sum_{k=1}^{s} [2(s-k+1)a_{2(s-k+1)}b_{2k} - a_{2k}'\,b_{2(s-k)+1}]\}/(a_0'+M)$$

$$a_{2(s+1)} = \{a_0'\,b_{2s+1} \tag{A.18.b}$$

$$- \sum_{k=1}^{s} [2(s-k+1)a_{2(s-k+1)}b_{2k} - a_{2k}'\,b_{2(s-k)+1}]\}/2(s+1)$$

$$b_{2(s+1)} = -\{\sum_{k=1}^{s} b_k\,b_{2s-k+2} + \frac{1}{2}\,b_{s+1}^2\} \tag{A.19.b}$$

Of course, when actually calculating the inner potential on the computer the a_i and b_i coefficients are not found explicitly, but approximated numerically.

III. Outer Field Determination

Now we must find an appropriate expansion for the Laplacian magnetic potential outside the cylinder. Laplace's equation in _spherical_ coordinates (ρ, θ, ϕ) is

$$\frac{\partial^2 \psi}{\partial \rho^2} + \frac{1}{\rho^2} \frac{\partial^2 \psi}{\partial \theta^2} + \frac{1}{\rho^2 \sin^2 \theta} \frac{\partial^2 \psi}{\partial \phi^2} + \frac{2}{\rho} \frac{\partial \psi}{\partial \rho} + \frac{\cot \theta}{\rho^2} \frac{\partial \psi}{\partial \theta} = 0 \qquad (A.20)$$

which has as a solution

$$\psi = (C_1 \rho^n + C_2 \rho^{-(n+1)}) (\cos m\phi) P_n^m(\cos \theta) \qquad (A.21)$$

If we assume no ϕ variation (i.e. m = 0) and transform this solution to _cylindrical coordinates_ (where of course it is still a valid solution) then we have that

$$\psi = [C_1 (r^2 + z^2)^{n/2} + C_2 (r^2 + z^2)^{-(n+1)/2}] P_n^0(\cos \theta)$$

Ignoring the second solution, we finally arrive at

$$\psi = C_1 (r^2 + z^2)^{n/2} P_n^0(\cos \theta) \qquad (A.22)$$

where $\tan \theta = \frac{r}{z}$ and $P_n^0(\cos \theta)$ is the associated Legendre function of degree n and order zero. If we then define

$$P_n^* \equiv (r^2 + z^2)^{n/2} P_n^0(\cos \theta) \qquad (A.23)$$

we can expand the outer potential $\hat{\psi}$ in terms of these polynomials as

$$-\hat{\psi} = \sum_{n=0} C_n P_n^*(r, z) \qquad (A.24)$$

For reference, the first five P_n^* functions are listed

below. Notice that since the P_n^* functions are non-singular for all z (i.e. have their sources at infinity), they must be used for regions outside the cylinder which contain the z-axis.

$$P_0^* = 1$$

$$P_1^* = z$$

$$P_2^* = z^2 - \frac{1}{2} r^2$$

$$P_3^* = z^3 - \frac{3}{2} z r^2$$

$$P_4^* = z^4 - 3 z^2 r^2 + \frac{3}{8} r^4$$

In addition, since in general the desired on axis field to be synthesized is a polynomial expression, and since the inner potential was expanded in a polynomial in r and z, it makes sense to expand the outer potential in the above polynomial expressions rather than the usual Bessel functions.

In regions outside the cylinder which do not include the z-axis (or where the z-axis is singular), solutions with a singularity at r = 0 may (or must) be added to equation (A.24). Instead of using the second solution to Laplace's equation in spherical coordinates which would yield a function singular only at a point, equation (A.22) is used along with Laplace's equation (ignoring ϕ variation) in cylindrical coordinates,

$$\frac{\partial^2 \psi}{\partial r^2} + \frac{1}{r} \frac{\partial \psi}{\partial r} + \frac{\partial^2 \psi}{\partial z^2} = 0 \qquad (A.25)$$

to obtain a second set of solutions singular on a line of the form

$$Q_n^*(r,z) = P_n^*(r,z) \cdot \ln r + N^*(r,z) \qquad (A.26)$$

where $N_n^* = z^n + \int \frac{1}{r} [2(z^n - P_n^*) - n(n-1) \cdot \int r N_{n-2}^* \, dr] \, dr$

$Q_n^*(r,z)$ is more usefully given by the recurrence formula

$$Q_n^* = \frac{2n-1}{n} z \, Q_{n-1}^* - \frac{n-1}{n}(z^2 + r^2) Q_{n-2}^* - \frac{2}{n}(P_n^* - z P_{n-1}^*) \qquad (A.27)$$

with $Q_0^* = (\ln r + 1)$. Therefore, in general the outer potential ψ may be expanded as

$$- \psi = C_0 + \sum_{n=1}^{N} C_n \, P_n^*(r,z) + \sum_{n=0}^{N-1} C_n' \, Q_n^*(r,z) \qquad (A.28)$$

where C_0 represents a reference potential and may be set to zero.

For reference, the first five Q_n^* functions are listed below. Notice that the Q_n^* functions, unlike the P_n^* functions, have their sources at both zero and infinity.

$$Q_1^* = \ln r + 1$$

$$Q_2^* = z \ln r + z$$

$$Q_3^* = z^2 \ln r - \frac{1}{2} r^2 \ln r + z^2$$

$$Q_4^* = z^3 \ln r - \frac{3}{2} z \, r^2 \ln r + z^3$$

$$Q_5^* = z^4 \ln r - 3 z^2 r^2 \ln r + \frac{3}{8} r^4 \ln r + z^4 - \frac{3}{16} r^4$$

Although the Q_n^* functions can be approximated by the P_n^* functions in many cases, this would require many terms in the expansion and P_n^* functions with large powers of z. Since in general it is better to expand in lower order polynomials, if possible Q_n^* functions should be included in the expansion of the outer potential. Expansions using the first five P_n^* functions and the first five Q_n^* functions yielded results consistent to better than an Oersted for the cases examined in this thesis.

IV. Boundary Conditions

This discussion is restricted to the case of a cylinder or disk, so it is beneficial to subdivide the outer region at the corners and carry out three separate expansions for $\hat{\psi}$. Those outer regions with $z < 0$ and $z > L$ cannot contain Q_n^* functions. The matching of $\psi = \hat{\psi}$ and $(1+\frac{M}{\nabla\psi})\frac{\partial\psi}{\partial n} = \frac{\partial\hat{\psi}}{\partial n}$ is carried out in a least squares sense. That is, if we assume the outer potential in a given region has been specified as

$$- \hat{\psi} = \sum_{j=1}^{N} C_j\, f_j(r,z) \qquad (A.28)$$

then we are trying to minimize the least square error defined as

$$E = \int_{\substack{\text{Boundary}\\ \text{Surface}}} [\psi - \sum_{j=1}^{N} C_j\, f_j(r,z)]^2\, dS \qquad (A.29.a)$$

An equivalent expression is

$$E = \langle\lambda_1^2 (\psi - \sum_{j=1}^{N} C_j\, f_j)^2\rangle + \langle\lambda_2^2 [(1+\frac{M}{\nabla\psi})\frac{\partial\psi}{\partial n} - \sum_{j=1}^{N} C_j\, \frac{\partial f_j}{\partial n}]^2\rangle \qquad (A.29.b)$$

where $\langle\ \rangle$ denotes averages over the boundary radius, and λ_1 and λ_2 weight, respectively, the relative importance of the tangential and normal components of the field subject to $\lambda_1^2 + \lambda_2^2 = 1$. Requiring $\frac{\partial E}{\partial C_i} = 0$ yields the set of equations

$$\sum_{j=1}^{N} [\langle\lambda_1^2\, f_i\, f_j\rangle + \langle\lambda_2^2\, \frac{\partial f_i}{\partial n}\, \frac{\partial f_j}{\partial n}\rangle]\, C_j$$
$$= \langle\lambda_1^2\, f_i\, \psi\rangle + \langle\lambda_2^2\, \frac{\partial f_i}{\partial n}\, (1 + \frac{M}{\nabla\psi})\, \frac{\partial\psi}{\partial n}\rangle \qquad (A.30)$$

for $i = 1, 2, 3, \ldots, N$. The solution of equation (A.30)

for the C_j coefficients yields an outer field that satisfies the boundary conditions.

The right circular cylindrical shape of the samples considered can be exploited to simplify the solution of equation (A.30). The radial match at $r = R$, and the end match at $z = L$ are considered separately.

IV.A. Radial Match

In order to obtain a good match with the outer field at the radius of the cylinder, the inner field is first approximated as

$$H_z(z,R^-) = \sum_{n=0}^{N-1} \alpha_n \left(\frac{z}{L}\right)^n \qquad (A.31)$$

and

$$[H_r(z,R^-) + M_r(z,R^-)] = \sum_{n=0}^{N-1} \beta_n \left(\frac{z}{L}\right)^n \qquad (A.32)$$

where N is an integer yielding tolerable error. This approximation is necessary since the inner field at the radius no longer has a polynomial form, while the outer field at the radius does have a polynomial form.

The α_n and β_n coefficients are found from a least squares fit using an inverse Hilbert matrix of order N. This arises from solving for the least squares coefficients such that the inner potential expansion,

$$f(x) = \sum_{k=1}^{N} A_k g_k(x) \qquad (A.33)$$

is approximated as a polynomial

$$f^O(x) = \sum_{k=1}^{N} A_k^O x^{k-1} \qquad (A.34)$$

The matrix least squares equation is of the form

$$
\begin{bmatrix}
\langle g_1^2 \rangle & \langle g_1\, g_2 \rangle & \langle g_1\, g_3 \rangle & \cdots \\
\langle g_2\, g_1 \rangle & \langle g_2^2 \rangle & \langle g_2\, g_3 \rangle & \cdots \\
\vdots & \vdots & \vdots & \\
\langle g_N\, g_1 \rangle & \langle g_N\, g_2 \rangle & \langle g_N\, g_3 \rangle & \cdots
\end{bmatrix}
\begin{bmatrix}
\langle A_1^o \rangle \\
\langle A_2^o \rangle \\
\vdots \\
\langle A_N^o \rangle
\end{bmatrix}
=
\begin{bmatrix}
\langle g_1 f \rangle \\
\langle g_2 f \rangle \\
\vdots \\
\langle g_N f \rangle
\end{bmatrix}
\tag{A.35}
$$

where $\qquad \langle g_i\, g_j \rangle = \dfrac{1}{L} \displaystyle\int_0^L g_i(x)\, g_j(x)\, dx$

and $\qquad \langle g_i\, f \rangle = \dfrac{1}{L} \displaystyle\int_0^L g_i(x)\, f(x)\, dx$

If the length of the cylinder is normalized to unity then

$$
\langle g_i\, g_j \rangle = \int_0^1 x^{i+j-2}\, dx = \frac{1}{i+j-1}
$$

Substituting into equation (A.35) yields

$$
\begin{bmatrix}
1 & \frac{1}{2} & \frac{1}{3} & \frac{1}{4} & \cdots \\
\frac{1}{2} & \frac{1}{3} & \frac{1}{4} & \frac{1}{5} & \cdots \\
\frac{1}{3} & \frac{1}{4} & \frac{1}{5} & \frac{1}{6} & \cdots \\
\vdots & \vdots & \vdots & \vdots &
\end{bmatrix}
\begin{bmatrix}
A_1^o \\
A_2^o \\
A_3^o \\
\vdots \\
A_N^o
\end{bmatrix}
=
\begin{bmatrix}
\int f(x)\, dx \\
\int x\, f(x)\, dx \\
\int x^2\, f(x)\, dx \\
\vdots \\
\int x^N\, f(x)\, dx
\end{bmatrix}
\tag{A.36}
$$

where the matrix multiplying the A_n^o coefficients is the Hilbert matrix of order N.

The solution to equation (A.36) is then

$$
\begin{bmatrix}
A_1^o \\
A_2^o \\
\vdots \\
A_N^o
\end{bmatrix}
=
H_N^{-1}
\begin{bmatrix}
\int f(x)\, dx \\
\int x\, f(x)\, dx \\
\vdots \\
\int x^N\, f(x)\, dx
\end{bmatrix}
\tag{A.37}
$$

where H_N^{-1} is the inverse Hilbert matrix of order N. However, the accuracy obtained with a computer solution to equation (A.37) can be deceptive. The Hilbert matrix is an ill-conditioned matrix, whose inverse rapidly overflows the capacity of a digital computer. Fortunately, from an engineering standpoint this inaccuracy is largely unimportant, changing the pole piece design only at distances far from the crystal sample. Since solutions to Maxwell's equations typically decay exponentially, varying the pole piece design far from the sample has little effect on the axial magnetic field. Therefore, the ill-conditioned property of the Hilbert matrix actually allows greater flexibility in the pole piece design and implementation.

In terms of α_n and β_n, the C_n and C_n' coefficients of equation (A.28) are found to satisfy

$$C_p = \frac{\alpha_{p-1}}{(p\,L^{p-1})} - (\ln R + 1)C_p'$$

$$- \sum_{k=1}^{N-p} R^{2k}\,A_{p+k,k} \cdot [C_{p+k} + (\ln R + \phi_k)C_{p+k}'] \qquad (A.37.a)$$

$$C_p' = \frac{R\,\beta_p}{L^p} - \sum_{k=1}^{N-p} R^{2k}\,A_{p+k,k} \cdot$$

$$\{2k[C_{p+k} + (\ln R + \phi_k)C_{p+k}'] + C_{p+k}'\} \qquad (A.37.b)$$

where $\qquad A_{n,k} = (-1)^k \dfrac{n!}{(n-k)!\,[(\frac{k}{2})!]^2\,2^k}$

and

$$\phi_k = \begin{cases} 1 & k=0 \\[2mm] 1 - (1+\frac{1}{2}+\frac{1}{3}+\ldots\frac{1}{N}) & k>0 \end{cases}$$

These equations are not general, but hold only for the special case of a right circular cylinder under discussion   Since by design $C_N' = 0$, equation (A.37.a) immediately gives C_N.

Alternating between equations (A.37.b) and (A.37.a) produces an unraveling that calculates in order C_N; C'_{N-1}, C'_{N-2}, C'_{N-3}, ...; C'_0. The value of C_0 is immaterial and may be set to zero.

IV.B. End Match

The outer potentials for $z < 0$ and $z > L$ can be found in a similar fashion. For the $z = 0$ end face, matching ψ and $H_z + M_z$ yields

$$C_n = \begin{cases} \dfrac{a_n(0)}{A_{n,n}} & n \text{ even} \\[2em] \dfrac{a_{n-1}(0) + M\, b_{n-1}(0)}{A_{n,n-1}} & n \text{ odd} \end{cases} \qquad (A.38)$$

where a_n and b_n satisfy equations (A.17), (A.18), and (A.19). Similar expressions result for the $z = L$ end face.

V. Design Example

To illustrate the use of the synthesis technique, it is helpful to work through a low order example by hand. We shall attempt the synthesis of a linear axial magnetic field of the form

$$H_z(0,z) = A + B \cdot z \qquad (A.39)$$

in a YIG cylinder of length L and radius R. For simplicity anisotropy will be ignored. Choosing

$$a_0 = A \cdot z + \frac{1}{2} B \cdot z^2 \qquad (A.40)$$

satisfies the requirement that

$$- \nabla \left(- \sum_{n=0}^{\infty} a_{2n}(z) \, r^{2n} \right) \Big|_{r=0} = A + B \cdot z \qquad (A.41)$$

Using equations (A.17), (A.18), and (A.19) we have that

$$b_1 = - \frac{1}{2} \frac{A}{B \cdot z + A + M} \qquad (A.42.a)$$

$$a_2 = - \frac{1}{4} \frac{A(A + B \cdot z)}{B \cdot z + A + M} \qquad (A.42.b)$$

$$b_2 = - \frac{1}{8} \frac{A^2}{(B \cdot z + A + M)^2} \qquad (A.42.c)$$

This allows the inner magnetic potential to be approximated as

$$\psi = - \left(A z + \frac{1}{2} B z^2 \right) + \frac{1}{4} \left(\frac{A(A + B z)}{B z + A + M} \right) r^2 \qquad (A.43)$$

The inner magnetic field is then given by

$$\overline{H}^i(r,z) = \left[A + B z - \frac{1}{4} M \frac{A B}{(B z + A + M)} r^2 \right] \hat{\imath}_z$$

$$+ \left[- \frac{1}{2} \frac{A B z + A^2}{B z + A + M} r \right] \hat{\imath}_r \qquad (A.44)$$

The magnetization is given by

$$\overline{M}(r,z) = M \left[1 - \frac{1}{8} \frac{A^2}{(B z + A + M)^2} r^2 \right] \hat{\imath}_z$$

$$+ M \left[- \frac{1}{4} \frac{A(A + B z)}{B z + A + M} r \right] \hat{\imath}_r \qquad (A.45)$$

Using equations (A.31) and (A.32) we then have that

$$H_z(R,z) \simeq \alpha_0 + \alpha_1 \left(\frac{z}{L} \right) + \alpha_2 \left(\frac{z}{L} \right)^2 \qquad (A.46.a)$$

$$\left[H_r(R,z) + M_r(R,z) \right] \simeq \beta_0 + \beta_1 \left(\frac{z}{L} \right) + \beta_2 \left(\frac{z}{L} \right)^2 \qquad (A.46.b)$$

For simplicity of calculation, we now assume that we are only concerned with matching tangential H, and we ignore the matching of normal B. This corresponds to setting $\lambda_1 = 1$ and $\lambda_2 = 0$ in equation (A.30). Expanding the outer potential as

$$- \psi = \sum_{n=0}^{2} C_n P_n^*(r,z) + C_0' Q_0^*(r,z) + C_1' Q_1^*(r,z) \qquad (A.47)$$

allows the least squares coefficients to be found. In terms of the α_n coefficients we find that:

$$C_0 = \alpha_0 - \alpha_2 \left(\frac{R}{L}\right)^2 \left(\frac{1}{2} + \ln R\right)$$

$$C_1 = \frac{1}{2} \frac{\alpha_1}{L}$$

$$C_2 = \frac{1}{3} \frac{\alpha_2}{L^2}$$

$$C_0' = \frac{1}{2} \left(\frac{\alpha_1}{L} - \alpha_1\right) R^2$$

$$C_1' = \alpha_2 \left(\frac{R}{L}\right)^2$$

More complete solutions can be obtained using the computer methods described in section IV. For computer solutions an expansion of the form of equation (A.28) is assumed. For the case of $A = B = 300$ in equation (A.39) we have as the coefficients:

End Match:

Coefficient	Value
C_1	− 2160.0000
C_2	− 21.6346
C_3	− 9.2571
C_4	− 0.2525
C_5	0.1111

Radial Match:

Coefficient	Value
c_1	$-$ 358.0249
c_2	$-$ 153.2998
c_3	0.3632
c_4	$-$ 0.0173
c_1'	$-$ 1.9934
c_2'	0.3182
c_3'	0.1384
c_4'	$-$ 0.0284

A plot of the equipotential contours implementing both the radial and end magnetic potential matches is shown in figure (A.1). Here, the magnetic potential end match at $z = L$ lies above that of the radial match at $z = L$, so the area enclosed by the two equipotentials would have to be negative. This is not physically realizable, and the end match at $z = L$ is not implemented. Since the magnetoelastic interactions occur near $z = 0$, this does not normally present any real problems.
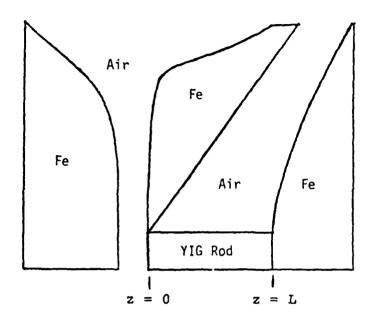
Figure (A.1) - Pole Piece Synthesis Example Showing
Both Radial And End Match

Synthesized Magnetostatic Modes and Waves Using Nonuniform Magnetic Bias Fields

Our progress on employing nonuniform dc field synthesis to magnetostatic modes and/or waves is described in the attached set of preprints and reprints of papers that were presented at the following conferences:

- -1980 Intermag Conference, Boston, Massachusetts, April 21 - 24, 1980

- -1980 International Conference on Ferrites, Kyoto, Japan, September 29 - October 2, 1980.

- -1980 Ultrasonics Symposium, Boston, Massachusetts, November 5 - 7, 1980

- -1980 Conference on Magnetism and Magnetic Materials, Dallas, Texas, November 11 - 14, 1980

For completeness, reprints are also included of our earlier work described at the 1977 Conference on Magnetism and Magnetic Materials and the 1978 Intermag, Florence, Italy.

NOVEL DEVICES BASED UPON FIELD GRADIENT
CONTROL OF MAGNETOSTATIC MODES AND WAVES

F. R. Morgenthaler
M.I.T.
Cambridge, Massachusetts

Abstract

We discuss the manner in which gradients in either the bias field magnitude, direction or both can be employed to synthesize magnetostatic wave dispersion characteristics or mode spectra. This is done to control pre-specified characteristics such as frequency, rf energy distribution, impedance, velocity of energy circulation and the threshold governing the onset of nonlinear effects due to parametrically-unstable spin waves.

Previous theoretical models are reviewed, extended, and utilized to predict the behavior of a new class of microwave resonators. In addition, we predict that frequency selective filter-limiters can be constructed with gradient-controlled limiting levels.

We also review experimental evidence of high-Q gradient-localized resonances in platelets and thin films of single crystal YIG. Included are recent observations of magnetostatic surface waves propagating in a thin film biased with a nonuniform in-plane field caused by movable permalloy strips.

NOVEL DEVICES BASED UPON FIELD GRADIENT
CONTROL OF MAGNETOSTATIC MODES AND WAVES*

F. R. MORGENTHALER

Department of Electrical Engineering and Computer Science
and the Research Laboratory of Electronics
Massachusetts Institute of Technology
Cambridge, Massachusetts, USA

Introduction

Our interest in controlling magnetostatic waves and modes by means of dc field gradients dates from the experimental observation of localized high-Q resonance in single crystal yttrium iron garnet (YIG) reported by Zeskind and Morgenthaler.[1]

Our interpretation of these resonances is that localized magnetic mode patterns are formed in which the resonant energies are guided or confined by regions of high dc field gradient within the crystal. By appropriately designing internal magnetic field profiles, one can create apparent "surfaces" or "tracks" of magnetic field discontinuity. Magnetic waves bound or guided by such gradients can be made to follow appropriate propagation paths with controlled group velcoity. If the mode amplitudes are very small at the edges and corners of the sample, the surface scattering (which one would expect to be enormous) is largely prevented. Consequently, the Q of the resonance governed primarily by the intrinsic linewidth of the bulk crystal together with normal circuit loading considerations.

In the first experiments such gradients arose naturally from the nonuniform shape demagnetizing fields; in subsequent work by Cooley[2] and Horowitz[3], we have created pre-specified gradients with shaped pole pieces designed by field synthesis techniques. A similar approach has recently been followed by Tsutsumi at al.[4]

We first review these early experiments and the theoretical treatment of

quasi-two-dimensional magnetostatic modes of single domain thin ferrite circular disks or annular rings, when the dc magnetic field is normal to the plane and varies radially.

We find solid theoretical justification for the 'track" concept and enumerate mode patterns for both gradient-modified boundary modes and gradient-dominated waves[5]. The important effects from rf fringing fields at the edge of the disk are also considered.

In the absence of a radial gradient, all of the modes of a solid disk have circularly-polarized rf h-fields with zero volume-divergence. These modes are stongly influenced by the magnetic pole distribution on the edge of the disk and the rf energy becomes progressively concentrated near the rim as the mode index increases.

When the field gradient is modest, the modes retain these general characteristics but develop non-zero values of $\vec{\nabla} \cdot \vec{h}$ throughout the volume which change both the state of polarization of the field and the distribution of rf energy; the latter can then predominate either in the central portion or near the edge of the disk. In addition, both the mode frequency and the velocity with which the mode energy circulates are found to be altered.

For increased gradient strength, the volume divergence of certain modes can change so dramatically that selective localization or expulsion of the energy occurs. The sense of polarization can also actually reverse. In certain cases, the volume divergence of the rf magnetization can become infinite (in the lossless exchangeless approximation) at a certain interior radius, r_x. The magnetic pole distribution at this "virtual-surface" thus resemble that of a true surface and can serve to guide and localize the mode.

These previously discussed "virtual-surface" modes, are reanalyzed in terms of the polarization factor of the rf magnetization. Analytic solutions of that factor are continuous through the "virtual-surface" and are given for

the two-dimensional modes associated with a special class of field profiles.

We next discuss the synthesis of modes with pre-specified characteristics, such as velocity of energy circulation and rf energy distribution. In addition, boundary conditions that have been imposed to make the mathematical analysis more tractable (namely placing the thin film or disk between perfectly conducting plates) are removed; the bias field is still normal to the plane but radial gradients although now generalized to arbitrary form must be only weak to moderate.

For mathematical convenience, we choose to model the thin film disk as a very oblate spheroid with semi-axes a and b. The thickness of the "disk" at its center is 2b and the radius is a where b<<a.

The modes analyzed are quasi-two-dimensional in that the rf magnetization is assumed to be without appreciable thickness variation; the fringing magnetic fields are, of course, three-dimensional because the spheriod is surrounded by free space.

The results can be utilized to predict the behavior of a new class of microwave resonator. In addition, we predict that frequency selective filter-limiters can be constructed with gradient-controlled limiting levels.

Finally, we consider the guiding of magnetostatic surface waves (MSSW) on films with an in-plane bias field that may be a function of those coordinates transverse to the propagation direction. In particular, the recent experimental observation[6] of MSSWs in a rectangular YIG film place between strips of permalloy and in the plane of the strips is reviewed.

Localized High-Q Resonance in Nonuniform DC Fields

While measuring the microwave coupling between two antennas closely spaced on the surface of a bulk single crystal YIG slab (with dc magnetic field applied perpendicular to the slab), Surprisingly, despite the very nonuniform demagnetizing field caused by the nonellipsoidal sample geometry, Zeskind[7] observed spatially

localized high-Q resonant modes. The convenient planar geometry along with the high-Q and magnetic tunability of these modes suggested the possibility of a totally integrated monolithic YIG filter.

The basic experimental configuration appears in Figure 1. Gold thin film antennas were photographically etched on the surface of the bottom alumina substrate. The 30 μm wide and 4.2 mm long antennas are separated by an 80 μm wide ground strip to improve electro-magnetic isolation. The bulk single crystal YIG slab cut along the (110) plane (shown in place on top of the antennas) is glued into a slot milled in the surface of the top alumina substrate. The top substrate and YIG, together, move with respect to the bottom substrate (antennas) thus allowing plots of spatially dependent microwave properties of the YIG. Both sides of the slab are polished to a surface finish of about one half micrometer. The dc magnetic field is applied perpendicular to the plane of the slab.

Figure 2 is a plot of microwave coupling between the two antennas as a function of frequency with antennas located along the center line of the slab and H_{dc} = 2300 Oe. The sharp resonance at 2.46 GHz is characterized by a half-power bandwidth of 1.8 MHz corresponding to a loaded-Q of approximately 1400. Insertion loss at resonance was initially on the order of 10dB but was subsequently reduced to under 2Db. The resonance is magnetically tunable over the range 2.2 to 3.0 GHz. No apparent power limiting was observed with input signals of up to +10 dBm.

In Figure 3 we plot microwave coupling as a function of antennas displacement along the surface of the YIG slab for fixed frequency (2.46 GHz) and fixed field (2300 Oe). A displacement of 0.0 mm corresponds to antennas located along the center line of the slab. It is evidently that spatially localized points of resonance exhibits symmetry about the middle of the crystal with maximum

response occurring at the midplane. Half-power spatial linewidths are approximately 60 nm.

Formulation of the Basic Two-Dimensional Equations

We consider a ferrimagnetic film disk magnetized to saturation in the z-direction by a dc field H; radial components are assumed negligible throughout the disk. Since we are interested in magnetic modes of frequency ω that have negligible electric field energy, the magnetostatic approximation is suitable and the rf magnetic field may be expressed as $h = -\nabla\psi$. Because the ferrite is assumed to be saturated by a cylindrically, symmetric field $H_z(r)$ and modes without z-variation are sought, we take the complex magnetostatic potential (with suppressed exp $[j\omega t]$ variation) to be of the form

$$\psi = \exp\left(|m| \int \frac{y(r)dr}{r} - jm\phi\right) \tag{1}$$

where m is a positive or negative integer and $y(r)$ determines the radial variation of the mode. The latter also describes the polarization of the rf $\bar{h}$-field

$$h_r/h_\phi = j \frac{|m|}{m} y(r) \tag{2}$$

The other field quantities follow from the Polder susceptibility tensor and the Maxwell Equation governing the curl of the electric $\bar{e}$-field.

They are

$$m_r = - \frac{|m|}{r} \left(\chi y - \kappa \frac{m}{|m|}\right)\psi \tag{3a}$$

$$m_\phi = j \frac{m}{r} \left(\chi - \kappa \frac{m}{|m|} y\right)\psi \tag{3b}$$

and

$$e_z = -\omega\mu_0 |m| y^0(r)\psi r \tag{4}$$

where

$$y^0 = (1+\chi) y - \kappa \frac{m}{|m|}$$

Here $\chi = Z/(Z^2-\Omega^2)$, $\kappa = -\Omega/(Z^2-\Omega^2)$ with $Z(r) = H_z(r)/M$ and $\Omega = \omega/\omega_M$. The latter are, respectively, field and frequency normalized to the saturation magnetization M; $\omega_M = -\gamma\mu_0 M$ where γ (negative) is the gyromagnetic ratio. It is also convenient to take $\Omega > 0$ and define $\sigma = \Omega m/|m|$.

The polarization factors of the rf magnetization and rf flux were ignored in our previous work but have been found to be very useful quantities. Consequently we define

$$m_r/m_\phi = j \frac{m}{|m|} p(r) \quad \text{and} \quad b_r/b_y = j \frac{m}{|m|} p^0(r) \qquad (5a), (5b)$$

where from Eqs. (3a, 3b) and (4)

$$p = \frac{Zy+\sigma}{Z+\sigma y} \quad \frac{Zy^0+\sigma}{Z+1+\sigma y^0} \quad \text{and} \quad p^0 = \frac{(Z+1)p-\sigma}{Z+1-\sigma p} \qquad (6a), (6b)$$

The wave impendances are defined by

$$\eta_r = \frac{e_z}{h_\phi} = j \frac{m}{|m|} \omega\mu_0 r y^0(r) \qquad (7a)$$

$$\eta_\phi = \frac{e_z}{h_r} = \frac{m}{|m|} \omega\mu_0 r \frac{y^0(r)}{y(r)} \qquad (7b)$$

The former quantity must be a continuous function of r.

The magnetostatic equations ($\nabla\times\bar{h}=0$, $\nabla\cdot\bar{h}=-\nabla\cdot\bar{m}$) require that

$$\frac{dy^0}{dr} = \frac{|m|}{r} (1+\chi(r))(1-y^2) \qquad (8a)$$

or equivalently from (6).

$$\frac{dy}{dr} = \frac{m}{r} (1-y^2) + \frac{(Z^2+\sigma^2)y+2Z\sigma}{(Z^2+Z-\sigma^2)(Z^2-\sigma^2)} \frac{dZ}{dr} \qquad (8b)$$

and

$$\frac{dp}{dr} = \frac{m}{r} (1-p^2) + \frac{\sigma(p^2-1)+p}{Z^2+Z-\sigma^2} \frac{dZ}{dr} \tag{8c}$$

In regions where $dZ/dr=0$, y and p are each of the form $(r^{2|m|}-C)/r^{2|m|}+C)$ where C is a constant; in air regions $y^0 = y$.

In regions where dZ/dr is very large, the first term on the RHS may be neglected and Eq. (8c) integrated directly.

Boundary Conditions at the Edge of the Parallel Plate Region

As a concrete example, consider a thin ferrite disk of thickness d and radius R placed between perfectly conducting circular plates that extend to the radius R_0. The cylindrical surface $r=R_0$ is assumed either conducting for $|z| < d/2$, (a) or for $|z| > d/2$, (b).

For (a), $n_r=0$ at the radius $r=R_0$ and from Eq. (7a), $y^0(R_0)=0$.

For (b) a reasonable approximation valid when $d/R_0 << 1$ is

$$[y^0(m,R_0)]^{-1} \simeq - \frac{|m|d}{\pi R_0} \ln \left(\frac{\frac{2\pi R_0}{d}+1+2\sqrt{\left(\frac{\pi R_0}{d}\right)^2 + \frac{\pi R_0}{d}+m^2}}{2|m|+1} \right) \tag{9}$$

Solutions When $Z(r) = A \cdot (A+Br^{2n})/(A_\infty+Br^{2n})$

In order to develop insight into the character of the modes that result when $Z(r)$ forms a potential well, we consider this general class of profile for which Eq. (8c) reduces to

$$\frac{dp}{dZ} \simeq \frac{|m|}{2n} \frac{(A_\infty-A_0)}{(Z-A_0)(A_\infty-Z)} + \frac{\sigma(p-\frac{Z_x}{\sigma})(p+\frac{\sigma}{Z_x})}{(Z-Z_x)(Z+Z_x+1)} \tag{10}$$

Once a solution of Eq. 12 is found, it can be applied to profiles with any desired value of B.

When $A_\infty \to \infty$, this family reduces to $Z=A+Br^{2n}$ analyzed previously.[5]

Sketches of possible rf magnetic field contours are given in Fig. 3 of Ref. 5.

For weak gradients, $|BR^{2n}| \ll 1$ and non-"virtual-surface" modes exist for $m>0$ when

$$\Omega_m \simeq A + \frac{m}{n+m} BR^{2n} + \frac{1}{2} [1 + \frac{1+y^0(R_0)}{1-y^0(R_0)} (\frac{R}{R_0})^{2m}] \qquad (11)$$

Solutions for p(Z)

A series solution for $p(Z)$ valid in the vicinity of $Z=Z_0$ can be obtained by assuming

$$p(Z) = \sum_{k=0} C_k (Z-Z_0)^K \qquad (12)$$

and using Eq. (13) to find the recurrence relationship among the various coefficients, C_K, given that $C_0 = p(Z_0)$.

The special cases $Z_0=A_0$ or A_∞ must be handled separately and the series representation generally fails when $Z(r_x) = Z_x = (\sqrt{1+4\sigma^2}-1)/2$ because at a "virtual-surface" $y(r_x)$ is singular and the radius of convergence for the power series goes to zero.

On the other hand, from Eq. (10) it follows that $p(Z_x) = Z_x/\sigma$ (or possibly $-\sigma/Z_x$) and the finite value allows one to integrate $p(Z)$ through the virtual surface.

The result of a detailed analysis reveals that with $u = (Z-Z_x)/(Z_x-A_0)$

$$p(u) = \frac{Z_x}{\sigma} - \frac{u}{w} \frac{dW}{du} / [\frac{\sigma}{Z+Z_x+1} - \frac{|m|}{2n} \frac{(A_\infty-A_0)(Z-Z_x)}{(Z-A_0)(A_\infty-Z)}] \qquad (13)$$

where for $A_\infty \to \infty$, $W(u)$ satisfies the following form of linear equation with nonconstant coefficients:

$$(1+ \sum_{K=1}^{5} R_K u^K) \frac{d^2 W}{du^2} + (\sum_{K=1}^{5} P_K u^K) \frac{1}{u} \frac{dW}{du} + (\sum_{K=1}^{5} Q_K u^K) \frac{W}{u^2} = 0 \qquad (14)$$

using the method of Frobenius, the solution of Eq. (14) is of the form

$$W \sim (C_h + \ln|u|) \sum_{K=1}^{\infty} b_K u^K + \sum_{k=1}^{\infty} d_K u^K \qquad (15)$$

where b_K and d_K are constants related to the R_K, P_K, Q_K coefficients and C_h is an integration constant used to match between the power series expansions of the form of Eq. (12) used on either side of Z_x. The solution is valid when $|u| < 1$ but it is also possible to expand W in powers of u^{-1} and hence obtain the asymptotic behavior for large Z.

It should be noted that exchange effects[9,10] at the "virtual-surface" are ignored in this model.

The properties of an $m=1$ "virtual-surface" mode are illustrated with the profile $Z = .3 + 1.095(r/R)^4$ for which, if y $(m=1,R) = -1$, such a mode occurs when $\Omega = .695$. The associated $\overline{m}$-field, $\overline{h}$-field and $\overline{b}$-field loci are plotted, respectively, in Figure (4a,b,c) with the "virtual-surface" radius $(r_x = .385R)$ shown by the dotted circle. Notice the reversed direction of $\overline{m}$ leading to "surface" magnetic poles near $r-r_x$. Notice too, that $p(r/R \sim .59) = 0$. Along with changes in Ω, larger values of BR^4 will cause r_x to shrink; smaller values to expand.

Synthesized Magnetostatic Resonances in a Nonuniformly Biased Thin Disk Without Conducting Boundaries

If the conducting plates bounding the ferrite are either separated or removed entirely, the rf field inside the disk will fringe. Then field variations with respect to z may be important even for the quasi-two-dimensional modes, as the outer and inner fields interact along the entire disk surface. If the ferrite is comparatively thick, z-variations in both $\overline{H}_{dc}$, and hence $\overline{\overline{\chi}}$, will occur and mode localization effects due to these vertical gradients can be expected.

When the disk is thin, the gradients weak to moderate, so that the modes in question do not have "virtual-surfaces, another form of analysis is convenient. We here review that alternate approach.[11]

The complex magnetostatic potential within the ferrite is approximately given by $\psi = R(r)e^{-jm\phi}$ where r and ϕ are cylindrical coordinates the factor $e^{j\omega t}$ is again suppressed and m is a positive mode integer.

We again choose to work with dc fields and frequencies that are normalized to the saturation magnetization M of the material. However, we now generalize the dc bias to be

$$H_z/M = Z(r) = A + \sum_{n=1}^{N} B_n r^{2n} \tag{16}$$

In terms of circularly-polarized small-signal magnetization vectors

$$\bar{m}^{\pm} = m_{\pm}(r)(\bar{i}_r \mp j\bar{i}_\phi) e^{jm\phi} \tag{17a,b}$$

and their associated scalar susceptibilities $x^{\pm} - 1/Z \mp \Omega$ the equation $\nabla \cdot \bar{b} = 0$ and $\nabla \times \bar{h} = 0$ become

$$\nabla \cdot [(1+Z-\Omega)\bar{m}^{+} + (1+Z+\Omega)\bar{m}^{-}] = 0 \tag{18a}$$

$$\nabla \times [(Z-\Omega)\bar{m}^{+} + (Z+\Omega)\bar{m}^{-}] = 0 \tag{18b}$$

Because the field gradients are assumed to be modest, the mode frequencies for low order m will satisfy $|Z-\Omega| \ll 1$ and $\bar{m}^{-}$ will be small. Therefore $\bar{m}^{+}$ is expected to be approximately Laplacian in character and, in fact, detailed perturbation analysis reveals that when $|m_-/m_+| \ll 1$ the associated potential inside the spheroid is

$$\psi^i \simeq m_0 \left[\frac{\Omega-A}{m} - \sum_{n=1}^{N} \frac{B_n}{n+m} r^{2n}\right] \left(\frac{r}{a}\right)^m e^{-jm\phi} \tag{19}$$

whereas outside it, the potential satisfies Laplace's Equation. Both ψ and the the normal component of $\bar{b}$ are continuous at the boundary.

The application of the boundary condition $\psi^i = \psi^0$ over the boundary surface is straight-forward, but calculation of $b_\zeta^i = b_\zeta^0$ involves evaluation of $\partial\psi^i/\partial z \neq 0$.

Fortunately, there is an alternate way to proceed that circumvents this difficulty; we calculate the dominant contribution to the far field potential from our knowledge of the form of $\overline{m}$ inside the spheroid and match it to the asymptotic value of ψ^0. The net result is that a mode exists whenever

$$\Omega_m = A + N(m) + \frac{1}{1+\frac{3/2}{m}} (B_1 a^2 + \frac{1}{1+\frac{3/2}{m+1}} (B_2 a^4 + \frac{1}{1+\frac{3/2}{m+2}} (B_3 a^6 + \ldots)))..) \qquad (20)$$

where

$$N(m) = \frac{b}{a} \frac{(\frac{a}{c})^{m+1} F_m^{(m)}(\frac{a}{c})}{(m-1)! 2^m} \qquad (21)$$

and

$$F_m(m)(\zeta) = (2m-1)!!\zeta^m \sin^{-1}(\frac{1}{\zeta}) - \frac{\sqrt{\zeta^2-1}}{m} [(2m-2)!! + (2m-1)(2m-4)!!\zeta^2$$
$$+ (2m-1)(2m-3)(2m-6)!!\zeta^4 + \ldots + (2m-1)!!\zeta^{2m-2}] \qquad (22)$$

where $n!! = n(n-2)(n-4)\ldots$

which both $\nabla\cdot\overline{m}=0$ and $b/a \to 0$.

In such cases, retaining terms in $\overline{h}$ that are first-order in k_0^2, leads to a modification of the normalized frequencies Ω_m that can be incorporated by letting

$$N(m) \to N(m) - \frac{(k_0 a)^2}{2m(m+1)}$$

As expected, this correction is largest for $m=1$.

Synthesized Dispersion Relations

If it is desired to create a spectrum with the resonance frequencies separated by pre-specified amounts or if one wishes to control the velocity of energy circulation v_ϕ^E of individual modes, the independent constants B_n can be adjusted and the required field $H_z(r)$ synthesized. In the former case, Eq. (27) is used alone whereas in the latter, the relation $v_\phi^E(m) = r\omega_\phi(m)/m$ (analogous to the group velocity for a plane wave) is also employed.

It is useful to realize that v_ϕ^E can be forced to be independent of m over some range of m. This also suggests that magnetostatic plane wave propagation can be made precisely nondispersive over a predetermined bandwidth.

Control of v_ϕ^E not only affects the group delay of signals propagating through the mode but also the total energy, E, of the mode in terms of the signal power P_ϕ. The governing relationship is $E = 2\pi r P_\phi/v_\phi^E$. The important point to be realized is that the normally slow energy circulation that occurs when $B_n=0$ can either be speeded up or slowed down. In the latter event, the direction of net power flow can even be reversed. Near the balance point where $v_\phi^E=0$, E becomes very large, for a fixed value of P_ϕ. Because nonlinear behavior, due to parametric spin wave instabilities[13], occurs when the energy density of the mode reaches a critical value, it follows that the threshold power of limiting level should be gradient controllable.

Consider two examples in which both $k_0 a$ and $N(m)$ are negligible.

In the first, we require that B_1 and B_2 force $\partial\Omega/\partial m=0$ for $m=1$ and .01 for $m=2$. The required values are

$$B_1 a^2 = -.267 \qquad B_2 a^4 = .344$$

In the second, we require that B_1, B_2 and B_3 force $\partial\Omega/\partial m=.01$ for $m=1$ and 0 for $m=2$ and $m=3$.

The required values are

$$B_1 a^2 = .477 \qquad B_2 a^4 = -1.121 \qquad B_3 a^6 = .739$$

In Figures (5a,b) and 6a,b) the values of $\Omega(m)$ and $\partial\Omega/\partial m$ are plotted vs. m for the two cases; in Figures (5c) and (6c) the required field profiles of Z-A are plotted vs. r/a.

Field Synthesis

In order to normally magnetize a very thin disk of magnetization M so as to produce within it the normalized field $H_z-M = A+Br^{2n}$, we first create the free space dc magnetic potential.

$$\hat{\psi} = C_0 + (A+1)Mz + (-1)^n \frac{n!4^n}{(2n+1)} BMP^*_{2n+1}(r,z) \tag{23}$$

where $P^*_n(r,z) = (z^2+r^2)^{n/2} P^0_n(\cos\theta)$, $\tan\theta = r/z$ and P^0_n is the associated Legendre function of degree n and order zero. These polynomial satisfy the recurrence formula

$$P^*_n = \frac{2n-1}{n} z P^*_{n-1} - \frac{n-1}{n} (z^2+r^2)P^*_{n-2} \tag{24}$$

with $P^*_0=1$.

The field associated with $\hat{\psi}$ can be generated utilizing high permeability pole-pieces designed to follow suitable equipotentials for Eq. 23.

If the thin disk is located at the plane z=0, and centered at r=0, the boundary conditions will be matched (neglecting fringing at the rim) and the required Z(r) generated inside the disk. Notice that through the use of super-position, any field of the form $H_z(r) = \sum_{n=0}^{} \alpha_n r^{2n}$ can be synthesized.[14]

Magnetostatic Modes and Waves in Films with Nonuniform In-Plane Bias

The analysis of three-dimensional modes in films with nonuniform in-plane bias by means of a coupled integral equation approach will be presented at the 1980 Conference on Magnetism and Magnetic Materials.[15]

The prospect of guiding magnetostatic waves is of considerable interest because of possible device applications.[16] Such guided waves might be used to increase the delay time realizable on a given size sample by meadering the path,

or to make a resonator by guiding the waves along a closed loop. In addition, controlling the coupling between adjacent waveguides could make possible signal routing devices such as directional couplers.

Guiding such a wave is complicated by the fact that MSSW propagation is only possible in one direction on a given surface when the applied in-plane bias field is uniform;[17] turns of 90° would normally require conversion to backward volume waves.

It should be possible to overcome this difficulty by employing gradients that arise from a change in the direction of the bias field. As an example, consider a YIG film that is covered with permalloy containing a slot of controlled width. If the permalloy is at a different magnetostatic potential on either side of the slot, the dc magnetic field will be parallel to the film in the region underneath the slot but normal to the film surface in those portions directly underneath the permalloy.

The in-plane fields permit magnetostatic surface wave propagation; the normal fields do not . Therefore the surface wave energy should be localized under the air-filled slot rather than under the conducting permalloy; eddy current dissipation is thereby minimized.

Notice also, that if the entire bias field is normally directed, the surface wave disappears completely. Taken together, these factors should allow novel control of the surface wave channel.

We here review Stancil's experimental observations[6] of MSSW propagation in a rectangular YIG film centered in the slot between strips of high permeability metal foil. The results indicate that surface waves can propagate in such a geometry but with modified dispersion characteristics, as expected.

The geometry of the experiment to be described is shown in Fig. (7). The sample is a 4.5 micron thick film of YIG approximately .28 cm wide and 1.09 cm long. The fine wire antennas are 50 microns wide and separated by 1 cm.

The results of the experiments can be summarized as follows:

1. As the gradient is increased, by decreasing the space d between the permalloy strips, a series of discrete modes appears on the low frequency side of the MSSW band. This behavior is illustrated in Figure 8.

2. Reversing the polarity of the bias field results in slightly reducing coupling to both the continuous and discrete modes implying that these modes have a nonreciprocal surface localization similar to conventional MSSW's.

3. Although the discrete modes show evidence of nonreciprocal surface localization, they appear at frequencies below the bottom of the surface wave band at the center of the film as calculated from the corrected fields at $y=x=0$. The arrows shown in Fig. 8 indicate the bottom of the MSSW band for each d as calculated in this way.

4. The slope of the phase was used to calculate approximate group velocities. The discrete modes propagate several times faster than the normal MSSW modes.

Acknowledgement

References

1. D. A. Zeskind and F. R. Morgenthaler, "Localized High-Q Ferromagnetic Resonance in Nonuniform Magnetic Fields," IEEE Trans. on Mag., Vol. MAG-13, No. 5, September (1977).
2. J. J. Cooley, "Magnetostatic Modes Bound by DC H-Field Gradients," S.M. Thesis, Dept. of Electrical Engineering and Computer Science, M.I.T., September (1977).
3. P. N. Horowitz, "Variable Speed Magnetostatic Modes in Uniform or Nonuniform DC H-Fields," S. M. Thesis, Dept. of Electrical Engineering and Computer Science, M.I.T., February (1979).
4. M. Tsutsumi, et al, "The Effect of an Inhomogeneous Bias Field on the Delay Characteristics of Magnetostatic Forward Volume Waves," Applied Physics Letters, Vol. 35, July (1979), p. 204.
5. F. R. Morgenthaler, "Bound Magnetostatic Waves Controlled by Field Gradients in YIG Single Crystals and Epitaxial Films," IEEE Trans. on Mag., Vol. MAG-14, September (1979), pp. 806-810.
6. D. D. Stancil and F. R. Morgenthaler, "Magnetostatic Surface Modes in a Thin Film with Nonuniform In-plane Fields," to be published in IEEE Trans in Mag. Conference Proceedings, September (1980).
7. D. A. Zeskind, "Localized Ferromagnetic Resonance in Nonuniform Magnetic Fields," S. M. thesis, Dept. of Electrical Engineering and Computer Science, M.I.T., February (1976).
8. F. R. Morgenthaler, Two-dimensional Magnetostatic Resonances in a Thin Film Disk Containing a Magnetic Bubble," presented at the 1978 Conference on Magnetism and Magnetic Materials, Cleveland, Ohio, November 14-17, (1978).
9. D. D. Stancil, "Magnetostatic Waves in Nonuniform Bias Fields Including Exchange Effects, to be published in IEEE Trans. on Mag. Conference Proc., September (1980).
10. F. R. Morgenthaler, "Synthesized Magnetostatic Resonances in a Nonuniformly Biased Thin Disk Without Conducting Boundaries," to be published in IEEE Trans. on Mag. Conference Proc., September (1980).
11. L. R. Walker, "Resonant Modes of Ferromagnetic Spheroids," J. Appl. Phys., Vol. 29, (1958), p. 318.
12. H. Suhl, "The Nonlinear Behavior of Ferrites at High Microwave Signal Levels," Proc. IRE, Vol. 44, (1956), p. 1270.
13. F. R. Morgenthaler and A. Platzker, "Magnetic Field Synthesis Procedures for Magnetostatic and Magnetoelastic Devices," Proc. of the 1978 International Symposium on Circuits and Systems, N.Y.C., May 17-19, (1978).
14. F. R. Morgenthaler, "Magnetostatic Surface Modes in Nonuniform Thin Films With In-Plane Bias Fields," submitted to the 26th Annual Conference on Magnetism and Magnetic Materials, Dallas, Texas, Nov. 11-14, (1980).
15. J. D. Adam and H. H. Collins, "Microwave Magnetostatic Delay Devices Based on Epitaxial Yttrium Iron Garnet," Proc. IEEE, Vol. 64, No. 5, May (1976), p. 794.
16. R. W. Damon and J. Eshbach, "Magnetostatic Modes of a Ferromagnetic Slab," J. Phys. Chem. Solids, Vol. 19, (1961), p. 308.

Figure Captions

Figure 1. Experimental configuration (a) partially exploded view
                                           (b) cross-sectional view

Figure 2. Microwave coupling between two antennas as a function of frequency.
           Antennas located along the crystal center line with H_{dc} = 2300 Oe.

Figure 3. Coupling between antennas as a function of crystal position with
           frequency = 2.46 GHz and H_{dc} = 2300 Oe.

Figure 4. Locus of field lines for the "virtual surface" mode $\Omega(m=1)$ = .655
           when Z = .3+1.095 $(r/R)^4$. The rf $\overline{m}$-field is shown in (a) the
           $\overline{h}$-field in (b) and the $\overline{b}$-field in (c). All patterns rotate at the
           normalized frequency Ω. The "virtual-surface" (shown dotted) occurs
           at r_x/R = .385 .

Figure 5. The normalized mode frequency (a) and pre-specified energy frequency
           (b) both plotted vs. mode number together with the required field
           profile (c) plotted vs. radius.

Figure 6. The normalized mode frequency (a) and pre-specified energy frequency
           (b) both plotted vs. mode number together with the required field
           profile (c) plotted vs. radius.

Figure 7. Basic experimental configuration.

Figure 8. MSSW transmission spectra as a function of the spacing between the
           permalloy strips. The fine structure near the high frequency end
           is due to interference with the EM feedthrough.
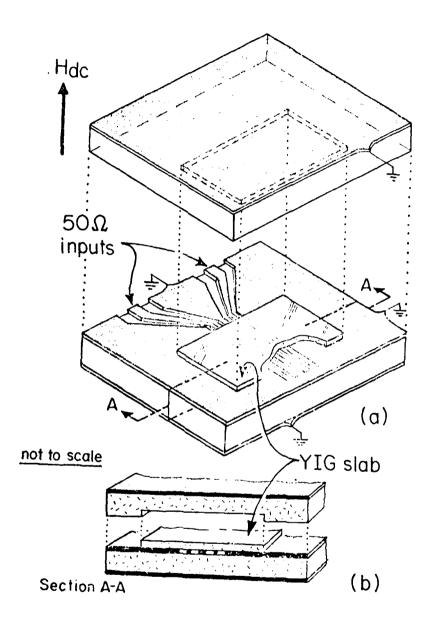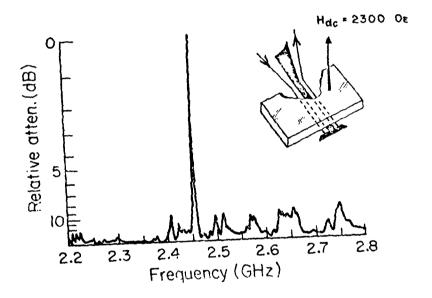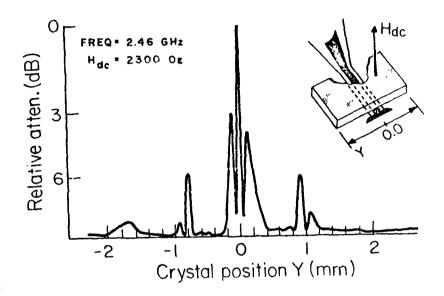
Hdc

50Ω inputs

A

A

(a)

not to scale

YIG slab

Section A-A

(b)

Figure 1

Figure 2

Figure 3

(a) $\overline{m}$-field locus

(b) $\overline{h}$-field locus

(c) $\overline{b}$-field locus

Figure 4

Figure 5

a.

b.
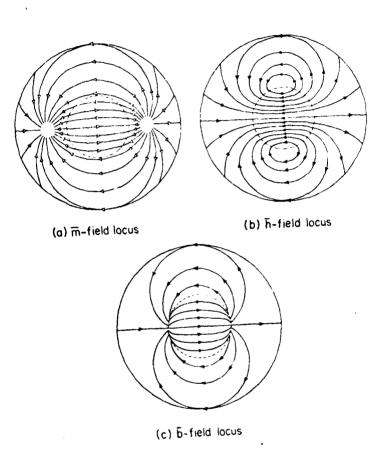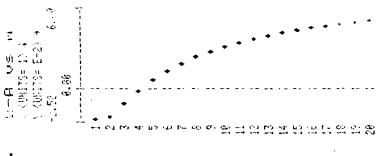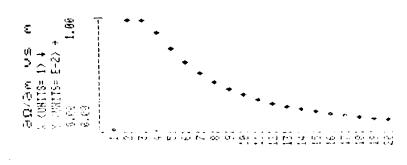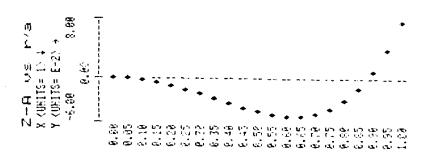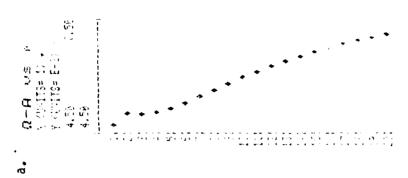
Figure 7

Figure 8

Effects of Exchange in Nonuniform Fields

I. Introduction

                                        In this Chapter we will
discuss how nonuniform fields along with the exchange interaction can
localize volume wave excitations in a normally magnetized thin film between
conducting plates. Although the presence of the conducting plates is
undesirable from an experimental point of view, a significant mathematical
simplification results which in some cases allows closed form solutions to
be obtained. These solutions give insight into the role of exchange in the
localization of magnetostatic waves with nonuniform fields.

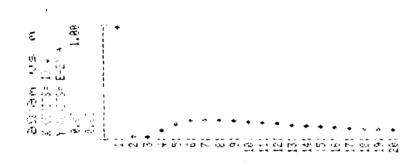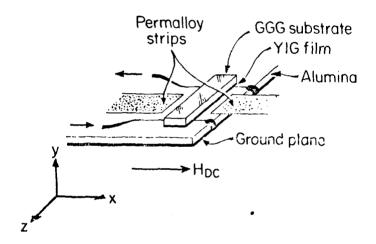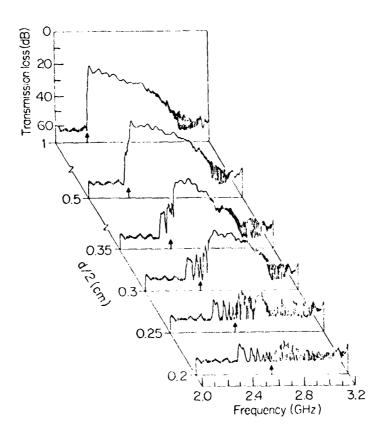The simplest field nonuniformity is, of course, that of a
one-dimensional linear profile. Such a profile has been used to synthesize
linear delay-vs.-frequency characteristics in single crystal YIG rods (29).
In this Chapter we discuss the possibility of a similar application of
linear profiles in thin ferrite films. Also, since an arbitrary
one-dimensional profile can always be linearized in a small region about a
point of interest, the understanding gained from the study of a linear
profile has very wide applications.

A profile which could be used in signal routing applications is the
one-dimensional quadratic profile. We will show that a magnetostatic wave
can be confined by such a profile and made to propagate along the direction

transverse to the gradient, much as water is guided by a trough.

Third, we will show that a magnetostatic mode can be totally confined by a two-dimensional quadratic field profile. Such a confined mode, or resonance, could form the basis of a tunable microwave filter.

As a bonus, the calculations predict the existence of a continuum of spin wave modes at frequencies above the top of the volume wave manifold confirming an earlier theory described by Eshbach (30) based on a quasi-uniform plane wave approach.

Although we have motivated the study of these particular profiles using possible device applications, we should point out that the primary value in the solutions to be described is in understanding the role of exchange in nonuniform fields; it is doubtful that modes dominated by exchange will be of great practical interest due to high propagation losses. It seems certain, however, that analogous mode confinement will result if the wave dispersion is dominated instead by the dipolar interaction. This would be the case in the more practical geometry of a ferrite slab without conducting plates.

Although the present study was begun because of questions raised by the virtual surface theory (12,15), our geometry differs from that of Morgenthaler's in one important respect. The properties of the virtual surface modes depend crucially on the boundary conditions at the edges of a finite width or diameter thin film. In our geometry the film is of infinite extent in the plane; hence edge effects are completely neglected. It is clear that the modes obtained by the two methods will not in general

be in one-to-one correspondence. However, it will in some cases be possible to draw connections between the two theories, and these will be stressed where appropriate.

II. Expansion in Normal Modes of the Magnetization

It is well known that the linearized torque equation reduces to a Schrodinger equation when dipolar interactions are neglected (31). When solutions to this are known, it is sometimes possible to construct a set of basis vector-functions from which solutions to Maxwell's equations in the magnetostatic limit can be constructed. We construct a set of basis vector-functions in a manner similar to that used by Vendik, et al. (17,18).

The geometry considered is that of a thin sheet of ferrite between perfectly conducting plates (Figure 2.1). The ferrite is assumed to be unbounded in the x and y directions. The material is magnetized by an H field whose only component is in the z direction but which has some arbitrary variation along x and y. This is strictly not allowed by the requirement $\nabla \times H = 0$, but can be a reasonable approximation if the thickness is sufficiently small. Although the applied field is nonuniform, the material is assumed to be saturated everywhere. The presence of the conducting plates allows us to consider fields which depend only on x and y. All fields depend on time through the factor $\exp(-i\omega t)$.

As shown in Appendix A, the linearized equation of motion for the magnetization can be written

$$\overline{h} = \overset{=}{\Lambda}_{op} \cdot \overline{m} \tag{2.1}$$
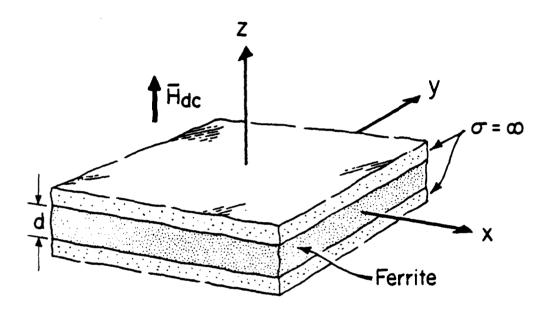
Figure 2.1. Geometry for exchange calculations

where

$$\bar{\bar{A}}_{op} = \begin{bmatrix} Z - \lambda_{ex}\nabla_t^2 & i\Omega \\ -i\Omega & Z - \lambda_{ex}\nabla_t^2 \end{bmatrix} ,$$

$$\nabla_t^2 = \frac{\partial^2}{\partial x^2} + \frac{\partial^2}{\partial y^2} ,$$

$$\Omega \equiv \frac{\omega}{-\gamma\mu_o M_s} , \qquad Z = H_o^{eff}/ M_s ,$$

$\bar{h}$ is the rf magnetic field, H_o^{eff} is the total effective dc magnetic field, M_s is the saturation magnetization, λ_{ex} is a phenomenological exchange constant, and γ is the gyromagnetic ratio (negative).

Suppose that the eigenvectors and eigenvalues of $\bar{\bar{A}}_{op}$ exist and are known; i.e., assume the equation

$$\bar{\bar{A}}_{op} \cdot \bar{S}_\ell = a_\ell \bar{S}_\ell \tag{2.2}$$

has been solved. Since $\bar{\bar{A}}_{op}$ is Hermitian, the eigenvalues (a_ℓ) will be real.

Let us assume that the magnetization can be expanded in terms of these eigenvectors (the success—or failure—of the method will determine the validity of this assumption). The magnetization can then be written

$$\bar{m} = \sum_\ell c_\ell \bar{S}_\ell . \tag{2.3}$$

The magnetic field can now be obtained easily from $\overline{m}$ in this representation:

$$\overline{h} = \sum_{\ell} c_\ell a_\ell \overline{S}_\ell . \tag{2.4}$$

We can now substitute (2.4) into Maxwell's equations in the magnetostatic limit and look for the coefficients (c_ℓ) and eigenvalues (a_ℓ) such that the equations are satisfied.

Having outlined our approach, let us return to the eigenvalue problem (2.2).

Note that $\overline{\overline{A}}_{op}$ can be written as the sum of a scalar operator and a matrix operator

$$\overline{\overline{A}}_{op} = (Z - \lambda_{ex}\nabla_t^2)\overline{\overline{I}} + \Omega \begin{bmatrix} 0 & i \\ -i & 0 \end{bmatrix} \tag{2.5a}$$

$$\overline{\overline{A}}_{op} = R_{op} \overline{\overline{I}} + \Omega \overline{\overline{P}}_{op} \tag{2.5b}$$

where R_{op} acts on the space of arbitrary functions of x and y and $\overline{\overline{P}}_{op}$ acts on the space of two-dimensional complex vectors. As a trial form for the eigenvectors, let us consider

$$\overline{S}_\ell = f(x,y)\overline{p} \tag{2.6}$$

where $f(x,y)$ is an eigenfunction in the space of R_{op} given by

$$R_{op} f(x,y) = \rho f(x,y) \tag{2.7}$$

and $\overline{p}$ is an eigenvector in the space of $\overline{\overline{P}}_{op}$ given by

$$\overset{\bullet}{P}_{op} \cdot \overline{p} = - \sigma \overline{p} . \tag{2.8}$$

(The reason for the minus sign will be discussed shortly.) The eigenvalue
equation (2.2) becomes

$$\overset{\bullet}{A}_{op} \cdot \overline{S}_\ell = (R_{op} \overset{\bullet}{I} + \Omega \overset{\bullet}{P}_{op}) f(x,y) \overline{p}$$

$$= \overline{p} R_{op} f(x,y) + \Omega f(x,y) \overset{\bullet}{P}_{op} \cdot \overline{p}$$

$$= (\rho - \Omega \sigma) f(x,y) \overline{p}$$

$$= (\rho - \Omega \sigma) \overline{S}_\ell \tag{2.9}$$

which implies $a_\ell = \rho - \Omega \sigma$. The problem therefore reduces to solving the
two eigenvalue equations (2.7) and (2.8).

Equation (2.8) is readily solved and the solutions are

$$\overline{p}_\sigma = \frac{1}{\sqrt{2}} \begin{bmatrix} 1 \\ \sigma i \end{bmatrix} \quad ; \quad \sigma = \pm 1. \tag{2.10}$$

We have been assuming that the subscript ℓ on the eigenvector $\overline{S}_\ell$ is a
general counting index which ranges over all possible eigenvectors. At
this point it is advantageous to modify the notation slightly and to
substitute the subscripts n and σ. It is understood that n ranges over the
solutions to (2.7) and σ ranges over the solutions to (2.8). Hence

$$\sum_\ell c_\ell \overline{S}_\ell = \sum_{n,\sigma} c_{n\sigma} \overline{S}_{n\sigma} \tag{2.11}$$

The vectors $\bar{p}_\sigma$ are the _polarization_ eigenvectors of the magnetization. The vector $\bar{p}_{+1}$ corresponds to right-hand circular polarization (thumb in the $\hat{z}$ direction) and $\bar{p}_{-1}$ corresponds to left-hand circular polarization. The choice of the minus sign in equation (2.8) establishes the convention that $\sigma = +1$ corresponds to resonant precession (RCP) of the magnetization.

We now turn our consideration to (2.7). We have

$$(Z - \lambda_{ex} \nabla_t^2) f_n(x,y) = \rho_n f_n(x,y)$$

which can be written

$$\nabla_t^2 f_n(x,y) + \frac{1}{\lambda_{ex}} [\rho_n - Z(x,y)] f_n(x,y) = 0 \tag{2.12}$$

Solutions to this Schrodinger equation will be discussed in the following sections.

The eigenvector-functions $(\bar{S}_{n\sigma})$ discussed in this Section can be thought of as the normal modes of the magnetization or spin wave modes (17).

Note that if $Z(x,y)$ were a constant, (2.12) would be a simple wave equation. If the dimensions of a finite sample were taken into account, only waves with certain discrete wavevectors would be allowed. This was, in fact, the case in the problems discussed by Vendik and Chartorizhskii, and would also be the case if this method were used to describe the Walker modes (69) of a uniformly magnetized sphere. If the sample were infinite but the field were nonuniform, the wavevectors could still be required to be discrete just as the energy levels of a quantum mechanical harmonic

oscillator are discrete. In this manner we shall see that the gradient can confine a mode even in the absence of boundaries.

III. Magnetostatic Waves Guided by One-dimensional Bias Field Profiles

A. General Formalism

In this section we will assume that the bias field is given by a function of x only and that $f_n(x,y)$ is of the form

$$f_n(x,y) = \phi_n(x) \, e^{i\beta y} \tag{2.13}$$

Equation (2.12) becomes

$$\frac{\partial^2 \phi_n(x)}{\partial x^2} + \frac{1}{\lambda_{ex}} [\rho_n - \lambda_{ex} \, \beta^2 - Z(x)] \, \phi_n(x) = 0 \tag{2.14}$$

For the moment we will assume this equaion has been solved and consider the constraints imposed by Maxwell's equations when taken in the magnetostatic limit. These equations are given by

$$\nabla_t \times \overline{h} = 0 \tag{2.15a}$$

$$\nabla_t \cdot (\overline{m} + \overline{h}) = 0. \tag{2.15b}$$

The magnetization is given by

$$\overline{m} = \sum_{n,\sigma} c_{n\sigma} \, \phi_n(x) \, e^{i\beta y} \, \overline{p}_\sigma \tag{2.16}$$

from which $\overline{h}$ is easily obtained:

$$\overline{h} = \sum_{n,\sigma} a_{n\sigma} \, c_{n\sigma} \, \phi_n(x) \, e^{i\beta y} \, \overline{p}_\sigma \tag{2.17}$$

The x and y components of $\overline{m}$ and $\overline{h}$ can be obtained with the aid of equation (2.10):

$$m_x = \frac{1}{\sqrt{2}} \sum_{n,\sigma} c_{n\sigma} \phi_n(x) e^{i\beta y} \tag{2.18a}$$

$$m_y = \frac{i}{\sqrt{2}} \sum_{n,\sigma} \sigma c_{n\sigma} \phi_n(x) e^{i\beta y} \tag{2.18b}$$

$$h_x = \frac{1}{\sqrt{2}} \sum_{n,\sigma} a_{n\sigma} c_{n\sigma} \phi_n(x) e^{i\beta y} \tag{2.19a}$$

$$h_y = \frac{i}{\sqrt{2}} \sum_{n,\sigma} \sigma a_{n\sigma} c_{n\sigma} \phi_n(x) e^{i\beta y} \tag{2.19b}$$

The curl equation (2.15a) requires

$$\frac{\partial h_y}{\partial x} - \frac{\partial h_x}{\partial y} = 0 \tag{2.20}$$

which becomes

$$\sum_{n,\sigma} [a_{n\sigma} c_{n\sigma} (\sigma \frac{\partial \phi_n}{\partial x} - \beta \phi_n)] = 0 \tag{2.21}$$

In a similar way the divergence equation (2.15b) requires

$$\frac{\partial}{\partial x}(m_x + h_x) + \frac{\partial}{\partial y}(m_y + h_y) = 0 \tag{2.22}$$

which becomes

$$\sum_{n,\sigma} \{(1 + a_{n\sigma}) c_{n\sigma} [\frac{\partial \phi_n}{\partial x} - \beta \sigma \phi_n]\} = 0 \tag{2.23}$$

B. Solutions for $\beta = 0$

A significant simplification occurs for the limiting case $\beta = 0$ (this is the cutoff condition for propagation in the y direction). Since the derivatives in (2.21) and (2.23) cannot vanish for all x (except in the trivial case), we have the conditions

$$\sum_{n,\sigma} a_{n\sigma} c_{n\sigma} \sigma = 0 \tag{2.24a}$$

$$\sum_{n,\sigma} (1 + a_{n\sigma}) c_{n\sigma} = 0 \tag{2.24b}$$

for each n. Expanding the summation in (2.24a) gives the relation

$$\frac{c_{n+}}{c_{n-}} = \frac{a_{n-}}{a_{n+}} \tag{2.25}$$

where the subscripts $\pm$ are shorthand for $\sigma = \pm 1$. Substituting this into (2.24b) and making use of the expression for $a_{n\sigma}$ in (2.9) gives

$$\Omega_n^2 = \rho_n (\rho_n + 1) \tag{2.26}$$

where ρ_n is the nth eigenvalue of the equation (cf. equation (2.14))

$$\frac{\partial^2 \phi_n}{\partial x^2} + \frac{1}{\lambda_{ex}} (\rho_n - Z(x)) \phi_n = 0 \tag{2.27}$$

Note that if we can find a solution to (2.27) for a given $Z(x)$ we have found an exact solution to the magnetostatic wave problem for the case $\beta = 0$. In such a case the frequency is given by (2.26), the polarization of the magnetization by (2.25) and $\bar{h}$ and $\bar{m}$ are determined to within an

arbitrary constant by (2.16) and (2.17) evaluated for $\beta = 0$.

C. Linear Bias Field Profile

Consider the following normalized bias field profile:

$$Z(x) = Z_0 + B\ x. \tag{2.28}$$

In the calculations which follow, we consider only the case $\beta = 0$ for simplicity. Equation (2.27) becomes

$$\frac{\partial^2 \phi_n}{\partial x^2} + \frac{1}{\lambda_{ex}} (\rho n - Z_0 - B\ x)\ \phi_n = 0 \tag{2.29}$$

Let us make the following change of variables

$$x = \alpha\ \xi - (Z_0 + \rho_n)/\ B \tag{2.30}$$

where α is a characteristic length to be determined and ξ is a dimensionless variable. Upon this substitution (2.29) becomes

$$\frac{\partial^2 \tilde{\phi}_n(\xi)}{\partial \xi^2} - \frac{B\ \alpha^3}{\lambda_{ex}}\ \xi\ \tilde{\phi}_n(\xi) = 0 \tag{2.31}$$

We can now choose the characteristic length (α) so as to simplify the equation. We therefore choose

$$\alpha = (\lambda_{ex}\ /\ B)^{1/3} \tag{2.32}$$

which gives

$$\frac{\partial^2 \tilde{\phi}_n(\xi)}{\partial \xi^2} - \xi\ \tilde{\phi}_n(\xi) = 0. \tag{2.33}$$

The solutions to this equation are the Airy functions $A_i(\xi)$ and $B_i(\xi)$. If we were considering a general boundary value problem, a linear combination of both functions would be necessary. However, for the present

infinite medium problem only $Ai(\xi)$ is permitted[1]. The solution in terms of x is given by

$$\phi(x) = A_i(x/\alpha + (Z_0 - \rho)/B\alpha). \qquad (2.34)$$

The subscript n is no longer necessary since only one solution is being considered.

According to Morgenthaler (15), the "virtual surface" in the absence of exchange would be located at the point of inflection $\xi = 0$ of the Airy function $A_i(\xi)$. The location of the virtual surface, or turning point, in the x coordinate is then given by equation (2.30):

$$x_{tp} = (\rho - Z_0)/B \qquad (2.35)$$

where the subscript "tp" refers to the turning point. The frequency is given by

$$\Omega^2 = (B x_{tp} + Z_0)(B x_{tp} + Z_0 + 1); \quad B x_{tp} > -Zo \qquad (2.36)$$

which, when $x_{tp} = 0$, reduces to

$$\Omega^2 = Z_0 (Z_0 + 1) \qquad (2.37)$$

which is the same frequency obtained by Morgenthaler (15). Although the present mode does not have precisely the same functional form as a virtual surface mode corrected to include exchange, we see that both theories predict that the turning point occurs at the position where the field places the frequency at the top of the volume wave manifold, which is where the virtual surface occurs in the absence of exchange. (These results are

---

[1]Strictly speaking, our assumptions of a linear bias field profile, an infinite medium and saturation of the magnetization throughout the material are not selfconsistent; there will be some negative x for which the field is not strong enough to saturate the magnetization. We can imagine, hovever, that the material is terminated with a perfectly absorbing boundary at some negative x at which the magnetization is still saturated.

also in exact agreement with those of Eshbach (30) even though he only considered dipolar effects in an approximate way.)

Note that in the present case ρ can assume a continuum of values each corresponding to a different location of the turning point.

This solution can be thought of as a standing wave resulting from a spin wave incident from the left and being totally reflected at the turning point. Equation (2.36) indicates that the higher the frequency of the wave, the further it can penetrate into the material. This can be understood qualitatively through a consideration of the strong field limit ($B\ x_{tp} + Z_0 \gg 1$) from the quasi-particle viewpoint. In this case, equation (2.36) states that the magnon is reflected from the point at which the strength of the potential energy barrier ($\propto B\ x + Z_0$) is equal to the energy of the magnon ($\propto \Omega$).

The possibility that different frequency components may be reflected at different depths into the crystal suggests that a linearly dispersive delay line could be made usign this principle. A major problem with building such a device would be coupling to the very high wavenumber spin waves involved. Based upon earlier work by Strauss (32) and others, Platzker and Morgenthaler (29) have described a linearly dispersive delay line using a linear field profile in a YIG rod. Coupling to the high wavenumber spin waves in their case was accomplished with a clever scheme making use of a backward-wave region of the dispersion diagram (present as a result of the boundary conditions involved) and phonon-magnon coupling. Perhaps a similar scheme could be employed to

fabricate such a delay line using thin films.

If the problem of coupling to these modes can be solved, their presence might be directly confirmed using optical probing. The one-dimensional standing wave pattern described above would appear as alternating stripes of large and small cone angles. This could act as a diffraction pattern for properly polarized and analyzed light passing perpendicularly through the film (33,34).

We have mentioned that the standing wave pattern resulting from a linear field profile would involve very short wavelength (high wavenumber) spin waves. It is instructive to consider a numerical example.

For large negative arguments, the function $A_i(-|\xi|)$ is approximately

$$A_i(-|\xi|) \approx \frac{1}{\pi^{1/2} |\xi|^{1/4}} \sin \left[\frac{2}{3} |\xi|^{3/2} + \pi/4 \right] \qquad (2.38)$$

Because of the $|\xi|^{3/2}$ in the argument, the period of the sinusoid will vary with position. We can estimate the sinusoidal period near a position ξ_0 in the following way:

$$\frac{2}{3}(|\xi_0 + \Delta\xi|^{3/2} - |\xi_0|^{3/2}) = 2\pi$$

which gives $\Delta\xi \approx 2\pi/\sqrt{\xi_0}$. But $\xi \propto x/\alpha$, so

$$\Delta x \approx 2\pi \sqrt{\frac{\alpha^3}{x_0}} \approx 2\pi \sqrt{\frac{\lambda_{ex}}{Bx_0}} . \qquad (2.39)$$

where x_0 is the distance from the "virtual surface." For a gradient such that $B = 1$ cm^{-1} and assuming $\lambda_{ex} = 3 \times 10^{-12}$ cm^2, the wavelength 1 cm from the virtual surface is approximately 0.11 μm.

D. Quadratic Bias Field Profile

1. Basis Eigenvector-Functions

We next consider a normalized field profile of the form[1]

$$Z(x) = Z_0 + Bx^2 \tag{2.40}$$

We begin by considering the problem of an arbitrary β. In this case equation (2.14) becomes

$$\frac{\partial^2 \phi_n(x)}{\partial x^2} + \frac{1}{\lambda_{ex}}(\rho_n - \lambda_{ex}\beta^2 - Z_0 - Bx^2)\,\phi_n(x) = 0 \ . \tag{2.41}$$

As in the linear profile case, it is desirable to express this equation in natural units. We do this by making the change of variable

$$x = \alpha_0 \, \xi \tag{2.42}$$

where α_0 is a characteristic length to be determined and ξ is a dimensionless parameter. Equation (2.41) becomes

$$\frac{\partial^2 \bar{\phi}_n(\xi)}{\partial \xi^2} + \left[\ \frac{\alpha_0^2}{\lambda_{ex}}(\rho_n - Z_0 - \lambda_{ex}\beta^2) - \frac{B\,\alpha_0^4}{\lambda_{ex}}\,\xi^2\ \right]\bar{\phi}_n(\xi) = 0. \tag{2.43}$$

It is now clear that we should choose

$$\alpha_0^4 = \lambda_{ex} / B \tag{2.44}$$

which gives

$$\frac{\partial^2 \bar{\phi}_n}{\partial \xi^2} + \left[\ \frac{(\rho_n - Z_0 - \lambda_{ex}\beta^2)}{\sqrt{B\,\lambda_{ex}}} - \xi^2\ \right]\bar{\phi}_n = 0. \tag{2.45}$$

The solutions to this equation can be immediately obtained by noting that it is of the same form as the one-dimensional harmonic oscillator

[1] The units of the generic gradient parameter, B, vary but should be apparent from the context (cf. equations (2.28) and (2.40)).

equation

$$\frac{\partial^2 \psi}{\partial \xi^2} + (2\epsilon - \xi^2)\,\psi = 0 \qquad (2.46)$$

Acceptable solutions to this equation exist only for discrete eigenvalues which are

$$\epsilon = n + 1/2, \qquad n = 0, 1 \ldots \qquad (2.47)$$

Identifying terms between equations (2.45) and (2.46) gives

$$\rho_n = (2n + 1)\sqrt{B\lambda_{ex}} + Z_0 + \lambda_{ex}\beta^2 \qquad (2.48)$$

or

$$a_{n\sigma} = (2n + 1)\sqrt{B\lambda_{ex}} + Z_0 + \lambda_{ex}\beta^2 - \Omega_n\,\sigma, \quad \sigma = \pm 1. \qquad (2.49)$$

The solutions to (2.45) are the Hermite-Gaussian functions

$$\phi_n(\xi) = \frac{H_n(\xi)\,e^{-\xi^2/2}}{(2^n\,n!\,\sqrt{\pi})^{1/2}} \qquad (2.50a)$$

or

$$\phi_n(x) = \frac{H_n(x/\alpha_0)\,e^{-x^2/2\alpha_0^2}}{(\alpha_0\,2^n\,n!\,\sqrt{\pi})^{1/2}} \qquad (2.50b)$$

where $H_n(\xi)$ is the nth order Hermite polynomial (see Appendix B).

Combining (2.6), (2.10), (2.13) and (2.50b) gives

$$\overline{S}_{n\sigma} = \frac{1}{\sqrt{2}}\begin{bmatrix} 1 \\ i\sigma \end{bmatrix}\phi_n(x)\,e^{i\beta y} \qquad (2.51)$$

Using the orthogonality properties of $\phi_n(x)$ (see Appendix B) it is straightforward to show that these vector-functions are orthonormal:

$$(\overline{S}_{n_1\sigma_1}, \overline{S}_{n_2\sigma_2}) = \int_{-\infty}^{\infty} \overline{S}_{n_1\sigma_1}{}^* \cdot \overline{S}_{n_2\sigma_2}\,dx = \delta_{n_1 n_2}\,\delta_{\sigma_1\sigma_2} \qquad (2.52)$$

2. General Solutions

Using equation (B.13) for the derivative of $\phi_n(x)$ allows us to write Maxwell's equations (2.21) and (2.23) as

$$\sum_\sigma \sum_{n=0}^\infty \left\{ \frac{\sigma \, a_{n\sigma} \, c_{n\sigma}}{\alpha_0} \left[\phi_{n-1}\sqrt{\frac{n}{2}} - \phi_{n+1}\sqrt{\frac{n+1}{2}} \right] - a_{n\sigma} \, c_{n\sigma} \, \beta \, \phi_n \right\} = 0 \quad (2.53)$$

$$\sum_\sigma \sum_{n=0}^\infty \left\{ \frac{(1+a_{n\sigma})}{\alpha_0} \, c_{n\sigma} \left[\phi_{n-1}\sqrt{\frac{n}{2}} - \phi_{n+1}\sqrt{\frac{n+1}{2}} \right] \right.$$

$$\left. - \beta \, \sigma \, (1 + a_{n\sigma}) \, c_{n\sigma} \, \phi_n \right\} = 0 \quad (2.54)$$

Finding the coefficients $(c_{n\sigma})$ and the frequencies (Ω_n) which satisfy these two equations will give the general solutions for the problem. It is useful, however, to consider approximate solutions constructed with only the first $m + 1$ eigenfunctions. The summations in (2.53) and (2.54) can then be reordered to give

$$\sum_\sigma \sum_{n=0}^{m-1} \left[\frac{\sigma \, a_{n+1,\sigma} \, c_{n+1,\sigma}}{\alpha_0} \sqrt{\frac{n+1}{2}} - \frac{\sigma \, a_{n-1,\sigma} \, c_{n-1,\sigma}}{\alpha_0} \sqrt{\frac{n}{2}} \right.$$

$$\left. - \beta \, a_{n\sigma} \, c_{n\sigma} \right] \phi_n$$

$$- \sum_\sigma \left[\frac{\sigma \, a_{m-1,\sigma} \, c_{m-1,\sigma}}{\alpha_0} \sqrt{\frac{n}{2}} + \beta \, a_{m\sigma} \, c_{m\sigma} \right] \phi_m$$

$$- \sum_\sigma \frac{\sigma \, a_{m\sigma} \, c_{m\sigma}}{\alpha_0} \sqrt{\frac{m+1}{2}} \, \phi_{m+1} = 0 \quad (2.55)$$

$$\sum_{\sigma} \sum_{n=0}^{m-1} \left[\frac{(1 + a_{n+1,\sigma})}{\alpha_0} c_{n+1,\sigma} \sqrt{\frac{n+1}{2}} - \frac{(1 + a_{n-1,\sigma})}{\alpha_0} c_{n-1,\sigma} \sqrt{\frac{n}{2}} \right.$$

$$\left. - \beta \sigma (1 + a_{n\sigma}) c_{n\sigma} \right] \phi_n$$

$$- \sum_{\sigma} \left[\frac{(1 + a_{m-1,\sigma})}{\alpha_0} c_{m-1,\sigma} \sqrt{\frac{m}{2}} + \beta \sigma (1 + a_{m\sigma}) c_{m\sigma} \right] \phi_m$$

$$- \sum_{\sigma} \frac{(1 + a_{m\sigma})}{\alpha_0} c_{m\sigma} \sqrt{\frac{m+1}{2}} \phi_{m+1} = 0 \qquad (2.56)$$

In order to satisfy these truncated equations exactly, the coefficient of each ϕ_n must vanish because of orthogonality giving a total of $2m + 4$ equations. However, there are only $2m + 2$ unknowns so that in general the equations cannot be satisfied exactly. To pursue this approach further either of the following procedures can be attempted.

a. Minimize the space average of the equations.

Instead of requiring (2.55) and (2.56) to vanish everywhere, we can try to minimize the average of their absolute squares or absolute values over all space. The equations so obtained would, of course, be nonlinear. In addition, although we constrain Ω_n to be real, the $c_{n\sigma}$ coefficients may be complex resulting in a search for minima in a $4m + 3$ dimensional space!

b. Satisfy the equations exactly at a finite number of points.

Alternatively, we can require the equations to be satisfied at $2m + 2$ points. Although this method results in a set of simultaneous linear equations, it is not clear which points we should choose in order to

optimize the solution.

Because of these difficulties, we will not consider the general solution further. Instead, we will examine these equations for several limiting cases in which significant simplifications occur. The case for $\beta = 0$ has been mentioned already. In addition, the weak gradient ($\sqrt{B\lambda_{ex}} \ll 1$) and strong gradient ($\sqrt{B\lambda_{ex}} \gg 1$) limits will be examined.

3. Solutions for $\beta = 0$

Using the results of Section III.B we can immediately write down solutions for $\beta = 0$. There is a solution for each n given by

$$\overline{m}_n = c_{n+} \overline{S}_{n+} \big|_{\beta=0} + c_{n-} \overline{S}_{n-} \big|_{\beta=0} \qquad (2.57a)$$

$$\overline{h}_n = a_{n+} c_{n+} \overline{S}_{n+} \big|_{\beta=0} + a_{n-} c_{n-} \overline{S}_{n-} \big|_{\beta=0} \qquad (2.57b)$$

where the polarization of the magnetization is

$$\frac{c_{n+}}{c_{n-}} = \frac{a_{n-}}{a_{n+}} \quad , \qquad (2.25)$$

$$a_{n\pm} = (2n + 1)\sqrt{B\lambda_{ex}} + Z_o \mp \Omega_n \, , \qquad (2.58)$$

and the frequency of the nth mode is given by

$$\Omega_n^2 = \left[(2n+1)\sqrt{B\lambda_{ex}} + Z_o\right]\left[(2n+1)\sqrt{B\lambda_{ex}} + Z_o + 1\right] \qquad (2.59)$$

Note in this case that although the magnetization is elliptically polarized, the small signal $\overline{h}$ field is <u>linearly</u> polarized in the x direction (this can be seen by separating (2.57) into x and y components and substituting (2.25) in for the coefficients $c_{n\sigma}$).

It is worth noting that localized non-propagating resonances have been observed in <u>tangentially</u> magnetized thin films (35,36). In such cases it has been proposed (36) that the inhomogeneity in the saturation magnetization near the interface between the gadolinium gallium garnet and yttrium iron garnet could give rise to an effective "potential well" having one bound state. Although the present analysis deals with an inhomogeneous magnetic field rather than magnetization, the two problems appear to be very closely related.

There are an unlimited number of modes in the present case, however, since we have assumed an infinite paraboloidal bias field profile. It is of interest to examine (2.59) in order to get an idea of the frequency separation of these modes. Expanding (2.59) to first order in $\sqrt{B\lambda_{ex}}$ gives

$$\Omega_n = \sqrt{Z_0(Z_0+1)} + \frac{(2n+1)(2Z_0+1)\sqrt{B\lambda_{ex}}}{2\sqrt{Z_0(Z_0+1)}} \qquad (2.60)$$

Using the parameter values (10) of $Z_0 = .78$, $B = 13$ cm^{-2}, $\lambda_{ex} = 3\times10^{-12}$ cm^2 gives

$$\Delta\Omega = \Omega_{n+1} - \Omega_n \simeq 1.4\times10^{-5}.$$

This is at least an order of magnitude smaller than the line-width of the best materials so that it should not be possible to experimentally resolve individual resonances. Instead, they should manifest themselves as a quasi-continuous absorption or transmission band immediately above the volume wave manifold.

It is instructive to find the locations of virtual surfaces for these modes as we did in the case of the linear profile. Using the definition of

α_0 given by equation (2.44), the mode frequencies can be written

$$\Omega_n = \left[(2n+1)B\alpha_0{}^2 + Z_0\right]\left[(2n+1)B\alpha_0{}^2 + Z_0 + 1\right] \qquad (2.61)$$

The frequency which would locate a virtual surface at a position x is given by

$$\Omega^2(x) = Z(x)[Z(x)+1]$$

or $\qquad \Omega^2(x) = [Z_0 + Bx^2][Z_0 + Bx^2 + 1] \qquad (2.62)$

Given the frequency of the nth mode from (2.61), the location of the virtual surface can be obtained from (2.62). Clearly the expressions are equal when $(2n+1)\alpha_0{}^2 = x^2$, or

$$\xi = x/\alpha_0 = \sqrt{2n+1} \qquad (2.63)$$

But this is simply the location of the turning point of the nth Hermite–Gaussian function (see Appendix B). Thus we find, as before with the linear profile, that the location of the virtual surface is coincident with the turning point when exchange is included.

The previous analysis of propagation in a linear gradient also showed that the location of the turning point could be varied continuously by changing the frequency. The higher the frequency, the further into the gradient the wave could penetrate. Said in another way, the spectrum for these waves is not a single resonance but a continuum. The situation in the case of a parabolic profile is very similar. In this case, however, there are two turning points symmetrically located about the center of the well. The additional requirement made by this geometry is that the osscillations must be continuous at the center. This requirement splits

the continuum into a series of resonances which, as we have seen, are very closely spaced for commonly realized gradients. The result is again a quasi-continuous mode spectum. We shall see that this is a characteristic of essentially all of the modes accessible with the present formalism. Such a spin wave continuum was first discussed and observed by Eshbach (30). Eshbach (30) also was first to discuss the behavior of spin waves in linear and quadratic field profiles, although he did not solve for analytic solutions which also satisfy Maxwell's equations in the magnetostatic limit as presented here.

Finally, let us consider the spatial localization for the present example. The characteristic length is given by

$$\alpha_0 = (\lambda_{ex}/B)^{1/4} \simeq 7 \ \mu m.$$

Thus we find that the modes near the top of the manifold are very highly localized.

4. Strong Gradient Limit, $\sqrt{B\lambda_{ex}} \gg 1$

We have already seen that a relatively small gradient can give rise to a highly localized resonance. For very strong gradients we can imagine that the localization would be such that the exchange interaction would completely dominate the resonance and the dipolar interactions could be neglected. In this case equation (2.4) gives

$$\sum_{n,\sigma} a_{n\sigma} c_{n\sigma} \overline{S}_{n\sigma} = 0. \tag{2.64}$$

If all of the $c_{n\sigma}$'s vanished, then so would the magnetization and we would have the null solution. Since we have assumed $\sqrt{B\lambda_{ex}} \gg 1$, all of the

$a_{n\sigma}$'s cannot simultaneously vanish—even in an approximate sense—but they can vanish individually. From (2.49) we see that for $\Omega_n > 0$ only the eigenvalues $a_{n\sigma}$ for $\sigma = +1$ (resonant precession) can vanish. We conclude that each of the vectors $\overline{S}_{n+}$ represents a solution with the frequency

$$\Omega_n = (2n+1)\sqrt{B\lambda_{ex}} + Z_0 + \lambda_{ex}\beta^2. \qquad (2.65)$$

The magnetization for each mode is right hand circularly polarized.
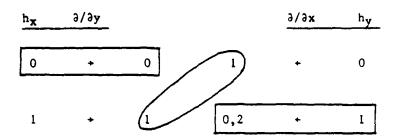
5. Weak Gradient Limit, $\sqrt{B\lambda_{ex}} \ll 1$

Because of the small size of λ_{ex}, the assumption that $\sqrt{B\lambda_{ex}} \ll 1$ is well satisfied in most experimental situations. In this approximation the fact that adjacent $a_{n\sigma}$'s are degenerate introduces a redundancy which reduces the $2m + 4$ equations of Section III.D.2 to an effective set of $2m + 2$ which can be solved exactly.

Expanding equations (2.55) and (2.56) for an arbitrary m quickly becomes cumbersome, so let us first consider a graphical representation of the equations which can quickly give us some insight into which and how many eigenfunctions are needed in order to construct a solution. A more rigorous treatment of this method is given in Appendix C.
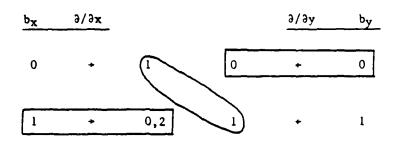
Consider a representation of the curl equation

$$\frac{\partial h_y}{\partial x} - \frac{\partial h_x}{\partial y} = 0 \qquad (2.20)$$

illustrated in Figure 2.2(a). The indices of the Hermite-Gaussian functions we would like to include in a trial solution are listed in the far left and right columns as terms in h_x and h_y, respectively. The

h_x $\partial/\partial y$ $\partial/\partial x$ h_y

| 0 | → | 0 |

1

| 0,2 | ← | 1 |

(a) $\nabla \times \overline{h} = 0$

b_x $\partial/\partial x$ $\partial/\partial y$ b_y

0 →

| 0 | ← | 0 |

| 1 | → | 0,2 |

1

(b) $\nabla \cdot \overline{b} = 0$

Figure 2.2. Diagrams representing Maxwell's
curl and divergence equations.

indices of terms resulting after taking the appropriate derivatives are listed in the inner two columns. By assumption, taking a derivative with respect to y simply gives the same function times a constant ($i\beta$), whereas taking an x derivative gives two terms with raised and lowered indices according to equation (B.13).

Equation (2.20) says that the algebraic sum of all of the terms represented in the inner two columns must vanish. Orthogonality of the functions $\phi_n(x)$ further requires that the sum of all terms with a given index must vanish. Thus the oval enclosing the terms representing $n = 1$ indicates that the difference between these two terms must vanish. Note that there is only one term with $n = 2$ so that its coefficient must vanish. This requires all of the elements enclosed by the rectangular box to vanish since they are all related through non-zero constants. This leaves only one $n = 0$ term so its coefficient must also identically vanish. A similar diagram can be constructed for the $\nabla \cdot \overline{b} = 0$ equation as shown in Figure 2.2(b).

These diagrams indicate that a solution may exist when $h_x \propto \phi_1$ and $h_y \propto \phi_0$. If, on the other hand, all of the terms in both h_x and h_y were required to vanish (as symbolized by enclosing all terms with rectangular boxes), there would be no nontrivial solution for the particular set of ϕ_n's included.

We have said that the diagrams of Figure 2.2 _may_ represent a solution. Experience indicates that solutions will exist only under the following conditions:

1. The eigenvalues ($a_{n\sigma}$) of all included eigenvector-functions ($\bar{S}_{n\sigma}$) must be degenerate in n.

2. The fields in the curl (or divergence) diagram must not identically vanish.

In the present case, both conditions are satisfied since $\sqrt{B\lambda_{ex}} \ll 1$. We conclude that the diagrams of Figure 2.2 do indeed represent a solution.

Before actually calculating the fields for this solution, it is useful to consider a slightly more general case. Let us begin by considering the nth eigenfunction and attempt to construct a solution by adding adjacent eigenfunctions one by one. The diagrams of Figure 2.3 result. Clearly, a solution exists if three consecutive eigenfunctions are included.

We will now calculate the field quantities for this mode. From (2.18) and (2.19) the coefficients which are required to vanish by the rectangular boxes in parts (c) and (d) of Figure 2.3 give

$$\frac{c_{n-1,+}}{c_{n-1,-}} = \frac{a_{n-1,-}}{a_{n-1,+}} \tag{2.66a}$$

$$\frac{c_{n+}}{c_{n-}} = -\frac{a_{n-}}{a_{n+}} \tag{2.66b}$$

$$\frac{c_{n+1,+}}{c_{n+1,-}} = \frac{a_{n+1,-}}{a_{n+1,+}} \tag{2.66c}$$

and

$$\frac{c_{n-1,+}}{c_{n-1,-}} = -\frac{(1 + a_{n-1,-})}{(1 + a_{n-1,+})} \tag{2.67a}$$

$$\frac{c_{n+}}{c_{n-}} = \frac{(1 + a_{n-})}{(1 + a_{n+})} \tag{2.67b}$$

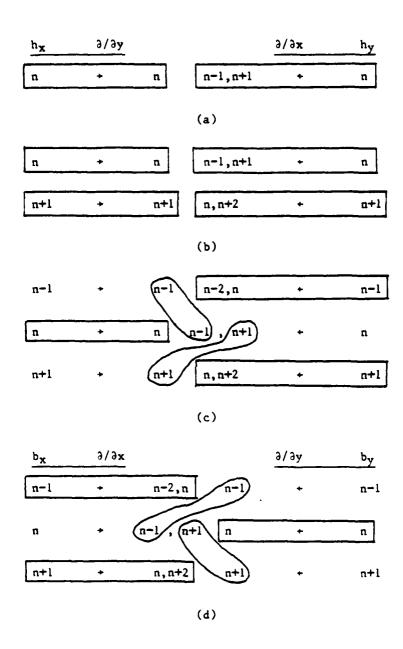$$\frac{c_{n+1,+}}{c_{n+1,-}} = -\frac{(1 + a_{n+1,-})}{(1 + a_{n+1,+})} \tag{2.67c}$$

Figure 2.3. Constructing a solution around the nth eigenfunction.

Equations (2.66) and (2.67) are consistent if

$$a_{n-1,\sigma} \approx a_{n\sigma} \approx a_{n+1,\sigma} \qquad (2.68)$$

and

$$\frac{a_{n-}}{a_{n+}} = -\frac{(1+a_{n-})}{(1+a_{n+})} \qquad (2.69)$$

Equation (2.68) is satisfied if $\sqrt{B\lambda_{ex}} \ll 1$, and equation (2.69) is satisfied when

$$\Omega^2 = \rho_n(\rho_n + 1) \qquad (2.70a)$$

where

$$\rho_n = \begin{matrix} Z_o + \lambda_{ex}\beta^2 & ; \quad n \text{ small} \\ \\ 2n\sqrt{B\lambda_{ex}} + Z_o + \lambda_{ex}\beta^2 & ; \quad n \text{ large.} \end{matrix} \qquad (2.70b)$$

In order to find the relations between the coefficients of different n we make the formal identifications[1]

$$\frac{\partial}{\partial y} \leftrightarrow \beta \qquad (2.71a)$$

$$\frac{\partial}{\partial x} \leftrightarrow \begin{cases} \dfrac{(n/2)^{1/2}}{\alpha_o} & \text{if index is decreased from } n \\ \\ -\dfrac{((n+1)/2)^{1/2}}{\alpha_o} & \text{if index is increased from } n \end{cases} \qquad (2.71b)$$

Requiring the differences between the circled terms in Figure 2.3(c) to vanish gives

$$\beta \; c_{n-1,+} \; g(a_{n+},a_{n-}) - \frac{1}{\alpha_o}\sqrt{\frac{\pi}{2}} \; c_{n+} \; g(a_{n+},a_{n-}) = 0 \qquad (2.72a)$$

---

[1] The i normally obtained in (2.71a) is cancelled by the i which appears as a coefficient of h_y (cf. (2.19b)).

$$\beta \; c_{n+1,+} \; g(a_{n+}, a_{n-}) + \frac{1}{\alpha_0}\sqrt{\frac{n+1}{2}} \; c_{n+} \; g(a_{n+}, a_{n-}) = 0 \qquad (2.72b)$$

where $g(a_{n+}, a_{n-})$ is a common function of each term and can be divided out. We obtain, finally:

$$\frac{c_{n-1,+}}{c_{n+}} = \frac{1}{\beta\alpha_0}\sqrt{\frac{n}{2}} \qquad (2.73a)$$

$$\frac{c_{n+1,+}}{c_{n+}} = -\frac{1}{\beta\alpha_0}\sqrt{\frac{n+1}{2}} \qquad (2.73b)$$

It is easily shown that under the condition $\sqrt{B\lambda_{ex}} \ll 1$ equations (2.73) also satisfy the remaining conditions of Figure 2.3(d).

Having obtained the frequency and the coefficients to within an arbitrary constant we can now write down the fields. We have

$$m_x{}^{(n)} = \frac{c_{n+}}{2\beta\alpha_0}\left\{\sqrt{n}\left[1+\frac{a_{n+}}{a_{n-}}\right]\phi_{n-1} + \beta\alpha_0\sqrt{2}\left[1-\frac{a_{n+}}{a_{n-}}\right]\phi_n + \sqrt{n+1}\left[1+\frac{a_{n+}}{a_{n-}}\right]\phi_{n+1}\right\}$$

$$(2.74a)$$

$$m_y{}^{(n)} = \frac{ic_{n+}}{2\beta\alpha_0}\left\{\sqrt{n}\left[1-\frac{a_{n+}}{a_{n-}}\right]\phi_{n-1} + \beta\alpha_0\sqrt{2}\left[1-\frac{a_{n+}}{a_{n-}}\right]\phi_n + \sqrt{n+1}\left[1-\frac{a_{n+}}{a_{n-}}\right]\phi_{n+1}\right\}$$

$$(2.74b)$$

$$h_x{}^{(n)} = \frac{c_{n+}a_{n+}}{\beta\alpha_0}\left[\sqrt{n}\;\phi_{n-1} - \sqrt{n+1}\;\phi_{n+1}\right] \qquad (2.74c)$$

$$h_y{}^{(n)} = ic_{n+}a_{n+}\sqrt{2}\;\phi_n \qquad (2.74d)$$

$$e_z{}^{(n)} = \frac{c_{n+}\omega\mu_0}{\beta\sqrt{2}}\left[1-\frac{a_{n+}}{a_{n-}}\right]\phi_n \qquad (2.74e)$$

where we have obtained the above approximation to the first order electric
field from the Maxwell equation

$$\nabla \times \overline{e} = - \frac{\partial \overline{b}}{\partial t} \quad . \tag{2.75}$$

Substituting $n = 0$ in the above equations allows us to obtain the
fields for the previously discussed example:

$$m_x^{(o)} = \frac{c_{0+}}{2\beta\alpha_0} \left\{ \beta\alpha_0\sqrt{2}\left[1-\frac{a_{0+}}{a_{0-}}\right]\phi_0 - \left[1+\frac{a_{0+}}{a_{0-}}\right)\phi_1 \right\} \tag{2.76a}$$

$$m_y^{(o)} = \frac{ic_{0+}}{2\beta\alpha_0} \left\{ \beta\alpha_0\sqrt{2}\left[1+\frac{a_{0+}}{a_{0-}}\right]\phi_0 - \left[1-\frac{a_{0+}}{a_{0-}}\right]\phi_1 \right\} \tag{2.76b}$$

$$h_x^{(o)} = - \frac{c_{0+}a_{0+}}{\beta\alpha_0}\phi_1 \tag{2.76c}$$

$$h_y^{(o)} = ic_{0+}a_{0+}\sqrt{2}\,\phi_0 \tag{2.76d}$$

$$e_z^{(o)} = \frac{c_{0+}\omega\mu_0}{\beta\sqrt{2}}\left[1-\frac{a_{0+}}{a_{0-}}\right]\phi_0 \tag{2.76e}$$

Note that the net electromagnetic power flow in the y direction is zero
for all of the waves described by (2.74) because of the orthogonality of
the Hermite–Gaussian functions:

$$P_y^{(em)} = \frac{1}{2}\,\mathrm{Re}\left\{ \int_{-\infty}^{\infty}(\overline{e}\times\overline{h}^*)\cdot\hat{i}_y\,dx \right\}$$

$$= \frac{1}{2}\int_{-\infty}^{\infty}e_z h_x\,dx$$

$$\propto \int_{-\infty}^{\infty} \phi_n(x)\phi_{n-1}(x) \ dx \ + \ \int_{-\infty}^{\infty} \phi_n(x)\phi_{n+1}(x) \ dx$$

$$= 0. \tag{2.77}$$

Thus the power flow in these modes is carried entirely by the exchange channel. The resulting group velocity can be estimated by expanding (2.70a) to lowest order in $\lambda_{ex}\beta^2$ and taking the derivative with respect to β. The result for n small is

$$v_g = \frac{2Z_0 + 1}{\sqrt{Z_0(Z_0 + 1)}} \ \omega_m\lambda_{ex}\beta \tag{2.78}$$

It should also be pointed out that the waves described by equations (2.74) are not all mutually orthogonal with respect to the inner product

$$(\overline{F}_i,\overline{F}_j) = \int_{-\infty}^{\infty} \overline{F}_i{}^* \cdot \overline{F}_j \ dx$$

where $\overline{F}_i$ is any field quantity of the ith solution. The solution for n is orthogonal to those for n-1 and n+1, but it is not orthogonal to the solutions for n+2 and n-2. Hence the modes for n=0 and n=1 can be taken to be the first two solutions of an orthogonal set, but solutions for n⩾3 must be carefully constructed so as to be orthogonal to all lower solutions.

IV. <u>Magnetostatic</u> <u>Resonances</u> <u>Bound</u> <u>to</u> <u>Two-dimensional</u> <u>Quadratic</u> <u>Bias</u> <u>Field</u> <u>Profiles</u>

A. Basis Eigenvector-functions

We would now like to consider normalized bias field profiles of the form

$$Z(x,y) = Z_0 + B_x x^2 + B_y y^2. \tag{2.79}$$

The eigenvalue equation (2.12) becomes

$$\frac{\partial^2 \phi}{\partial x^2} + \frac{\partial^2 \phi}{\partial y^2} + \frac{1}{\lambda_{ex}}[a + \Omega\sigma - Z_0 - B_x x^2 - B_y y^2] \phi = 0. \tag{2.80}$$

which is of the same form as the two-dimensional harmonic oscillator equation. Following the usual procedure of separation of variables, the solutions can be easily shown to be products of one-dimensional Hermite-Gaussian functions (Appendix B). The eigenvalues are calculated to be

$$a_{n_x n_y \sigma} = \sqrt{B_x \lambda_{ex}} \; (2n_x+1) + \sqrt{B_y \lambda_{ex}} \; (2n_y+1) + Z_0 - \Omega\sigma \; . \tag{2.81}$$

and the eigenvector-functions are given by

$$\bar{S}_{n_x n_y \sigma} = \frac{1}{\sqrt{2}} \begin{bmatrix} 1 \\ i\sigma \end{bmatrix} \phi_{n_x}(x) \; \phi_{n_y}(y) \tag{2.82}$$

where $\phi_{n_x}(x)$ and $\phi_{n_y}(y)$ are properly normalized one-dimensional harmonic oscillator wavefunctions as defined by equation (2.50b). These eigenvector-functions are orthonormal in the sense that

$$\int_{-\infty}^{\infty} \int_{-\infty}^{\infty} dxdy \; \overline{S}_{n_x n_y \sigma}^* \cdot \overline{S}_{m_x m_y \sigma'} = \delta_{n_x, m_x} \; \delta_{n_y, m_y} \; \delta_{\sigma, \sigma'} \qquad (2.83)$$

B. General Solutions

We assume that the eigenvector-functions (2.82) form a complete set so that $\overline{m}$ and $\overline{h}$ can be expanded in terms of them. We can then write

$$\overline{m} = \sum_{\substack{n_x, n_y \\ \sigma}} c_{n_x n_y \sigma} \; \overline{S}_{n_x n_y \sigma} \qquad (2.84a)$$

$$\overline{h} = \sum_{\substack{n_x, n_y \\ \sigma}} a_{n_x n_y \sigma} \; c_{n_x n_y \sigma} \; \overline{S}_{n_x n_y \sigma} \qquad (2.84b)$$

The individual components of these fields are found to be

$$m_x = \frac{1}{\sqrt{2}} \sum_{\substack{n_x, n_y \\ \sigma}} c_{n_x n_y \sigma} \; \phi_{n_x} \phi_{n_y} \qquad (2.85a)$$

$$m_y = \frac{i}{\sqrt{2}} \sum_{\substack{n_x, n_y \\ \sigma}} \sigma \; c_{n_x n_y \sigma} \; \phi_{n_x} \phi_{n_y} \qquad (2.85b)$$

$$h_x = \frac{1}{\sqrt{2}} \sum_{\substack{n_x, n_y \\ \sigma}} a_{n_x n_y \sigma} \; c_{n_x n_y \sigma} \; \phi_{n_x} \phi_{n_y} \qquad (2.86a)$$

$$h_y = \frac{i}{\sqrt{2}} \sum_{\substack{n_x, n_y \\ \sigma}} \sigma \; a_{n_x n_y \sigma} \; c_{n_x n_y \sigma} \; \phi_{n_x} \phi_{n_y} \qquad (2.86b)$$

Applying the curl equation (2.20) to (2.86) and using equation (B.13) for the derivatives gives

$$\sum_{n_x,n_y} \sum_\sigma \{\frac{i\sigma}{\alpha_x} a_{n_x n_y \sigma} c_{n_x n_y \sigma}[\phi_{n_x-1}\sqrt{\frac{n_x}{2}} - \phi_{n_x+1}\sqrt{\frac{n_x+1}{2}}]\phi_{n_y}$$

$$- \frac{1}{\alpha_y} a_{n_x n_y \sigma} c_{n_x n_y \sigma}\phi_{n_x}[\phi_{n_y-1}\sqrt{\frac{n_y}{2}} - \phi_{n_y+1}\sqrt{\frac{n_y+1}{2}}]\} = 0 \quad (2.87)$$

Similarly, the divergence equation (2.22) becomes

$$\sum_{n_x,n_y} \sum_\sigma \{\frac{(1+a_{n_x n_y \sigma})}{\alpha_x} c_{n_x n_y \sigma}[\phi_{n_x-1}\sqrt{\frac{n_x}{2}} - \phi_{n_x+1}\sqrt{\frac{n_x+1}{2}}]$$

$$+ \frac{i\sigma(1+a_{n_x n_y \sigma})}{\alpha_y} c_{n_x n_y \sigma}\phi_{n_x}[\phi_{n_y-1}\sqrt{\frac{n_y}{2}} - \phi_{n_y+1}\sqrt{\frac{n_y+1}{2}}]\} = 0 \quad (2.88)$$

If we wish to keep only a finite number of terms in these equations we must specify precisely how we are going to count terms. In order to do this, let us define a principle eigenfunction index n such that

$$n = n_x + n_y. \quad (2.89)$$

We will truncate the series by keeping all of the terms (n_x,n_y) such that $n_x + n_y \leq n$. Equations (2.87) and (2.88) can then be written

$$\sum_{n_x=0}^{n} \sum_{n_y=0}^{n-n_x} \sum_\sigma \{ \frac{i\sigma}{\alpha_x} \sqrt{\frac{n_x}{2}} a_{n_x n_y \sigma} c_{n_x n_y \sigma} \psi_{n_x-1,n_y}$$

$$- \frac{i\sigma}{\alpha_x} \sqrt{\frac{n_x+1}{2}} a_{n_x n_y \sigma} c_{n_x n_y \sigma} \psi_{n_x+1,n_y}$$

$$- \frac{1}{\alpha_y} \sqrt{\frac{n_y}{2}} a_{n_x n_y \sigma} c_{n_x n_y \sigma} \psi_{n_x,n_y-1}$$

$$+ \frac{1}{\alpha_y} \sqrt{\frac{n_y+1}{2}} a_{n_x n_y \sigma} c_{n_x n \sigma} \psi_{n_x,n_y+1} \} = 0 \quad (2.90)$$

$$\sum_{n_x=0}^{n} \sum_{n_y=0}^{n-n_x} \sum_{\sigma} \Big\{ \frac{1}{\alpha_x} \sqrt{\frac{n_x}{2}} (1+a_{n_x n_y \sigma}) c_{n_x n_y \sigma} \psi_{n_x-1,n_y}$$

$$- \frac{1}{\alpha_x} \sqrt{\frac{n_x+1}{2}} (1+a_{n_x n_y \sigma}) c_{n_x n_y \sigma} \psi_{n_x+1,n_y}$$

$$+ \frac{i\sigma}{\alpha_y} \sqrt{\frac{n_y}{2}} (1+a_{n_x n_y \sigma}) c_{n_x n_y \sigma} \psi_{n_x,n_y-1}$$

$$- \frac{i\sigma}{\alpha_y} \sqrt{\frac{n_y+1}{2}} (1+a_{n_x n_y \sigma}) c_{n_x n_y \sigma} \psi_{n_x,n_y+1} \Big\} = 0 \qquad (2.91)$$

where $\psi_{n_x,n_y} = \phi_{n_x}(x)\phi_{n_y}(y)$.

The solution to the general problem would be obtained by finding the coefficients, $c_{n_x n_y \sigma}$, and eigenvalues, $a_{n_x n_y \sigma}$, which satisfy—or minimize in some sense—equations (2.90) and (2.91).

Fortunately, it is possible to find a set of solutions which exactly satisfies these equations when $B_x = B_y$. These solutions, as well as a number of approximate solutions, are discussed in the following sections.

C. Solutions for $B_x = B_y$

In order to avoid the complications of expanding equations (2.90) and (2.91) without a good idea of how many and which terms to include, we will first explore different combinations graphically using a straightforward extension of the method discussed in Section III.D.5. The rules indicating the existence of solutions generalized to the present case of a finite number of two-dimensional Hermite-Gaussian functions are:

1. The eigenvalues $(a_{n_x n_y \sigma})$ of all included eigenvector-functions $(\bar{S}_{n_x n_y \sigma})$ must be degenerate in (n_x, n_y).

2. The fields in the curl (or divergence) diagram must not identically vanish.

The first condition is met for all neighboring eigenvector-functions in the weak gradient limit ($\sqrt{B_i \lambda_{ex}} \ll 1$, $i=x,y$). It is also met for all eigenvector-functions belonging to the same principle eigenfunction index when $B_x = B_y$. This latter case is the one we will examine in this section.

The curl equation diagrams for the first four principle eigenfunction indices are shown in Figure 2.4. It appears that no solutions are possible for n even, but solutions do exist for n odd.

The fields can be obtained from the diagrams in a manner very similar to the one-dimensional case discussed earlier. We first make the formal identifications:

$$\frac{\partial}{\partial \nu} \leftrightarrow \begin{cases} \dfrac{1}{\alpha_\nu} \sqrt{\dfrac{n_\nu}{2}} & \text{if index is decreased from } n_\nu, \\[3mm] -\dfrac{1}{\alpha_\nu} \sqrt{\dfrac{n_\nu + 1}{2}} & \text{if index is increased from } n_\nu. \end{cases} \tag{2.92}$$

We must also remember that the y component of each field quantity has a factor of i (this factor was cancelled by the i in $\partial/\partial\beta \to i\beta$ in the previous case).

Let us first consider the solution for n=1. The components of h_x and h_y which are required to vanish by Figure 2.4(b) imply

$$h_x \qquad \partial/\partial y \qquad\qquad\qquad \partial/\partial x \qquad h_y$$

| 00 | → | 01 |

| 10 | ← | 00 |

(a) Fields vanish for n=0.

| 01 | → | 00,02 | 11 | ← | 01 |

10 → 11 | 00,20 | ← | 10 |

(b) A solution exists for n=1.

| 02 | → | 01,03 |

| 12 | ← | 02 |

| 1! | → | 10,12 |

| 01,21 | ← | 11 |

| 20 | → | 21 |

| 10,30 | ← | 20 |

(c) Fields vanish for n=2.

| 03 | → | 02,04 | 13 | ← | 03 |

12 → 11 , 13 | 02,22 | ← | 12 |

| 21 | → | 20,22 | 11 , 31 | ← | 21 |

30 → 31 | 20,40 | ← | 30 |
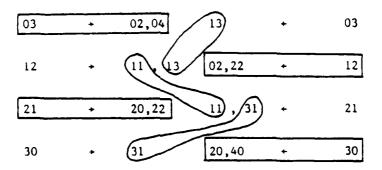
(d) A solution exists for n=3.

Figure 2.4. Curl Diagrams.

$$\frac{c_{o1+}}{c_{o1-}} = -\frac{a_{1-}}{a_{1+}} \tag{2.93a}$$

$$\frac{c_{1o+}}{c_{1o-}} = \frac{a_{1-}}{a_{1+}} \tag{2.93b}$$

Referring to Figure 2.5, the components of b_x and b_y which are required to vanish give

$$\frac{c_{o1+}}{c_{o1-}} = \frac{(1+a_{1-})}{(1+a_{1+})} \tag{2.94a}$$

$$\frac{c_{1o+}}{c_{1o-}} = -\frac{(1+a_{1-})}{(1+a_{1+})} \tag{2.94b}$$

Equations (2.93) and (2.94) can be satisfied only if

$$\Omega_1^2 = \left[4\sqrt{B\lambda_{ex}} + Z_o\right]\left[4\sqrt{B\lambda_{ex}} + Z_o + 1\right] \tag{2.95}$$

where we have used

$$a_{n\sigma} = 2\sqrt{B\lambda_{ex}}\ (n+1) + Z_o - \Omega\sigma \tag{2.96}$$

and $B = B_x = B_y$.

Requiring the difference between the terms enclosed by the oval in either the curl or divergence diagrams to vanish gives the relationship between the (01) and (10) eigenfunctions. From the curl equation we have

$$-\frac{1}{\alpha\sqrt{2}}\ c_{1o+}\ g(a_{1+},a_{1-}) + \frac{i}{\alpha\sqrt{2}}\ c_{o1+}\ g(a_{1+},a_{1-}) = 0$$

where $g(a_{1+},a_{1-})$ is a function common to both terms. This equation simplifies to

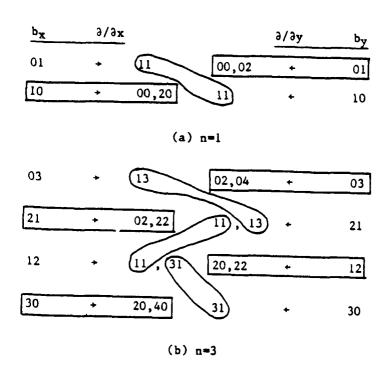$$\frac{c_{1o+}}{c_{o1+}} = i \tag{2.97}$$

Figure 2.5. Divergence Diagrams

We now have all of the information needed to write down the fields for the solution. We have

$$m_x^{(1)} = \frac{c_{o1+}}{\sqrt{2}} \left\{ \left[1 - \frac{a_{1+}}{a_{1-}}\right]\psi_{o1} + i\left[1 + \frac{a_{1+}}{a_{1-}}\right]\psi_{1o}\right\} \tag{2.98a}$$

$$m_y^{(1)} = \frac{ic_{o1+}}{\sqrt{2}} \left\{ \left[1 + \frac{a_{1+}}{a_{1-}}\right]\psi_{o1} + i\left[1 - \frac{a_{1+}}{a_{1-}}\right]\psi_{1o}\right\} \tag{2.98b}$$

$$h_x^{(1)} = ic_{o1+} \sqrt{2} \; a_{1+} \; \psi_{1o} \tag{2.98c}$$

$$h_y^{(1)} = ic_{o1+} \sqrt{2} \; a_{1+} \; \psi_{o1} \tag{2.98d}$$

$$e_z^{(1)} = -i\omega\mu_o 2c_{o1+}(1+a_{1+})\alpha \; \psi_{oo} \tag{2.98e}$$

Spatial maps of the field strengths and polarizations of $\bar{m}$ and $\bar{h}$ are presented in Figure 2.6. Note that $\bar{h}$ is linearly polarized.

Repeating this procedure for n=3 (see Figures 2.4(d) and 2.5(b)) we obtain the following fields:

$$m_x^{(3)} = \frac{c_{o3+}}{\sqrt{2}} \left\{ \left[1 - \frac{a_{3+}}{a_{3-}}\right]\psi_{03} + \frac{i}{\sqrt{3}}\left[1 + \frac{a_{3+}}{a_{3-}}\right]\psi_{12} + \frac{1}{\sqrt{3}}\left[1 - \frac{a_{3+}}{a_{3-}}\right]\psi_{21} + i\left[1 + \frac{a_{3+}}{a_{3-}}\right]\psi_{30}\right\} \tag{2.99a}$$

$$m_y^{(3)} = \frac{ic_{o3+}}{\sqrt{2}} \left\{ \left[1 + \frac{a_{3+}}{a_{3-}}\right]\psi_{03} + \frac{i}{\sqrt{3}}\left[1 - \frac{a_{3+}}{a_{3-}}\right]\psi_{12} + \frac{1}{\sqrt{3}}\left[1 + \frac{a_{3+}}{a_{3-}}\right]\psi_{21} + i\left[1 - \frac{a_{3+}}{a_{3-}}\right]\psi_{30}\right\} \tag{2.99b}$$

$$h_x^{(3)} = ic_{o3+}\sqrt{2} \; a_{3+}\left[\frac{\psi_{12}}{\sqrt{3}} + \psi_{30} \right] \tag{2.99c}$$

$$h_y^{(3)} = ic_{o3+}\sqrt{2} \; a_{3+}\left[\psi_{03} + \frac{\psi_{21}}{\sqrt{3}} \right] \tag{2.99d}$$
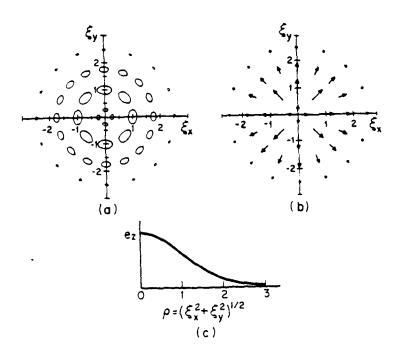
Figure 2.6. Fields of the n=1 solution in the presence of a z directed bias field which is a symmetric paraboloid of revolution. (a) Relative magnitude and polarization of m̄. The ellipses indicate the locus of points traced by the tip of the small signal magnetization vector as it rotates counterclockwise. (b) Relative magnitude and polarization of h̄.
(c) Relative magnitude of the z directed electric field (e_z). Unlike m̄, both h̄ and ē are linearly polarized.

$$e_z^{(3)} = -i\omega\mu_o c_o 3 + (1+a_3+)\alpha \frac{2}{\sqrt{3}} \left[\sqrt{2}\, \psi_{00} + \psi_{02} + \psi_{20} \right] \qquad (2.99e)$$

and

$$\Omega_3^2 = \left[8\sqrt{B\lambda_{ex}} + Z_o \right]\left[8\sqrt{B\lambda_{ex}} + Z_o + 1 \right] . \qquad (2.100)$$

Spatial maps of the field strengths and polarizations for this solution are shown in Figure 2.7.

In general, a solution can be constructed from the n+1 eigenvector-functions belonging to the principle eigenfunction index n when n is odd. The nth solution has rotational symmetry about the z axis and the magnetic field has (n+1)/2 radial nodes. The frequency of the nth solution is given by

$$\Omega_n^2 = \left[2\sqrt{B\lambda_{ex}}\,(n+1) + Z_o \right]\left[2\sqrt{B\lambda_{ex}}\,(n+1) + Z_o + 1 \right] \qquad (2.101)$$

D. Strong Gradient Limit, $\sqrt{B\lambda_{ex}} \gg 1$

If the magnetic field gradient is so large that the exchange interaction completely dominates the behavior of the magnetization, the magnetization can be approximated by any of the eigenvector-functions which can have a zero eigenvalue. The solutions are

$$\bar{m}_{n_x n_y +} = \frac{c_{n_x n_y +}}{\sqrt{2}} \begin{bmatrix} 1 \\ i \end{bmatrix} \phi_{n_x}(x)\phi_{n_y}(y) \qquad (2.102)$$

and the frequencies are given by

$$\Omega_{n_x n_y +} = \sqrt{B_x\lambda_{ex}}\,(2n_x + 1) + \sqrt{B_x\lambda_{ex}}\,(2n_y + 1) + Z_o \qquad (2.103)$$
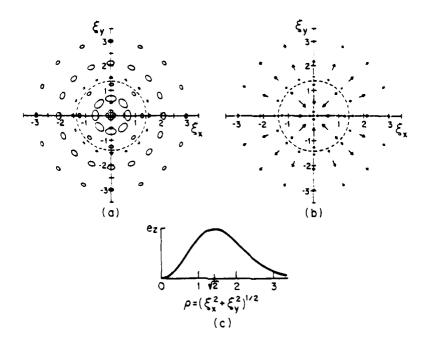
Figure 2.7. Fields for n=3 solution. (a) Magnitude and polarization of $\overline{m}$, (b) Magnitude and polarization of $\overline{h}$, (c) Magnitude of e_z.
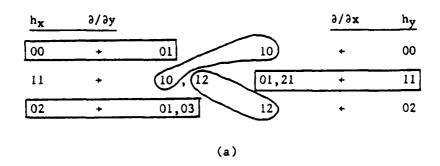
Here, as in the one-dimensional field profile of Section III.D.3, the magnetization of each mode is right hand circularly polarized.

It is interesting to note that when B_x and B_y differ slightly, the spectrum of resonances given by equation (2.103) consists of a series of multiplets qualitatively very similar to those observed by Cooley in a disk (37). However, in order for the resonances to differ by only a few megahertz for YIG ($f_m \simeq 5$ GHz) we must have $\sqrt{B\lambda_{ex}} \simeq 10^{-3}$, or $B \simeq 3(10^5)$ cm^{-2}. We conclude that although the qualitative behavior of equation (2.103) is very suggestive, it is extremely unlikely that field gradients of this magnitude existed in the experiment reported by Cooley! This disagreement results in part from our neglect of surface magnetic poles which in the magnetostatic modes of a disk, as in the Walker modes of a sphere (69), play a dominant role in determining the mode characteristics. It is therefore possible that Cooley's results could be explained by a similar analysis if the effects of finite sample edges were included.

E. Weak Gradient Limit $\sqrt{B\lambda_{ex}} \ll 1$

When terms of order $\sqrt{B\lambda_{ex}}$ can be neglected, combinations of eigenvector-functions from adjacent principle eigenfunction indices may be considered as a trial solution. Clearly the "exact" solutions of Section IV.C are also valid in this limit when $B_x = B_y$. In addition, similar solutions can be found when $B_x \neq B_y$ if the fields are rederived taking into consideration that $\alpha_x \neq \alpha_y$ (this will destroy the symmetry and elongate the mode patterns in the direction of the weakest gradient).

Since we are no longer restricted to eigenvector-functions belonging to the same principle eigenfunction index, the diagrams shown in Figure 2.8 may now be considered. Notice that the diagrams shown in Figure 2.8(a) and
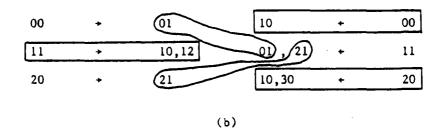
Figure 2.8. Curl diagrams for combinations of n = 0 and n = 2 eigenvector-functions.

2.8(b) transform into one another under the interchange of x and y. Thus the two solutions are equivalent under a rotation of $\pi/2$ about the z axis[1]. It is sufficient, then, to consider the solution represented by Figure 2.8(a).

Following a now familiar procedure, the fields corresponding to Figure 2.8(a) are found to be

$$m_x = \frac{c_{oo+}}{\sqrt{2}} \left\{ \left[1-\frac{a_+}{a_-}\right]\psi_{00} - \frac{i\alpha_y}{\alpha_x} \left[1+\frac{a_+}{a_-}\right]\psi_{11} - \sqrt{2} \left[1-\frac{a_+}{a_-}\right]\psi_{02} \right\} \tag{2.104a}$$

$$m_y = \frac{ic_{oo+}}{\sqrt{2}} \left\{ \left[1+\frac{a_+}{a_-}\right]\psi_{00} - \frac{i\alpha_y}{\alpha_x} \left[1-\frac{a_+}{a_-}\right]\psi_{11} - \sqrt{2} \left[1+\frac{a_+}{a_-}\right]\psi_{02} \right\} \tag{2.104b}$$

$$h_x = -ic_{oo+}\sqrt{2}\; a_+ \frac{\alpha_y}{\alpha_x} \psi_{11} \tag{2.104c}$$

$$h_y = ic_{oo+} \sqrt{2}\; a_+(\psi_{00} - \sqrt{2}\; \psi_{02}) \tag{2.104d}$$

$$e_z = i\omega\mu_o c_{oo+}2(1+a_+)\alpha_y\; \psi_{01} \tag{2.104e}$$

and

$$\Omega^2 = Z_0(Z_0 + 1), \tag{2.105}$$

where $a_\sigma \approx Z_0 - \Omega\sigma$. Spatial maps of the field strengths and polarizations for this solution are shown in Figure 2.9.

In the weak gradient limit, all solutions near a given n have approximately the same frequency which for large n is approximately

$$\Omega_n^2 = \left[2n\sqrt{B\lambda_{ex}} + Z_o\right]\left[2n\sqrt{B\lambda_{ex}} + Z_o + 1\right] \tag{2.106}$$

Again, we find that the frequencies of the modes are so closely spaced that they form a quasi-comtinuum.

---

[1]The diagrams do not explicitly indicate the signs of the quantities involved. The actual transformation is $x \rightarrow y$, $y \rightarrow -x$.
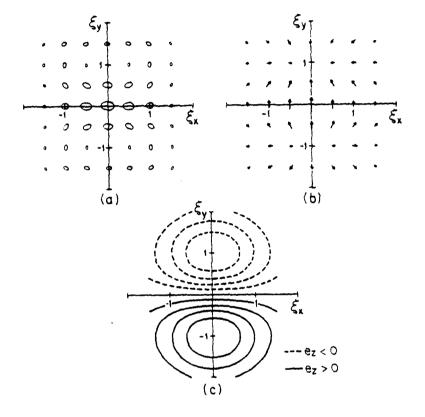
Figure 2.9. Fields of the lowest order solution which does not possess rotational symmetry about the z axis even when the bias field is symmetric. The format is similar to that of Figure 2.6. (a) Magnitude and polarization of $\bar{m}$. (b) Magnitude and polarization of $\bar{h}$. (c) Contour map of e_z.

It should be possible to construct additional solutions in such a way that the solution of this Section and the solutions of Section IV.C in the limit $\sqrt{B\lambda_{ex}} \ll 1$ are three of the lowest order solutions of a complete orthogonal set.

V. Discussion

If exchange were neglected, the dispersion relation for $\overline{k} \perp \overline{H}$ in an infinite medium (or in a normally magnetized slab between conducting plates) is simply $\Omega^2 = Z_0(Z_0+1)$, independent of β. Hence in the virtual surface theory (1,2), at the point in the material where the field and frequency have this relationship all wavelengths are possible. Qualitatively, this gives an idea of how a singularity in the field might be possible at this point.

The addition of exchange, on the other hand, lifts this degeneracy and results in a one-to-one correspondence between Ω and β, thus eliminating the possibility of a singularity. In the case of a nonuniform field, the resulting mode is oscillatory in regions of the sample where propagation is permitted, and decays rapidly outside of these regions.

This suggests a mechanism whereby a gradient could localize a mode in a thin slab with the conducting plates removed. As shown in Appendix A, the effect of the new boundary conditions is to introduce a component of $\overline{e} \times \overline{h}$ power flow which, in most cases, dominates the power flow in the exchange channel. Hence one can imagine a mode which again can propagate in some regions and not in others, but whose propagation characteristics are determined completely by the magnetostatic boundary conditions rather than

exchange. This general concept of mode localization should not be limited to volume waves, but should apply to other bias field orientations as well. It is, in fact, the conceptual basis for the surface wave theory described in Chapter Three.

Finally, two limitations of the present theory deserve mention:

1. In many cases (including that of Eshbach (30)) the magnetoelastic crossover point occurs within frequencies of interest and cannot be neglected. The present theory is strictly valid only where this is not the case.

2. As pointed out in the introduction, these solutions lose their validity if the turning point occurs near the edge of a finite width/diameter film. In such a case, the second solution to the harmonic oscillator equation (which does not vanish at infinity) must be included in the eigenfunction expansion.

VI. Summary of Chapter

We have extended the method of expansion in normal spin wave modes (17,18) to the case of a two-dimensional non-uniformly magnetized ferrite with the effects of exchange included. Using this method, a number of solutions (both exact and approximate) to the linearized magnetostatic equations have been obtained.

A consideration of the special case of a one-dimensional linear bias field profile and propagation parallel to the gradient showed that the profile of the magnetization is given by an Airy function. The turning point of the Airy function was shown to correspond to the location of a

virtual surface in qualitative agreement with previous work by Morgenthaler
(15). In addition, it was shown that the distance penetrated into the
gradient is roughly proportional to the frequency of the spin wave.

Next, spin wave propagation down a "trough" formed by a one-dimensional
parabolic bias field was considered. It was shown that solutions to the
magnetostatic problem can be constructed from basis vector-functions
consisting of the product of a polarization vector and a Hermite-Gaussian
function. In the weak gradient limit, $\sqrt{B\lambda_{ex}} \ll 1$, it was shown that the
wave can be localized to a very narrow "trough" (as narrow as 15 um for
$B = 12$ cm^{-2}) when the frequency is very near the top of the volume wave
manifold. The net Poynting flux was found to be zero, however, indicating
that power can flow only through the exchange channel.

Finally, localized resonances confined by two-dimensional parabolic
bias field profiles were considered. In this case, basis vector-functions
consisting of the product of a polarization vector and a two-dimensional
Hermite-Gaussian function can be used to construct solutions to the
magnetostatic problem. A class of exact solutions (good for any strength
quadratic gradient) was found for the symmetric case $B_x = B_y$.

Both the frequencies and field distributions of the solutions are in
agreement with the spin wave continuum discussed and observed by Eshbach
(30).

These solutions, free of the singularities encountered in the virtual
surface theory, demonstrate that exchange can play an important role in the
localization of magnetostatic waves in nonuniform bias fields.

Dispersion Relations for Magnetostatic Waves in Thin Ferrite Films

I. Background

Magnetostatic waves in a ferrite slab with an in-plane magnetic field were first discussed by Damon and Eshbach (54) in 1961, and waves in a normally magnetized slab were first discussed by Damon and Van de Vaart (55) in 1965. since these initial studies, various modifications have been made to the basic theories. Some of the most notable of these are:

1. Effects of a nearby parallel ground plane (56-59)

2. Effects of crystalline anisotropy (51,60-64)

3. Effects of finite slab width (38,44,65,66)

In the following sections we derive the general suscepcibility tensor including anisotropy and exchange and present the basic equations of magnetostatics. We then derive the basic dispersion relations for the three principle normal modes of an isolated, isotropic, infinite width slab. Dispersion relations for ferrite-dielectric-metal and finite width geometries are also given but without derivation.

II. The General Susceptibility Tensor

The equation of motion for the magnetization is given by

$$\frac{\partial \overline{M}}{\partial t} = \gamma \mu_0 \overline{M} \times (\overline{H} + \overline{H}_a + \overline{H}_{ex}) \qquad (A.1)$$

where $\gamma = -g|e|/2m$ is the gyromagnetic ratio, $\overline{M}$ is the magnetization, $\overline{H}$ is the Maxwellian field, and $\overline{H}_a$ and $\overline{H}_{ex}$ are effective fields due to anisotropy and exchange, respectively. The effective fields are defined by

$$\overline{H}_a = -\frac{1}{\mu_o}\frac{\partial W^a}{\partial \overline{M}} \qquad\qquad\qquad\qquad (A.2a)$$

$$\overline{H}_{ex} = \lambda_{ex}\,\nabla^2\overline{M} \qquad\qquad\qquad\qquad (A.2b)$$

where W^a is the anisotropy energy density (Section III) and λ_{ex} is a phenomenological constant equal to approximately $3(10^{-12})$ cm^2 for YIG.

Following the usual linearization procedure, these fields are divided into static and time varying components as follows:

$$\overline{M} = \overline{M}_o + \overline{m} \qquad\qquad\qquad\qquad (A.3a)$$

$$\overline{H} = \overline{H}_o + \overline{h} \qquad\qquad\qquad\qquad (A.3b)$$

$$\overline{H}_a = \overline{H}_{oa} + \overline{h}_a \qquad\qquad\qquad\qquad (A.3c)$$

$$\overline{H}_{ex} = \overline{H}_{oex} + \overline{h}_{ex} \qquad\qquad\qquad\qquad (A.3d)$$

The field $\overline{H}_o$ should understood to be the vector sum of the actual externally applied magnetic field and the internal demagnetizing field, but we will not explicitly indicate this in order to avoid further notational complexity. Making these substitutions into (A.1) and assuming the time variation $\exp(-i\omega t)$ gives

$$\frac{-i\omega\bar{m}}{\gamma\mu_0} = \bar{M}_0 \times [\bar{H}_0 + \bar{H}_{oa} + \bar{H}_{oex}] + \bar{M}_0 \times [\bar{h} + \bar{h}_a + \bar{h}_{ex}]$$

$$+ \bar{m} \times [\bar{H}_0 + \bar{H}_a + \bar{H}_{ex}] + \bar{m} \times [\bar{h} + \bar{h}_a + \bar{h}_{ex}] \qquad (A.4)$$

The equilibrium direction of the magnetization is determined by the equation

$$\bar{M}_0 \times [\bar{H}_0(\bar{M}_0) + \bar{H}_a(\bar{M}_0) + \bar{H}_{oex}(\bar{M}_0)] = 0 \qquad (A.5)$$

where we have explicitly indicated the dependence of $\bar{H}_0$, $\bar{H}_{oa}$, and $\bar{H}_{oex}$ on $\bar{M}_0$. The dependence of $\bar{H}_0$ on $\bar{M}_0$ results from the demagnetizing field mentioned previously. Equation (A.5) represents a set of three coupled, nonlinear, simultanious equations which are, in general, quite difficult to solve. They have a rich family of solutions, however, including Bloch walls and bubble domains.

At present we are primarily interested in single domain materials in which case $\bar{H}_{oex}$ vanishes by (A.2b). If in addition, $|\bar{H}_0| \gg |\bar{H}_a|$, we can assume $\bar{M}_0 \parallel \bar{H}_0$. This approximation is valid for many cases of interest, but should be examined closely for lower microwave frequencies and strong anisotropies.

Making the strong field approximation and neglecting terms second order in small quantities enables us to write (A.4) in the form

$$i\bar{\Omega}\bar{m} = \hat{z} \times [\lambda_{ex} \nabla^2 \bar{m} + \vec{N}^a \cdot \bar{m} + \bar{h} - (Z_0 + Z_a)\bar{m}] \qquad (A.6)$$

where we have introduced several new quantities:

$$\Omega = - \frac{\omega}{\gamma \mu_o M_o} \tag{A.7a}$$

$$\overline{h}_a = \overline{\overline{N}}^a \cdot \overline{m} \tag{A.7b}$$

$$Z_o = H_o / M_o \tag{A.7c}$$

$$Z_a = \overline{H}_{oa} \cdot \hat{z} / M_o \tag{A.7d}$$

$$\nabla_t^2 = \frac{\partial^2}{\partial x^2} + \frac{\partial^2}{\partial y^2} \tag{A.7e}$$

and we have chosen the coordinate system so that the equilibrium magnetization points along the $\hat{z}$ direction. The form of the small signal anisotropy field is justified by noting that this field will only be present if there is some deviation from the equilibrium direction of $\overline{M}$. Keeping only the $\hat{z}$ component of $\overline{H}_{oa}$ is justified since the other components give rise to an m_z which we neglect as a second order quantity.

Solving for $\overline{h}$ in (A.6) gives

$$\overline{h} = \overline{\overline{A}}_{op} \cdot \overline{m} \tag{A.8a}$$

where

$$\overline{\overline{A}}_{op} = \begin{bmatrix} Z_o + Z_a - N_{xx}^a - \lambda_{ex} \nabla_t^2 & i\Omega - N_{xy}^a \\ -i\Omega - N_{yx}^a & Z_o + Z_a - N_{yy}^a - \lambda_{ex} \nabla_t^2 \end{bmatrix} \tag{A.8b}$$

This operator (with anisotropy set to zero) is the starting point for the exchange calculations of Chapter Two.

If exchange is neglected, equation (A.8) can be easily inverted to obtain the Polder susceptibility tensor

$$\overline{m} = \overset{=}{\chi} \cdot \overline{h} \tag{A.9a}$$

where

$$\chi_{xx} = (Z_o + Z_a - N_{yy}^a)/D \tag{A.9b}$$

$$\chi_{xy} = (-i\Omega + N_{xy}^a)/D \tag{A.9c}$$

$$\chi_{yx} = (i\Omega + N_{yx}^a)/D \tag{A.9d}$$

$$\chi_{yy} = (Z_o + Z_a - N_{xx}^a)/D \tag{A.9e}$$

$$D = (Z_o + Z_a - N_{yy}^a)(Z_o + Z_a - N_{xx}^a)$$

$$- (i\Omega + N_{yx}^a)(-i\Omega + N_{xy}^a) \tag{A.9f}$$

Bajpai, et al. (63) have derived an expression analogous to (A.9) for the permeability tensor $(\overset{=}{I} + \overset{=}{\chi})$ for an arbitrary orientation of the dc bias field. Their result is incorrect, however, since their tensor is not Hermitian (this is a requirement since their calculation does not include loss).

If anisotropy is neglected, the susceptibily reduces to the familiar form

$$\overset{=}{\chi} = \begin{bmatrix} \chi & -i\kappa \\ i\kappa & \chi \end{bmatrix} \tag{A.9g}$$

where

$$\chi = \frac{Z}{Z^2 - \Omega^2}, \qquad \kappa = \frac{\Omega}{Z^2 - \Omega^2}.$$

III. The Effective Anisotropy Field (67)

We consider here the anisotropy in a cubic ferromagnet. Such a model
is appropriate for single crystal bulk YIG, but inevitably YIG thin films
also exhibit a stress-induced uniaxial anisotropy due to the slight lattice
mismatch between the YIG and GGG substrate. This mismatch can be
minimized, however, by doping with suitable nonmagnetic impurities (68).

For a cubic ferromagnet, the anisotropy energy density to lowest order
is given by

$$W^a = \frac{K}{M_o^4} \left[M_1^2 M_2^2 + M_1^2 M_3^2 + M_2^2 M_3^2 \right] \tag{A.10}$$

where the subscripts $(1,2,3)$ refer to the principle crystal axes. The
effective anisotropy field is defined by

$$\overline{H}_a = - \frac{1}{\mu_o} \frac{\partial W^a}{\partial \overline{M}}$$

$$= - \frac{2K}{\mu_o M_o^4} \begin{vmatrix} M_1(M_2^2 + M_3^2) \\ M_2(M_1^2 + M_3^2) \\ M_3(M_1^2 + M_2^2) \end{vmatrix} \tag{A.11}$$

separating the static and time varying components and keeping terms to
first order in $\overline{m}$ gives

$$\overline{H}^a = - \frac{2K}{\mu_o M_o^4} \begin{vmatrix} M_{01}(M_{02}^2 + M_{03}^2) \\ M_{02}(M_{01}^2 + M_{03}^2) \\ M_{03}(M_{01}^2 + M_{02}^2) \end{vmatrix} + \overline{\overline{N}}^a \cdot \overline{m} \tag{A.12a}$$

where
$$N_{ii}^{a} = -\frac{2K}{\mu_0 M_0^4}(M_0^2 - M_{oi}^2) \tag{A.12b}$$

$$N_{ij}^{a} = -\frac{4K}{\mu_0 M_0^4} M_{oi} M_{oj}; \quad i \neq j \tag{A.12c}$$

Again, these quantities are expressed in terms of the major cubic axes of the crystal. In order to obtain the corresponding quantities in the xyz system defined in terms of the direction of the applied magnetic field, we use the transformation matrix $\overline{\overline{T}}$:

$$\overline{H}_a{}' = \overline{\overline{T}} \cdot \overline{H}_a \tag{A.13a}$$

$$\overline{\overline{N}}^{a}{}' = \overline{\overline{T}} \cdot \overline{\overline{N}}^{a} \cdot \overline{\overline{T}}^{-1} \tag{A.13b}$$

where

$$T_{11} = \cos\theta \cos\phi \cos\xi - \sin\phi \sin\xi$$

$$T_{21} = -\sin\phi \cos\xi - \cos\theta \cos\phi \sin\xi$$

$$T_{31} = \sin\theta \cos\phi$$

$$T_{12} = \cos\theta \sin\phi \cos\xi + \cos\phi \sin\xi$$

$$T_{22} = \cos\phi \cos\xi - \cos\theta \sin\phi \sin\xi \tag{A.13c}$$

$$T_{32} = \sin\theta \sin\phi$$

$$T_{13} = -\sin\theta \cos\xi$$

$$T_{23} = \sin\theta \sin\xi$$

$$T_{33} = \cos\theta$$

and θ, ϕ, ξ are the Euler angles relating the two coordinate systems.

IV. Walker's Equation and Magnetostatics

Maxwell's equations in the magnetostatic limit are

$$\nabla \times \overline{h} = 0 \qquad\qquad\qquad\text{(A.14a)}$$

$$\nabla \cdot (\overline{m} + \overline{h}) = 0 \qquad\qquad\qquad\text{(A.14b)}$$

Using (A.9) and introducing a magnetostatic scalar potential allows us to combine (A.14) into a single equation:

$$\partial_i [\delta_{ij} + \chi_{ij}]\partial_j \psi = 0 \qquad\qquad\qquad\text{(A.15)}$$

where $\overline{h} = - \nabla\psi$, $\partial_i \equiv \partial/\partial x_i$, and sums over repeated indices are implied. Expanding this equation gives

$$\left\{\partial_x\left[(1+\chi_{xx})\partial_x + \chi_{xy}\partial_y\right] + \partial_y\left[(1+\chi_{yy})\partial_y + \chi_{yx}\partial_x\right] + \partial_z^2\right\}\psi = 0 \qquad\text{(A.16)}$$

If $\overset{=}{\chi}$ is not a function of position this can be written

$$\left[(1+\chi_{xx})\partial_x^2 + (1+\chi_{yy})\partial_y^2 + \partial_z^2 + \frac{2N_{xy}^a}{D}\partial_x\partial_y\right]\psi = 0 \qquad\text{(A.17)}$$

where we have used the fact that $N_{xy}^a = N_{yx}^a$. Note that the presence of the cross term in (A.17) significantly complicates the solution of this equation. All of the correct existing calculations involving anisotropy of which the author is aware have been done in selected coordinate systems in which N_{xy}^a vanished. Unfortunately, there are many coordinate systems of practical interest in which this is not the case.

Because of the computational difficulties involved with anisotropy we

will not consider it further. In the absence of anisotropy, (A.17) reduces to the Walker equation (69)

$$\left[(1+\chi)(\partial_x^2 + \partial_y^2) + \partial_z^2\right]\psi = 0 \tag{A.18}$$

This result, combined with the requirement that tangential $\bar{h}$ and normal $\bar{b}$ be continuous across all boundaries, completes the formulation of the magnetostatic boundary value problem.

V. Dispersion Relations for Magnetostatic Waves in Ferrite Slabs

The following calculations neglect both exchange and anisotropy.

A. Surface Waves

Consider the geometry of Figure A.1. In air, Walker's equation reduces to Laplace's equation so the potential in the three regions can be expressed

$$\psi^I = A\, e^{-kx + i\nu ky} \tag{A.19a}$$

$$\psi^{II} = \left[B\, e^{-kx} + C\, e^{kx}\right] e^{i\nu ky} \tag{A.19b}$$

$$\psi^{III} = D\, e^{kx + i\nu ky} \tag{A.19c}$$

where $\nu = \pm 1$, and k is taken to be positive definite.

Continuity of tangential h requires the potential to be continuous across the surfaces of the ferrite giving rise to the equations

$$A\, e^{-kd/2} = B\, e^{-kd/2} + C\, e^{kd/2} \tag{A.20}$$
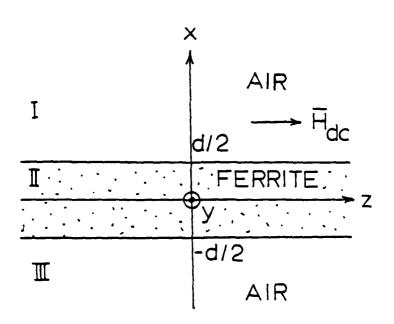
$$D\, e^{-kd/2} = B\, e^{kd/2} + C\, e^{-kd/2} \tag{A.21}$$

Figure A.1.   Surface and backward volume wave geometry.

Similarly, continuity of normal $\bar{b}$ gives

$$- Ae^{-kd/2} = (1+\chi)(Ce^{kd/2} - Be^{-kd/2}) + \nu\kappa(Be^{-kd/2} + Ce^{kd/2}) \qquad (A.22)$$

$$De^{-kd/2} = (1+\chi)(Ce^{-kd/2} - Be^{kd/2}) + \nu\kappa(Be^{kd/2} + Ce^{-kd/2}) \qquad (A.23)$$

The dispersion relation is obtained by setting the determinant of the coefficient matrix of the simultaneous homogeneous equations (A.20)-(A.23) equal to zero. The result is

$$\Omega^2 = Z(Z+1) + (1-e^{-2|k|d})/4 \qquad (A.24a)$$

$$\text{or} \qquad |k| = -\frac{1}{2d} \ln\left[4Z(Z+1) - 4\Omega^2 + 1\right] \qquad (A.24b)$$

The absolute values emphasize the fact that although surface waves exhibit field displacement nonreciprocity, the dispersion relation is reciprocal for propagation in the $\pm$ y directions. Equation (A.24) is plotted qualitatively in Figure A.2.

B. Backward Volume Waves

The geometry for backward volume waves is also given by Figure A.1, except that propagation is assumed along the $\pm$ z directions rather than along $\pm$ y. Let us first consider even modes (ie., modes in which $\psi(x)$ is even). The potential in the three regions can be written

$$\psi^I = A e^{-kx + i\nu kz} \qquad (A.25a)$$

$$\psi^{II} = B \cos k_x x \, e^{i \nu k z} \tag{A.25b}$$

$$\psi^{III} = C \, e^{kx + i \nu k z} \tag{A.25c}$$

Substituting (A.25b) into Walker's equation (A.18) gives the following relationship between k_x and k:

$$k_x = \frac{k}{\sqrt{-(1+\chi)}} \tag{A.26}$$

The radical is real since $1+\chi < 0$ in the volume wave manifold.

Requiring ψ to be continuous at $x = \pm d/2$ gives

$$A \, e^{-kd/2} = B \cos(k_x d/2) \tag{A.27}$$

$$C \, e^{-kd/2} = B \cos(k_x d/2) \tag{A.28}$$

while the boundary condition on normal $\bar{b}$ gives

$$-k \, A \, e^{-kd/2} = -B \, k_x \, (1+\chi) \, \sin(k_x d/2) \tag{A.29}$$

$$k \, C \, e^{-kd/2} = B \, k_x \, (1+\chi) \, \sin(k_x d/2) \tag{A.30}$$

The dispersion relation can be obtained by combining either (A.27) and (A.29) or (A.28) and (A.30). The result for even modes

$$\cot(k_x d/2) = - \sqrt{-(1+\chi)} \tag{A.31}$$

Note that although there is only one surface wave mode, there are a multiplicity of backward volume wave modes given by the roots of (A.31).

The odd modes can be obtained by assuming a new form for ψ^{II}:

$$\psi^{II} = B \sin(k_x x)\, e^{i \nu k z} \tag{A.32}$$

Repeating the above application of the boundary conditions gives

$$\cot(k_x d/2) = \frac{1}{\sqrt{-(1+\chi)}} \tag{A.33}$$

A single compact equation containing both the even and odd modes can be obtained by multiplying (A.31) and (A.33) and applying the identities

$$\cot^2 \theta/2 = \frac{1 + \cos\theta}{1 - \cos\theta} \tag{A.34a}$$

$$\cot\theta/2 = \frac{1 + \cos\theta}{\sin\theta} \tag{A.34b}$$

The result is

$$2\cot(k_x d) = \frac{1}{\sqrt{-(1+\chi)}} - \sqrt{-(1+\chi)} \tag{A.35a}$$

This is the form first given by Damon and Eshbach. Equations (A.31) and (A.33) can be combined in an even simpler way, however, by using the identity $\tan(\theta + \pi/2) = -\cot\theta$. The result is

$$\tan\left[(k_x d + n\pi)/2\right] = -\frac{1}{\sqrt{-(1+\chi)}} \quad ; \quad n = 0,1,2,\ldots \tag{A.35b}$$

Clearly for all even integers this is equivalent to (A.31) while for odd integers it gives (A.33). The backward volume wave spectrum as given by (A.35) is illustrated qualitatively in Figure A.3.
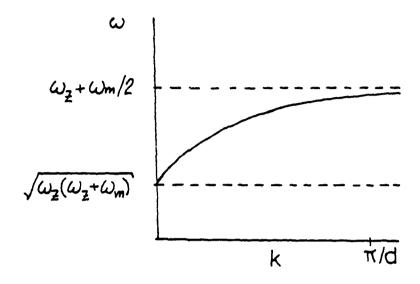
ω

$\omega_{\underline{z}} + \omega m/2$

$\sqrt{\omega_{\underline{z}}(\omega_{\underline{z}} + \omega_m)}$

k π/d

Figure A.2.   Surface wave dispersion diagram

ω

$\sqrt{\omega_{\underline{z}}(\omega_{\underline{z}} + \omega_m)}$

3

2

1

$n = 0$

$\omega_{\underline{z}}$
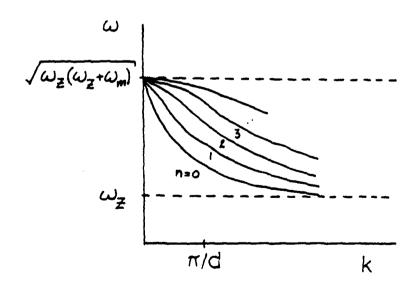
π/d k

Figure A.3.   Backward volume wave mode dispersion diagram

C. Forward Volume Waves

Forward volume waves propagate in a normally magnetized slab as illustrated in Figure A.4. In the absence of anisotropy, the propagation of forward volume waves is isotropic in the plane of the slab. We therefore arbitrarily choose propagation in the $\pm$ y directions.

For even modes, the potential in the three regions is of the form

$$\psi^I = A\, e^{-kz + i\nu ky} \tag{A.36a}$$

$$\psi^{II} = B\, \cos(k_z z)\, e^{i\nu ky} \tag{A.36b}$$

$$\psi^{III} = C\, e^{kz + i\nu ky} \tag{A.36c}$$

Requiring ψ to be continuous at $z = \pm\, d/2$ gives

$$A\, e^{-kd/2} = B\, \cos(k_z d/2) \tag{A.37}$$

$$C\, e^{-kd/2} = B\, \cos(k_z d/2) \tag{A.38}$$

and matching normal $\overline{b}$ at these boundaries gives

$$-kA e^{-kd/2} = -B\, k_z\, \sin(k_z d/2) \tag{A.39}$$

$$kC e^{-kd/2} = B\, k_z\, \sin(k_z d/2) \tag{A.40}$$

Combining either (A.37) and (A.39) or (A.38) and (A.40) gives the dispersion relation for even modes

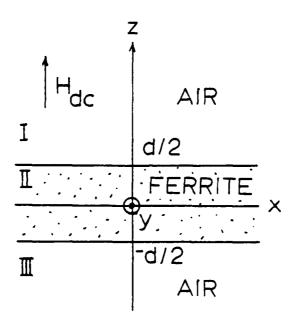$$\tan(k_z d/2) = \frac{1}{\sqrt{-(1+\chi)}} \tag{A.41}$$

Figure A.4.   Forward volume wave geometry.

where from Walker's equation

$$k_z = k \sqrt{-(1+\chi)} \ . \tag{A.42}$$

As before, the odd modes can be obtained by redefining ψ^{II}:

$$\psi^{II} = B \sin(k_z z) \, e^{i\nu k y} \tag{A.43}$$

The result is

$$-\cot(k_z d/2) = \frac{1}{\sqrt{-(1+\chi)}} \tag{A.44}$$

As in the backward volume wave case, the even and odd modes can be combined in a single equation using $\tan(\theta+\pi/2) = -\cot\theta$ to obtain

$$\tan\left[k_z d/2 + n\pi/2\right] = \frac{1}{\sqrt{-(1+\chi)}} \tag{A.45}$$

The magnetostatic forward volume wave spectrum is illustrated in Figure A.5.

D. Effects of an Adjacent Parallel Ground Plane

Some physical insight into the effects of placing metal in contact with one face of a ferrite slab can be obtained through the use of the image theorem. As illustrated in Figure A.6, magnetic dipoles parallel to a perfect electric conductor are imaged without inversion, whereas the images of dipoles normal to the surface are inverted (70).

In the case of forward volume waves, the rf magnetic dipoles are always parallel to the ground plane and so they are imaged without inversion. Hence the modes are identical to the even modes of a slab twice as thick
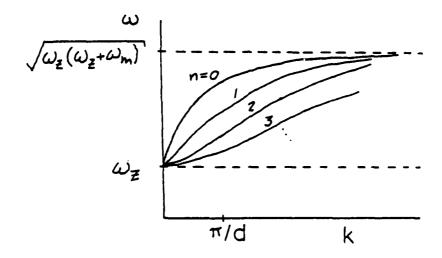
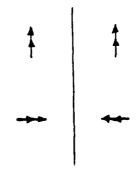Figure A.5. Forward volume wave dispersion diagram.

Figure A.⟨⟩ Magnetic dipoles imaged by a perfect electrical conductor.

without a ground plane.

Reference to (A.24), (A.35) and (A.45) reveals that for a fixed frequency, $k \propto 1/d$ for all three types of modes. Since the band edge at k=0 does not depend on d, this implies that thicker slabs sustain faster modes. Hence the presence of a conducting plate increases the velocities of forward volume waves.

In the case of surface waves and backward volume waves, the rf magnetic dipoles have components both perpendicular and parallel to the metal surface. As a result, the effect on the wave propagation is more complex than simply doubling the thickness. However, the qualitative result that the presence of the conducting plate increases mode velocities is still correct.

The case of a metal surface placed a finite distance away from the slab can be understood in terms of a transition between the limiting cases of a conducting surface in contact with the slab, and the conducting surface completely removed.

Due to the consequences of Laplace's equation, the magnitude of the potential outside of the slab always decays as exp(-kL), where k is the wavenumber and L is the distance along the slab normal[1]. As a consequence, for small k the metal will appear electrically as if it were in contact with the slab, while for large k the mode will not be affected by the metal. Intermediate values of k will be characterized by a smooth transition between these two limits.

---

[1] The form of the decay away from the surface becomes more complicated if the bias field is not uniform (see Chapter Three).

If $d/L \ll 1$ where L is the is the separation between the slab and the metal, only waves with small k will be affected. The results are illustrated qualitatively in Figure A.7. The actual dispersion relations for the three modes are given below, with the corresponding geometries illustrated in Figure A.8.

MSSW (57):

$$e^{2|k|d} = \frac{1}{2(\Omega v + Z) + 1} \left[\frac{1 + (\Omega v + Z)[1 + \tanh(-|k|L)]}{1 - (\Omega v - Z)[1 - \tanh(-|k|L)]} \right]$$ (A.46)

where $\psi \propto e^{iv|k|y}$; $v = \pm 1$.

MSBVW (59):

$$\cot\left[\frac{|k|d}{\sqrt{-(1+\chi)}}\right] = \frac{2 + \chi(1 + e^{-2|k|L})}{2\sqrt{-(1+\chi)}}$$ (A.47)

where $\psi \propto e^{iv|k|z}$; $v = \pm 1$.

MSFVW (58):

$$-\cot\left[-\sqrt{-(1+\chi)}|k|d\right] = \frac{1 + \chi + \tanh(|k|L)}{\sqrt{-(1+\chi)}[\tanh(|k|L) + 1]}$$ (A.48)

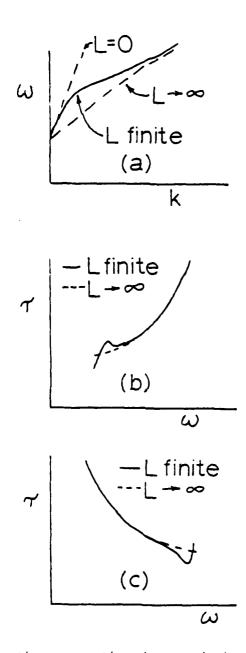where $\psi \propto e^{iv|k|x_i}$; $v = \pm 1$, $x_i = (x, y)$.

Figure A.7. Qualitative propagation characteristics for ferrite-dielectric-metal layered structure. (a) Dispersion relation for forward waves. (b) Delay characteristic for forward waves. (c) Delay characteristics for backward waves.
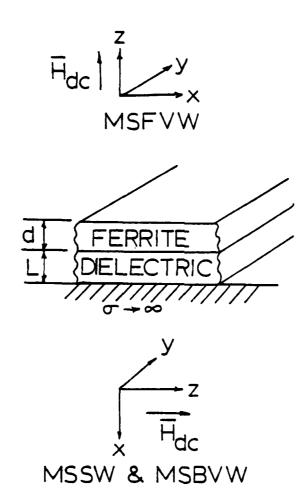
Figure A.8. Geometry and coordinate systems for ferrite-dielectric-metal layered structure.

E. Effects of Finite Slab Width

Generally speaking, introducing a finite width to the ferrite slab has the effect of adding a transverse component to the total k vector. In other words, we view the mode as consisting of a plane wave propagating at an oblique angle and bouncing back and forth down the slab.

As in Section V.D, the forward volume waves are again easier to understand. In the present case this is because the propagation is isotropic in the plane of the slab. Hence the frequency depends on the transverse component of k (k_t) in exactly the same way as the longitudinal component (k_ℓ). The transverse component is quantized and held relatively constant by the boundary conditions while the longitudinal component depends strongly on frequency. Hence k_t is negligible when k_ℓ is large, but k_t dominates for $k_\ell \to 0$.

The various quantized values of k_t give rise to an infinite number of modes which, when combined with the various modes corresponding to thickness variations, comprise a mode family entirely analogous to the modes of a rectangular metallic electromagnetic waveguide.

The effect on surface waves is more complicated, however, since propagation in the plane is not isotropic. As a result, when k_ℓ is small and k_t dominates, the wave has a volume wave character, whereas when k_ℓ dominates the surface wave character is restored. Hence the finite width induces a volume wave band near the band edge where $k_\ell \to 0$.

To the author's knowledge, no calculation of the width effects on backward volume waves has been done to date. However, it seems very likely

that a similar argument to the above could be made in favor of the existence of width-induced surface waves near the low-k band edge. It would be expected that these surface waves should show backward wave character.

For $d/w \ll 1$, where w is the slab width, only the spectrum near $k_\ell \rightarrow 0$ will be affected. The qualitative propagation behavior for surface and forward volume waves for this case is illustrated in Figure A.9. The presence of a ground plane such that $d/L \ll 1$ is also assumed. The dispersion relations for these cases are given below. It should be noted that both of these results are based on the somewhat artificial assumption of spin-pinning at the edges of the sample (44,65); the electromagnetic boundary conditions at the edges have not been rigorously satisfied. An integral equation formulation which rigorously satisfies these edge boundary conditions has been described by Morgenthaler (38,66). Unfortunately, the solution to the integral equation is not available in closed form.

MSSW (44) (width-induced volume waves excluded):

$$e^{2Md} = \frac{ZM+\Omega v|k|+(Z^2-\Omega^2)(M-N)}{ZM-\Omega v|k|+(Z^2-\Omega^2)(M+N)}$$

$$\times \frac{ZM-\Omega v|k|+(Z^2-\Omega^2)[M-N\tanh(NL)]}{ZM+\Omega v|k|+(Z^2-\Omega^2)[M+N\tanh(NL)]} \qquad (A.49)$$

where $M^2 = [n\pi/w]^2/(1+\chi) + k^2$, $N^2 = [n\pi/w]^2 + k^2$

(a) MSFVW dispersion

(b) MSFVW delay

(c) MSSW dispersion

(d) MSSW delay
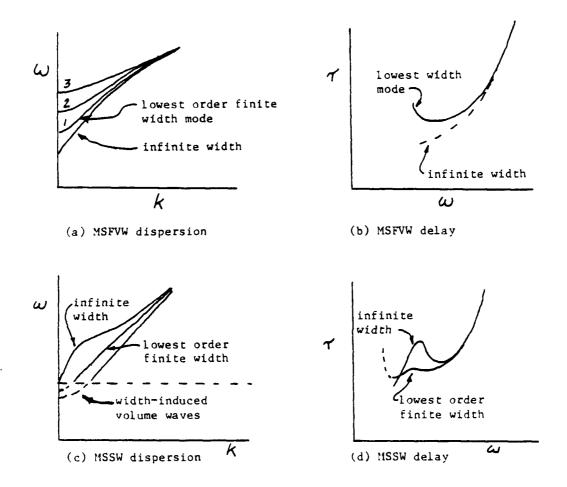
Figure A.9. Finite width effects on surface and forward volume wave propagation. A ground plane such that d/L <<1 is also included.

and $\psi \propto e^{i\nu|k|y}$; $\nu = \pm 1$.

MSFVW (65):

$$\cot(\alpha_f d) = \frac{\alpha_f^2 - \alpha_l^2 \tanh(\alpha_l L)}{\alpha_f \alpha_l [\tanh(\alpha_l L)+1]} \tag{A.50}$$

where $\alpha_f^2 = -(1+\chi)[k^2+(n\pi/w)^2]$, $\alpha_l^2 = k^2 + (n\pi/w)^2$,

and $\psi \propto e^{i\nu|k|y}$; $\nu = \pm 1$.

APPENDIX B

Harmonic Oscillator Mathematics

A. One-dimensional Harmonic Oscillator

1. The equation for a one-dimensional quantum mechanical harmonic oscillator can be written

$$\frac{\partial^2 \phi(x)}{\partial x^2} + \left[\frac{2\varepsilon}{\alpha^2} - \frac{x^2}{\alpha^4}\right]\phi(x) = 0 \tag{B.1}$$

where α is a characteristic length defined in the context of a particular problem. In natural or normalized units the equation assumes the form

$$\frac{\partial^2 \bar{\phi}(\xi)}{\partial \xi^2} + (2\varepsilon - \xi^2)\bar{\phi}(\xi) = 0 \tag{B.2}$$

where $\xi = x/\alpha$.

2. The eigenfunctions of (B.1) which vanish at infinity are given by the Hermite-Gaussian functions

$$\phi_n(x) = \frac{H_n(x/\alpha)\, e^{-x^2/2\alpha^2}}{(\alpha\, 2^n\, n!\, \sqrt{\pi})^{1/2}} \tag{B.3}$$

where $H_n(\xi)$ is the nth order Hermite polynomial (see (B.9)). The corresponding solutions to (B.2) are given by

$$\bar{\phi}_n(\xi) = \frac{H_n(\xi)\, e^{-\xi^2/2}}{(2^n\, n!\, \sqrt{\pi})^{1/2}} \tag{B.4}$$

The eigenvalues belonging to either eigenfunction are

$$\varepsilon = n + 1/2 \quad , \quad n = 0,1,2, \ldots \tag{B.5}$$

3. Hermite polynomials are solutions to the equation

$$\frac{d^2 H_n}{d\xi^2} - 2\xi\frac{dH_n}{d\xi} + 2nH_n = 0 \tag{B.6}$$

4. The Hermite polynomials can be expressed

$$H_n(\xi) = \left[\frac{d^n}{ds^n} e^{-s^2+2s\xi}\right]_{s=0} \tag{B.7}$$

where

$$F(s,\xi) = e^{-s^2+2s\xi} \tag{B.8}$$

is the <u>generating function</u> for Hermite polynomials. The first few Hermite
polynomials are

$$
\begin{aligned}
H_0(\xi) &= 1 & H_3(\xi) &= -12\xi+8\xi^3 \\
H_1(\xi) &= 2\xi & H_4(\xi) &= 12-48\xi^2+16\xi^4 \\
H_2(\xi) &= -2+4\xi^2 & H_5(\xi) &= 120\xi-160\xi^3+32\xi^5
\end{aligned} \tag{B.9}
$$

5. Useful recurrence relations for Hermite polynomials are

$$\frac{dH_n}{d\xi} = 2nH_{n-1} \tag{B.10a}$$

$$H_{n+1} = 2\xi H_n - 2nH_{n-1} \tag{B.10b}$$

6. The orthogonality integral for Hermite polynomials is

$$\int_{-\infty}^{\infty} H_m(\xi)H_n(\xi)e^{-\xi^2}d\xi = \delta_{mn} \, 2^n \, n! \sqrt{\pi} \qquad (B.11)$$

7. The orthonormality of the Hermite-Gaussian functions (B.3) and (B.4) can be easily demonstrated using (B.11):

$$\int_{-\infty}^{\infty} d\xi \; \tilde{\phi}_n(\xi)\tilde{\phi}_m(\xi) = \int_{-\infty}^{\infty} dx \; \phi_n(x)\phi_m(x) = \delta_{mn} \qquad (B.12)$$

8. The derivative of the Hermite-Gaussian $\phi(x)$ can be obtained using (B.3) and (B.10):

$$\frac{d\phi_n(x)}{dx} = \frac{1}{\alpha}\left[\phi_{n-1}\sqrt{\frac{n}{2}} - \phi_{n+1}\sqrt{\frac{n+1}{2}}\right] \qquad (B.13)$$

9. A measure of the spatial extent of the functions $\phi_n(x)$ is given by the location of the turning point of equation (B.1) defined as

$$2\varepsilon - x_{tp}^2/\alpha^2 = 0 \qquad (B.14a)$$

Combining this with (B.5) gives

$$x_{tp} = \alpha\sqrt{2n+1} \qquad (B.14b)$$

B. Two-dimension Harmonic Oscillator

1. The equation of a two-dimensional quantum mechanical harmonic oscillator is

$$\alpha_x^2\frac{\partial^2\psi}{\partial x^2} + \alpha_y^2\frac{\partial^2\psi}{\partial y^2} + \left(2\varepsilon - \frac{x^2}{\alpha_x^2} - \frac{y^2}{\alpha_y^2}\right)\psi = 0 \qquad (B.15)$$

Assuming a product function for ψ, this separates into two one-dimensional harmonic oscillator equations

$$\frac{\partial^2 \phi_x}{\partial x^2} + \left[\frac{2\epsilon_x}{\alpha_x^2} - \frac{x^2}{\alpha_x^4}\right]\phi_x = 0 \qquad (B.16a)$$

$$\frac{\partial^2 \phi_y}{\partial y^2} + \left[\frac{2\epsilon_y}{\alpha_y^2} - \frac{y^2}{\alpha_y^4}\right]\phi_y = 0 \qquad (B.16b)$$

where $\epsilon = \epsilon_x + \epsilon_y$.

In the case of equation (2.80)(Chapter Two), we have

$$\frac{2\epsilon_x}{\alpha_x^2} + \frac{2\epsilon_y}{\alpha_y^2} = (a + \Omega\sigma - Z_0)/\lambda_{ex} \qquad (B.16c)$$

where $\alpha_x = (\lambda_{ex}/B_x)^{1/4}$ and $\alpha_y = (\lambda_{ex}/B_y)^{1/4}$.

2. The eigenfunctions of (B.15) which vanish at infinity are simply products of one-dimensional Hermite-Gaussians as indicated by (B.16). We have

$$\psi_{n_x n_y}(x,y) = \phi_{n_x}(x)\phi_{n_y}(y) \qquad (B.17)$$

where $\phi_{n_i}(x_i)$ is given by (B.3).

3. The orthonormality of the functions $\psi_{n_x n_y}$ is easily demonstrated using (B.17) and (B.11). The result is

$$\int_{-\infty}^{\infty} dx \int_{-\infty}^{\infty} dy\ \psi_{n_x n_y}\psi_{m_x m_y} = \delta_{n_x, m_y}\ \delta_{n_x, m_y} \qquad (B.18)$$

C. <u>Properties</u> <u>of</u> <u>the</u> <u>Generalized</u> <u>Functions</u> $\phi_m^n(z)$

1. For the analysis of Chapter Three, it is convenient to introduce

the generalized one-dimensional Hermite-Gaussian function:

$$\phi_m^n(z) = \frac{H_m(z/\alpha_n) \, e^{-z^2/2\alpha_n^2}}{(\alpha_n \, 2^m \, m! \, \sqrt{\pi})^{1/2}} \tag{B.19}$$

These functions represent the set of m solutions to n different harmonic

oscillator problems.

The functions $\phi_n^n(z)$ are shown in Chapter Three to be solutions of the

equation

$$\frac{\partial^2}{\partial z^2}\phi_n^n(z) + (A-Bz^2)\Lambda^2\phi_n^n(z) = 0 \tag{B.20}$$

where $\Lambda^2 = B(2n+1)^2/A^2$, and $\alpha_n = \sqrt{\dfrac{A}{B(2n+1)}}$.

2. The functions $\phi_m^n(z)$ are not, in general, orthogonal:

$$\int_{-\infty}^{\infty} dz \, \phi_m^n(z)\phi_q^r(z) \neq 0 \tag{B.21}$$

This is simply because for $n \neq r$ the functions are solutions to different

harmonic oscillator problems. It follows that functions having the same

characteristic lengths (ie., $n=r$) are orthonormal:

$$\int_{-\infty}^{\infty} dz \, \phi_m^n(z)\phi_q^n(z) = \delta_{mq} \tag{B.22}$$

3. The derivative of $\phi_m^n(z)$ is given by

$$\frac{\partial \phi_m^n}{\partial z}(z) = \frac{1}{\alpha_n}\left[\phi_{m-1}^n \sqrt{\frac{m}{2}} - \phi_{m+1}^n \sqrt{\frac{m+1}{2}}\right] \tag{B.23}$$

4. The quantity $z^2\phi_n^n(z)$ is needed for the integral equation theory of Chapter Three. This quantity can be expressed in terms of the second derivative of ϕ_n^n by use of the differential equation (B.20a). The result is

$$z^2\phi_n^n = \alpha_n^4 \frac{\partial^2 \phi_n^n}{\partial z^2} + \frac{A}{B}\phi_n^n \tag{B.24}$$

The second derivative can be obtained by differentiating (B.23). This gives

$$\frac{\partial^2 \phi_n^n}{\partial z^2} = \frac{\sqrt{n(n-1)}}{2\alpha_n^2}\phi_{n-2}^n - \frac{(2n+1)}{2\alpha_n^2}\phi_n^n + \frac{\sqrt{(n+1)(n+2)}}{2\alpha_n^2}\phi_{n+2}^n \tag{B.25}$$

Substituting (B.25) and (B.20c) into (B.24) gives the final result

$$z^2\phi_n^n = \frac{A\sqrt{n(n-1)}}{2B(2n+1)}\phi_{n-2}^n + \frac{A}{2B}\phi_n^n + \frac{A\sqrt{(n+1)(n+2)}}{2B(2n+1)}\phi_{n+2}^n \tag{B.26}$$

5. The Fourier Transform of $\phi_m^n(z)$ is defined as

$$\phi_m^n(\zeta) = \int_{-\infty}^{\infty} dz\ e^{-i\zeta z}\phi_m^n(z) \tag{B.27}$$

It is computationally convenient to define the normalized variables $u=\zeta\alpha_n$ and $\xi=z/\alpha_n$. Making these substitutions and using (B.19) gives

REFERENCES

1. J. D. Adam, J. H. Collins, and J. M. Owens, "Microwave Device Applications of Epitaxial Magnetic Garnets," Radio and Electronics Engineer, 45 738 (1975).

2. J. D. Adam and J. H. Collins, "Microwave Magnetostatic Delay Devices Based on Epitaxial Yttrium Iron Garnet," Proc. of IEEE, 64 794 (1976).

3. J. H. Collins and F. A. Pizzarello, "Propagating Magnetic Waves in Thick Films: A Complementary Technology to Surface Wave Acoustics," Int. J. Elect., 34 319 (1973).

4. J. H. Collins and J. M. Owens, "Magnetostatic Wave and SAW Devices--Similarities, Differences and Trade-offs," 1978 IEEE International Symposium on Circuits and Systems Proc. (IEEE, New York, 1978) p. 536.

5. K. Reed, "Microwave Pulse Compression Loops with MSW Delay Lines," RADC/EEA Microwave Magnetics Technology Workshop Proc., June 10-11, 1981 (to be published).

6. D. A. Zeskind and F. R. Morgenthaler, "Localized High-Q Ferromagnetic Resonance in Nonuniform Magnetic Fields," IEEE Trans. on Mag., MAG-13 1249 (1977).

7. J. D. Adam, "A Temperature Stabilized Magnetostatic Wave Device," 1970 IEEE MTT-S International Microwave Symp. Digest, p. 160 (1979).

8. J. Castera, "MSW Temperature Coefficients," RADC/EEA Microwave Magnetics Technology Workshop Proc., June 10-11, 1981 (to be published).

9. D. D. Stancil, "A Microwave Diplexer Using Magnetostatic Surface and Backward Volume Waves," Memorandum to MIT Microwave and Quantum Magnetics Group, August, 1981 (unpublished).

10. M. Tsutsumi, Y. Masaoka, T. Ohira and N. Kumagai, "The Effect of an Inhomogeneous Bias Field on the Delay Characteristics of Magnetostatic Forward Volume Waves," Appl. Phys. Let., 35 204 (1979).

11. F. R. Morgenthaler, "Magnetostatic Waves Bound to a DC Field Gradient," IEEE Trans. on Mag., MAG-13 1252 (1977).

12. F. R. Morgenthaler, "Bound Magnetostatic Waves Controlled by Field Gradients in YIG Single Crystal and Epitaxial Films," IEEE Trans. on Mag., MAG-14 806 (1978).

13. F. R. Morgenthaler, "Novel Devices Based upon Field Gradient Control of Magnetostatic Modes and Waves," The Third International Conference on Ferrites, Proc., Sept. 29—Oct. 2, 1980, Kyoto (to be published).

14. F. R. Morgenthaler, private communication, Nov., 1978.

15. F. R. Morgenthaler, "Two-dimensional Magnetostatic Resonances in a Thin Film Disk Containing a Magnetic Bubble," J. Appl. Phys., 50 2209 (1979).

16. F. R. Morgenthaler, private communication, Oct., 1980.

17. O. G. Vendik and D. N. Chartorizhskii, "Spin-wave Spectrum in a Thin Ferromagnetic Film in a Rectangular Waveguide," Soviet Physics-Solid State, 11 1957 (1970).

18. O. G. Vendik, B. A. Kalinikos and D. N. Chartorizhskii, "Instability of Spin Waves in Tangentially Magnetized Ferromagnetic Films," Soviet Physics-Solid State, 19 222 (1977).

19. D. D. Stancil, "Magnetostatic Waves in Nonuniform Bias Fields Including Exchange Effects," IEEE Trans. on Mag., MAG-16 1153 (1980).

20. D. D. Stancil, "Localized Magnetostatic Resonances in Inhomogeneous Fields Including Exchange Effects," Memorandum to Microwave and Quantum Magnetics Group, April, 1979 (unpublished).

21. D. D. Stancil, "Virtual Surfaces, Harmonic Oscillator Wavefunctions, and the Spin Wave Continuum," Memorandum to Microwave and Quantum Magnetics Group, June, 1979 (unpublished).

22. F. R. Morgenthaler, private communication, Nov., 1978.

23. D. D. Stancil and F. R. Morgenthaler, "Magnetostatic Surface Modes in a Thin Film with Nonuniform In-plane Fields," IEEE Trans. on Mag., MAG-16 1156 (1980).

24. D. D. Stancil and F. R. Morgenthaler, "The Effects of Nonuniform In-plane Fields on the Propagation Characteristics of Magnetostatic Surface Waves," 1980 Ultrasonics Symposium Proc. (IEEE, New York, 1980) p. 547.

25. D. D. Stancil and F. R. Morgenthaler, "Guiding Magnetostatic Surface Waves with Nonuniform In-plane Fields," RADC/EEA Microwave Magnetics Technology Workshop Proc., June 10-11, 1981 (to be published).

26. L. Brillouin, Wave Propagation and Group Velocity, Academic Press, Inc., New York, 1960.

27. Pleshko and I. Palocz, "Experimental Observation of Sommerfeld and Brillouin Precursors in the Microwave Domain," Phys. Rev. Let., 22 1201 (1969).

28. D. D. Stancil, "Magnetostatic Wave Precursors in Ferrite Thin Films Part I: Theory," Memorandum to Microwave and Quantum Magnetics Group, November, 1980 (unpublished).

29. A. Platzker and F. R. Morgenthaler, "Synthesized Linearly Dispersive Microwave YIG Delay Line with Wide Instantaneous Bandwidth," AIP Conference Proc No. 29, p. 645 (1975).

30. J. R. Eshbach, "Spin-Wave Propagation and the Magnetoelastic Interaction in YIG," J. Appl. Phys., 34 1298 (1963).

31. E. Schlomann, "Spin-Wave Spectroscopy Advances in Quantum Physics," Columbia Univ. Press, (New York, 1961) p. 437.

32. W. Strauss, "Magnetoelastic Waves in Yttrium Iron Garnet," J. Appl. Phys., 36 118 (1965).

33. B. A. Auld and D. A. Wilson, "Bragg Scattering of Infrared Radiation from Coherent Spin Waves," J. Appl. Phys., 38 3331 (1967).

34. H. L. Hu, "Studies of Magnetostatic Waves and Magnetoelastic Waves in YIG Using Optical Probing and Microwave Techniques," MIT Microwave and Quantum Magnetics Group Technical Report No. 25 (1971).

35. J. T. Yu, R. A. Turk, and P. E. Wigen, "Exchange-Dominated Surface Spin Waves in Thin Yttrium-Iron-Garnet Films," Phys. Rev. B, 11 420 (1975).

36. C. Vittoria and J. H. Schelleng, "Effects of Diffusion on Magnetic Excitations in Films of Yttrium Iron Garnet," Phys. Rev. B, 16 4020 (1977).

37. J. J. Cooley, "Magnetostatic Modes Bound by DC H field Gradients," MIT Microwave and Quantum Magnetics Group Technical Report 40 (1977).

38. F. R. Morgenthaler, "Magnetostatic Surface Modes in Nonuniofrm Thin Films with In-plane Bias Fields," J. Appl. Phys., 52 2267 (1981).

39. M. Bini, L. Millanta, and N. Rubino, "Gaussian-beam Distribution of Magnetostatic Surface Waves in Inhomogeneous DC Field," J. Appl. Phys. 46 3175 (1975).

40. W. Faber, "Terminations for Magnetostatic Waves," Elect. Let. 16 452 (1980).

41. L. Taylor, "MSW Terminations," RADC/EEA Microwave Magnetics Technology Workshop Proc., June 10-11, 1981 (to be published).

42. J. H. Collins, D. M. Hastie, J. M. Owens and C. V. Smith, "Matched Loads for Magnetostatic Wave Delay Lines," Wave Elect., 3 201 (1978).

43. W. L. Bongianni, "Magnetostatic Propagation in a Dielectric Layered Structure," J. Appl. Phys. 43 2541 (1972).

44. T. W. O'Keefe and R. W. Patterson, "Magnetostatic Surface-Wave Propagation in Finite Samples," J. Appl. Phys., 49 4886 (1978).

45. J. M. Owens, J. H. Collins, and J. D. Adam, "Planar Microwave Multipole Filters using LPE-YIG," AIP Conf. Proc. No. 24, p. 497 (1975).

46. J. D. Adam, J. H. Collins, and J. M. Owens, "Microwave Device Applications of Epitaxial Magnetic Garnets," Radio and Elect. Engineer, 45 738 (1975).

47. This acid mixture was recommended by Dr. Howard Glass of Rockwell International in a private communication, December, 1980.

48. A. Bers, "Linear Waves and Instabilities," Plasma Physics-Les Houches (1972).

49. Z. M. Bardai, J. D. Adam, J. H. Collins and J. P. Parekh, "Delay Lines Based on Magnetostatic Volume Waves in Epitaxial YIG," AIP Conf. Proc. No. 34, p. 268 (1976).

50. J. D. Jackson, Classical Electrodynamics, 2nd Edition, John Wiley and Sons (1975).

51. B. Schneider, "Effect of Crystalline Anisotropy on the Magnetostatic Spin Wave Modes in Ferromagnetic Plates I. Theoretical Discussion for Infinite Plates," Phys. Stat. Sol. (b), 51 325 (1972).

52. C. V. Smith, Jr., J. M. Owens, T. J. Mears II and N. D. Parikh, "Induction Probing of Magnetostatic Delay Line Fields," IEEE Trans. on Mag., MAG-15 1738 (1979).

53. P. N. Horowitz, "Variable Speed Magnetostic Modes in Uniform or Nonuniform DC H Fields," MIT Microwave and Quantum Magnetics Group Technical Report No. 41 (1978).

54. R. W. Damon and J. R. Eshbach, "Magnetostatic Modes of a Ferromagnet Slab," J. Phys. Chem. Solids, 19 308 (1961).

55. R. W. Damon and H. Van De Vaart, "Propagation of Magnetostatic Spin Waves at Microwave Frequencies in a Normally-Magnetized Disk," J. Appl. Phys., 36 3453 (1965).

56. S. R. Seshadri, "Surface Magnetostatic Modes of a Ferrite Slab," Proc. IEEE, 58 506 (1970).

57. W. L. Bongianni, "Magnetostatic Propagation in a Dielectric Layered Structure," J. Appl. Phys., 43 2541 (1972).

58. T. Yukawa, J. Ikenoue, J. Yamada and K. Abe, "Effects of Metal on Dispersion Relations of Magnetostatic Volume Waves," J. Appl. Phys., 49 376 (1978).

59. N. D. J. Miller, "Non-Reciprocal Propagation of Magnetostatic Volume Waves," Phys. Stat. Sol. (a), 43 593 (1977).

60. B. Schneider, "Effect of Crystalline Anisotropy on the Magnetostatic Spin Wave Modes in Ferromagnetic Plates II. Results for finite Plates," Phys. Stat. Sol. (b), 66 99 (1974).

61. C. Vittoria and N. D. Wilsey, "Magnetostatic Wave Propagation Losses in an Anisotropic Insulator," J. Appl. Phys. 45 414 (1974).

62. N. C. Srivastava, "Magnetostatic Modes of a Slab of Hexagonal Planar Ferrite," J. Appl. Phys., 47 5447 (1976).

63. S. N. Bajpai, I. Rattan, N. C. Srivastava, "Magnetostatic Volume Waves in Dielectric Layered Structure: Effect of Magnetocrystalline Anisotropy," J. Appl. Phys., 50 2887 (1979).

64. C. V. Smith, Jr., J. M. Owens, N. D. Parikh, and R. L. Carter, "Anisotropic Propagation of Magnetostatic Waves in Epitaxial YIG Films," (to be published).

65. S. N. Bajpai, N. C. Srivastava, "Magnetostatic Bulk Wave Propagation in a Multilayered Structure," Elect. Let., 16 269 (1980).

66. F. R. Morgenthaler, "Field Gradient Control of Magnetostatic Waves for Microwave Signal Processing Applications," RADC/EEA Microwave Magnetics Technology Workshop Proc., June 10-11, 1981 (to be published).

67. See, for example, F. R. Morgenthaler, "Dynamic Magnetoelastic Coupling in Ferromagnets and Antiferromagnets," IEEE Trans. on Mag., MAG-8, 130 (1972).

68. H. Glass, "Epitaxial Ferrites for MSW Devices," RADC/EEA Microwave Magnetics Technology Workshop Proc., June 10-11, 1981 (to be published).

69. L. R. Walker, "Resonant Modes of Ferromagnetic Spheroids," J. Appl. Phys., 29 318 (1958).

70. J. A. Kong, Theory of Electromagnetic Waves, John Wiley and Sons (1975).

Control of the Frequency of Energy Circulation of Magnetostatic Modes in a Sphere

The SM thesis of Mr. Daniel A. Fishman, now nearing completion, is concerned with the control of frequency at which magnetostatic mode energy circulates in a YIG sphere; the uniform precession is of particular interest.

A portion of the thesis proposal is given below:

The use of ferrimagnetic materials, particularly YIG spheres, in microwave magnetically tunable filters is widespread. In general these devices have good power handling characteristics. It is proposed that this is due, in part, to the fast velocity of energy circulation of the modes, (analogous to the group velocity for planes waves), and that this works to prevent low power limiting. However, it has been shown by Morgenthaler that this velocity can be altered by changing the specific electromagnetic boundary conditions. The situation where this boundary condition is of the form of a concentric conducting spherical shell, is studied theoretically and approximated experimentally. The theoretical analysis indicates that there is a critical ratio, between the radius of the YIG sample and that of the conducting spherical cavity, where the velocity will become zero. These calculations did not include the electromagnetic losses that arise in the experimental situation, thus the velocity approaches zero at this ratio. In addition to the effect of the energy velocity upon signal delay times, there is the effect of decreasing the critical power threshold for nonlinear effects. The onset of instabilities in the uniform precession of the magnetization is due to a level of rf energy density inside the sample which exceeds a certain critical value. A decrease in energy velocity could be expected to decrease the amount of incident power required to obtain this critical energy density.

The object of this work is to observe the predicted effects the velocity of energy circulation may have on the onset of spin wave instabilities and other nonlinear effects.

MISSION
of
Rome Air Development Center

RADC plans and executes research, development, test and selected acquisition programs in support of Command, Control Communications and Intelligence (C^3I) activities. Technical and engineering support within areas of technical competence is provided to ESD Program Offices (POs) and other ESD elements. The principal technical mission areas are communications, electromagnetic guidance and control, surveillance of ground and aerospace objects, intelligence data collection and handling, information system technology, ionospheric propagation, solid state sciences, microwave physics and electronic reliability, maintainability and compatibility.

DAT
FILM